

# **Quantum networking with single ions and single photons interfaced in free space**

**Dissertation**

zur Erlangung des Grades  
des Doktors der Naturwissenschaften  
der Naturwissenschaftlich-Technischen Fakultät II  
– Physik und Mechatronik –  
der Universität des Saarlandes

von

**Christoph Kurz**



Saarbrücken 2015

Tag des Kolloquiums: 16.09.2015

Dekan: Univ.-Prof. Dr. Georg Frey

Mitglieder des Prüfungsausschusses: Univ.-Prof. Dr. Jürgen Eschner  
Univ.-Prof. Dr. Ferdinand Schmidt-Kaler  
Univ.-Prof. Dr. Philipp Treutlein  
Univ.-Prof. Dr. Rolf Pelster  
PD Dr. Michael Koblichka

## Abstract

Atom-based quantum memories and processors, interconnected through photonic quantum channels, are a promising platform for quantum networks with the goal of secure information transmission and calculational speed-up.

In my dissertation, I first cover the experimental methods and tools for the manipulation of single  $^{40}\text{Ca}^+$  ions. This includes a narrow-band laser for addressing an optical quantum bit (qubit) as well as a magnetic field for the manipulation of a radio-frequency qubit.

Furthermore, I describe experiments toward the implementation of basic quantum networks; by means of suitable laser excitation, we generate single photons, tailored both temporally and spectrally, onto which we transfer the ion's coherence properties.

Finally, I present a protocol in which the polarization state of a single photon is transferred onto the spin state of a single ion through an absorption process. Successful state transfer is heralded by the detection of a Raman-scattered photon. This property of the protocol (*heralded* quantum-state transfer) allows for mapping the photonic onto the atomic quantum state with high fidelity, even in the case of low absorption probabilities. In addition, a slight modification of the experimental scheme allows for the generation of an entangled atom-photon state.

## Zusammenfassung

Eine vielversprechende Plattform für Quantennetzwerke zum Zwecke sicherer Informationsübertragung und erhöhter Rechengeschwindigkeit sind auf einzelnen Atomen basierende Quantenspeicher und -prozessoren, die untereinander Information durch Lichtquanten (Photonen) austauschen.

In meiner Dissertation behandle ich zunächst die experimentellen Methoden und Werkzeuge zur Manipulation einzelner  $^{40}\text{Ca}^+$ -Ionen. Dazu zählen ein schmalbandiger Laser zur Adressierung eines optischen Quantenbits (Qubit) sowie ein Magnetfeld zur Manipulation eines Radiofrequenzqubits.

Im Weiteren beschreibe ich vorbereitende Experimente zur Implementierung einfacher Quantennetzwerke; durch geeignete Laseranregung lassen sich zeitlich und spektral maßgeschneiderte Einzelphotonen erzeugen, auf die sich die Kohärenzeigenschaften des Ions übertragen lassen.

Schließlich stelle ich ein Protokoll vor, mit dem der Polarisationszustand eines einzelnen Photons durch Absorption auf den Spinzustand eines einzelnen Ions übertragen wird. Erfolgreiche Zustandsübertragungen werden durch die Detektion eines Raman-gestreuten Photons angekündigt. Diese Eigenschaft des Protokolls (*heralded* quantum-state transfer) erlaubt das Übertragen des photonischen auf den atomaren Quantenzustand mit hoher Güte (Fidelity), selbst im Fall geringer Absorptionswahrscheinlichkeiten. Eine leichte Modifikation des experimentellen Schemas erlaubt zudem die Erzeugung eines verschränkten Atom-Photon-Zustands.

# Contents

<b>Introduction</b>	<b>9</b>
<b>1 Trapping ions</b>	<b>15</b>
1.1 Trapping theory . . . . .	15
1.1.1 The Paul trap . . . . .	15
1.1.2 Basics of light-matter interaction . . . . .	19
1.1.3 Laser cooling trapped ions . . . . .	22
1.1.4 Atomic level scheme . . . . .	26
1.2 Experimental setup . . . . .	27
1.2.1 Trap apparatus . . . . .	28
1.2.2 Optical access . . . . .	29
1.2.3 Laser system . . . . .	30
1.2.4 Experimental control unit . . . . .	32
<b>2 Experimental tools for quantum-state manipulation</b>	<b>35</b>
2.1 Coherent manipulations – optical qubit . . . . .	35
2.1.1 Qubit laser at 729 nm . . . . .	36
2.1.2 Experimental sequence . . . . .	38
2.1.3 Internal-state discrimination . . . . .	39
2.1.4 Spectroscopy . . . . .	42
2.1.5 Rabi oscillations . . . . .	43
2.1.6 Characterization of magnetic-field noise . . . . .	44
2.2 Coherent manipulations – radio-frequency qubit . . . . .	48
2.2.1 Magnetic-dipole transitions . . . . .	49
2.2.2 Experimental implementation . . . . .	50
2.2.3 Spectroscopy . . . . .	51
2.2.4 Rabi oscillations . . . . .	52
2.2.5 Ramsey experiment . . . . .	53
2.3 Optical ground-state pumping . . . . .	54
2.3.1 Pumping at 397 nm . . . . .	55
2.3.2 Pumping at 729 nm . . . . .	56
2.4 Auxiliary spectroscopy . . . . .	57
2.4.1 866 nm spectroscopy . . . . .	57

2.4.2	854 nm spectroscopy . . . . .	58
2.5	Ion-temperature measurement . . . . .	58
<b>3</b>	<b>Toward quantum networking</b>	<b>63</b>
3.1	Generation of single photons . . . . .	63
3.1.1	Spontaneous Raman scattering . . . . .	64
3.1.2	Experimental realization . . . . .	70
3.2	Atom-to-photon phase mapping . . . . .	77
3.2.1	Quantum beats . . . . .	77
3.2.2	Experimental realization . . . . .	78
3.2.3	Results . . . . .	79
<b>4</b>	<b>Quantum-networking experiments</b>	<b>81</b>
4.1	Protocol for photon-to-atom quantum-state transfer . . . . .	81
4.1.1	Quantum-state transfer scheme . . . . .	82
4.1.2	Experimental realization . . . . .	84
4.1.3	State transfer in circular polarization basis . . . . .	86
4.1.4	State transfer of linear polarization . . . . .	87
4.1.5	Quantum-process tomography . . . . .	90
4.1.6	State-transfer fidelity vs. heralding probability . . . . .	90
4.1.7	Error sources . . . . .	91
4.1.8	Alternative schemes . . . . .	91
4.1.9	Coherence-time considerations for single-photon realizations . . . . .	93
4.2	Atom-photon entanglement . . . . .	94
4.2.1	Scheme for atom-photon entanglement . . . . .	95
4.2.2	Experimental realization . . . . .	96
4.2.3	Interlude: Quantum-state tomography . . . . .	98
4.2.4	Experimental results . . . . .	100
4.2.5	Error sources . . . . .	103
<b>5</b>	<b>Conclusion</b>	<b>105</b>
5.1	Related work: Photonic interaction between distant ions . . . . .	105
5.2	Summary . . . . .	108
5.3	Outlook . . . . .	109
<b>Appendix</b>		<b>111</b>
A.1	Properties of atomic states and transitions . . . . .	111
A.2	Adiabatic passage . . . . .	111
A.3	Probability distribution of an oscillating magnetic field . . . . .	116
A.4	Ramsey-fringe visibility . . . . .	117
A.5	Spectrum of a single-photon wave packet . . . . .	119
A.6	Probability distribution of parasitic photons . . . . .	120
A.7	Estimating the multi-photon probability . . . . .	121
A.8	Maximum-likelihood estimation for a two-qubit system . . . . .	122

Contents

---

<b>Journal publications</b>	<b>125</b>
<b>Bibliography</b>	<b>127</b>
<b>Acknowledgments</b>	<b>141</b>



# Introduction

In the course of the past decades, computer science has brought vast socio-economic and ecological changes to society. The ability to process information in a rapid and automatized way, accompanied by the advent of the internet, enabled the development of technical applications that have revolutionized our everyday life. However, despite today's enormous computing capacities, certain types of mathematical problems have so far eluded efficient<sup>1</sup> computation by current technology. While no efficient algorithms for these intractable problems seem to exist on classical computers, quantum physics offers concepts that allow one to tackle these issues through a qualitative computational speed-up [1].

## Quantum computing

Classical computers operate on registers of binary digits (bits) [2] that can be in the logical states 0 and 1. Following the input–process–output dogma [3], information is written onto the register, processed through logic gates, and read out. Since a classical bit can be in only one state at a time, only one input state can be processed at a time. Quantum physics, however, provides us with quantum bits (qubits) [1], which can be in both logical states simultaneously (quantum superposition). Furthermore, qubits can exhibit non-classical correlations (quantum entanglement). These characteristics allow processing many different input states by a single computational step, a feature sometimes referred to as *quantum parallelism* [4]. However, it is not trivial to extract the desired information from the quantum register after performing a quantum computation. This has led to the conclusion that a quantum processor excels only at certain mathematical problems for which suitable quantum algorithms exist. The probably best-known example is Shor's algorithm [5] which efficiently factorizes composite numbers into their primes and computes discrete logarithms. It is based on the quantum Fourier transform [1], which is also the groundwork for the Deutsch-Jozsa algorithm [6] which efficiently determines if a given function is balanced or constant. Another class of quantum algorithms are those based on amplitude amplification [7], the most prominent being Grover's algorithm [8] for the efficient search of unstructured databases. A third class of algorithms is based on quantum walks [9] which enable exponential speed-ups for certain black-box (oracle) problems.

In addition to the ambition of quantum computing, a more specialized approach is

---

<sup>1</sup>In this context, “efficient” means that the computing time scales only polynomially with the input length, in contrast to e.g. exponential scaling.

found in the branch of *quantum simulation* [10]; many physical phenomena, in particular quantum many-body systems [11] such as magnetism and superconductivity, cannot be simulated efficiently on a classical computer. In 1982, Richard Feynman proposed using a well-controlled quantum system that is engineered in order to behave like the physical system under study [12]. While the latter might be hard to control experimentally, it might be simulated efficiently on another, more easily controllable system.

However, beyond the special-purpose quantum simulator, great interest was raised by the idea of a universal quantum computer, also referred to as quantum Turing machine. This concept, first proposed by David Deutsch in 1985 [4] and inspired by Richard Feynman's idea of a quantum simulator, allows one to harness all power of quantum computation in that any quantum algorithm can be implemented through quantum logic gates [1]. Similar to classical computation, a quantum gate performs quantum operations on one or several qubits. A universal set of quantum gates is any finite set of gates that allows one to approximate any conceivable quantum operation through a finite sequence of gates. An example for such a set are the Hadamard gate, a phase rotation and a controlled-NOT gate. Another universal set is that containing only the three-qubit Deutsch gate [13]. It should be mentioned at this point that important alternative approaches, such as measurement-based models [14, 15] or adiabatic quantum computation [16, 17], exist, but the general trend in quantum computing seems to tend toward the gate-based concept.

On the experimental side, many physical systems have proven worth investigating for the implementation of a quantum-information processor. They can be grouped in three categories, of which the most representative systems shall be named:

- Quantum-optical systems: photons [14, 18], electrons [19], trapped atoms [20, 21] and ions [22, 23]
- Solid-state systems: superconducting circuits [24, 25], quantum dots [26], color centers in diamond [27]
- Nuclear magnetic resonance (NMR) systems [28, 29]

As technology evolved and all these systems became more and more developed, it became necessary to define precise requirements on a physical system. In 2000, David DiVincenzo formulated the well-known criteria named after him that any physical system aspiring to constitute a universal quantum-information processor ought to fulfill [30]:

1. The qubits are well-defined and well-characterized, and the system is scalable.
2. All qubits can be initialized to a well-defined state.
3. The qubit coherence time significantly exceeds the typical gate-operation time.
4. A universal set of quantum gates exists.
5. All qubits can be read out individually.

**The quantum system of choice: single trapped ions**

Of all the physical systems listed above, single trapped atomic ions have come closest to complying with the DiVincenzo criteria, proving to be among the most promising candidates for future large-scale quantum-information processors [31, 32]. Atomic ions can be confined by oscillating electric fields and well isolated from the laboratory environment [33]. Hence they can easily be cooled to very low temperatures [34] and exhibit very long coherence times [35]. Typically, the electronic (internal) state of a single ion is used to encode a qubit, while the collective motion (external state) of a string of single ions acts as a quantum bus between the qubits. Laser, radio-frequency and microwave sources that are nowadays close to technical perfection are used to manipulate both the electronic and motional state of an ion string at a very high degree of control. This facilitates the quantum operations required to implement universal sets of quantum gates; the ions can be addressed individually by laser beams [36], but also by microwave fields [37], to perform single-qubit gates, while addressing the collective motion allows for executing multi-qubit gates [38, 39]. That way, a number of quantum-gate operations have been demonstrated experimentally, such as single-qubit rotations and phase shifts [40], the geometric phase gate [38], the controlled-NOT gate [41, 42], the Toffoli gate [43], and the highly versatile Mølmer-Sørensen gate [44, 45, 39]. Nowadays, many of these gates are carried out with very high fidelity [46]. Prior to any gate operations, however, all qubits must be initialized in a pure electronic state, which is usually achieved through optical-pumping techniques [47]. Following a sequence of gates, the qubits can be individually read out through state-dependent fluorescence measurements [48]. Furthermore, quantum error-correction protocols, which will allow for fault-tolerant quantum computing, have been devised [49, 50] and implemented [51, 52]. With these tools at hand, a number of quantum algorithms have been realized in proof-of-principle experiments, e.g. the Deutsch-Jozsa algorithm [53] and the quantum Fourier transform [54].

Also, the great advances of quantum simulations implemented in systems of single trapped ions should be mentioned. To name only a few, models of interacting spins, such as the Ising model [55], have been simulated, but also relativistic phenomena like Klein tunneling [56] and the zitterbewegung [56] have been studied.

**Quantum networks**

The approach toward a quantum-information processor based on strings of single trapped ions reaches its limit in the first DiVincenzo criterion, i.e. scalability; as the number of ions increases, so does the number of motional modes, increasing the spectral mode density (“mode crowding”). The smaller the mode spacing, the lower the speed at which many types of quantum gates that make use of the ions’ collective motion can be executed. At some point, quantum algorithms will become too slow to be carried out in a sensible amount of time. In addition, it becomes increasingly hard to maintain qubit coherence over the duration of a computational cycle.

Two widely recognized approaches have been proposed that might be able to overcome the scalability issue. One is based on arrays of microtraps within the same quantum-

information processor, where each microtrap holds only a manageable number of ions [22, 57, 58, 59]. Exchanging quantum information between the traps by shuttling single ions creates a quantum-information processor which is much more powerful than the entity of independently working microtraps. However, this approach is technically very challenging, in particular due to anomalous heating [60]. This effect is very prominent in microtraps; ions trapped in close proximity (typically 20 – 50  $\mu\text{m}$ ) to the trap surface experience much higher heating rates when compared with ions held in traditional, macroscopic traps. This effect is not yet fully understood and currently constitutes a major obstacle to the microtrap approach.

Our group, however, pursues the approach of quantum networking [21, 61]. The fundamental idea is similar to that of the microtrap array; the quantum-information processor is broken up into small processing units (network nodes, containing the “stationary qubits”) that are connected through optical channels. Instead of shuttling the ions themselves, quantum information is exchanged through photons (“flying qubits”) via the optical channels. In order to formulate requirements on any practical implementation of a quantum network, the DiVincenzo criteria have been extended [30]:

6. Stationary and flying qubits can be interconverted.
7. Flying qubits can be transmitted faithfully between network nodes.

We focus on these two criteria in particular, as their implementation represents the backbone of quantum networking.

The essential resource in a quantum-network scenario is *distant entanglement*: in order to have several network nodes form a larger-scale quantum-information processor, individual stationary qubits from different nodes need to be entangled. Three experimental schemes for establishing distant entanglement have emerged so far, one of which is based on the projective measurement of photonic quantum states: in either a single-photon [62, 63] or two-photon [64, 65, 66] configuration, photons emitted from two stationary qubits are brought to interference on a beam splitter, and their subsequent detection projects the two stationary qubits onto an entangled state. In another scheme, a stationary qubit from one node is entangled with a photon, and the latter is sent to another network node where its state is mapped onto another stationary qubit, thereby attaining entanglement between the two qubits [67, 68]. Our group, however, also pursues a third approach: a photon source, in our case a spontaneous parametric down-conversion (SPDC) source [69, 70], emits pairs of entangled photons. The two photons of a pair are split up and sent to two different network nodes. Mapping the quantum state of each photon onto a stationary qubit at the respective node transfers the entanglement from the photon pair onto the two nodes (hence the term *entanglement transfer*) [71, 72, 73].

Distant entanglement has brought forward many interesting applications in addition to quantum computation. For example, the concept of *quantum repeaters* [74] plays an essential role in transmitting quantum information over large distances. Despite the availability of low-cost optical fibers with very low absorption losses in the near-infrared region (telecom C and O band), photonic quantum states cannot be transmitted faithfully beyond a typical distance of  $\sim 10$  km [75, 76]. Very much in analogy to classical repeaters, breaking a

long quantum channel into smaller ones, connected through quantum repeaters, will allow one to overcome the current limitation imposed by fiber attenuation. Another application for distant entanglement has been found in *quantum teleportation* [77, 78, 79, 80]. Once entanglement has been established between the qubits of two network nodes, a special kind of projective measurement (coupled with the transmission of classical information) allows for transferring the state of a qubit from one node to the other.

### Quantum-network interfaces

At the heart of a quantum network lies the interface that facilitates the exchange of quantum information between flying and stationary qubits. Such an interface must provide efficient as well as faithful conversion of quantum states between the two kinds of qubits. In the context of quantum networks based on single atoms or ions, a variety of technical approaches has been undertaken so far, a very popular one being optical resonators (cavities) [81, 82]. Atoms trapped inside a cavity are strongly coupled to the cavity light modes, enabling efficient quantum-state conversion between atoms and photons. Integrating such a cavity with ion traps for quantum-information processing has, however, proven to be technically very challenging since efficient atom-light coupling requires small cavity volumes and thus very small ion traps.

A very different approach is found in objectives and lenses of high numerical aperture (NA) [83, 84, 85]. They impose less restrictive demands on the size of ion traps and are significantly easier to handle than optical cavities, albeit they are not yet a match for cavities in terms of coupling efficiency. We have chosen to employ high-NA objectives which allow for large experimental flexibility and easily accommodate most types of ion traps.

Also, the novel approach of mirrors for atom-photon interfaces should be mentioned. Strong atom-light coupling has been demonstrated by placing a single ion in the focal spot of a parabolic mirror [86, 87]. However, this method is once more experimentally challenging; positioning the ion at the focal spot is a delicate task, and handling the polarization pattern of light emitted by the ion is highly nontrivial.

### This work

We operate two independent, spatially separated Paul traps for confining, cooling and manipulating single  $^{40}\text{Ca}^+$  ions. Objectives of high numerical aperture ( $\text{NA} = 0.4$ ) allow for efficient coupling between the atomic state and the light field. The work presented in this thesis comprises the realization of basic quantum-networking operations. This includes both the experimental prerequisites and the demonstration of fundamental building blocks for quantum networks.

After introducing the theoretical and experimental principles, I cover the experimental methods and tools required for the control and manipulation of quantum-mechanical states. This includes a narrow-band laser resonant with an optical transition between two long-lived atomic states, the latter forming an optical qubit. Another type of qubit is represented by two Zeeman substates whose transition frequency lies in the radio-frequency

domain. This qubit is manipulated coherently and independently of the ion's thermal motion by means of a magnetic field. Further experimental methods for state manipulation include cooling of the thermal motion and optical pumping to specific Zeeman states.

Furthermore, I describe experiments toward the implementation of basic quantum networks. We demonstrate the efficient generation of single photons from a single ion, controlled through sequences of laser pulses [88]. The photons' temporal and spectral properties are governed by suitable choice of the laser parameters. In the following, we modify this scheme to map atomic phase information onto the photonic quantum state [89].

In the last chapter, I present the realization of two typical building blocks for quantum networks; for the first, we implement a protocol in which the polarization state of a single photon is mapped onto the quantum state of a single ion through an absorption process [90]. Successful state transfer is heralded by the detection of a Raman-scattered photon. This particular property of the protocol allows for a high state-transfer fidelity, even in the case of low absorption probabilities. The scheme constitutes the pinnacle of my thesis; it is currently the only one that enables high-fidelity heralded photon-to-atom quantum-state transfer and, at the same time, local quantum-information processing. We achieve transfer fidelities  $> 95\%$ , while work from competing groups [81, 91] has so far been limited to fidelities  $< 10\%$  due to the lack of a suitable heralding signal<sup>2</sup>. In contrast, quantum memories based on atomic ensembles [92] have been shown to be suitable for heralded photon-to-atom quantum-state transfer; ensembles, however, do not offer the prospect of local quantum-information processing.

Our second building block for quantum-networking is formed by an experiment entangling a single photon with the ion. A spontaneous Raman photon is emitted as the ion returns from an excited to the ground state via two atomic transitions that result in distinct final states of the ion's angular-momentum degree of freedom, hence the photonic polarization becomes entangled with the atomic spin.

I conducted most of the experiments presented in this thesis with my colleagues Michael Schug and Jan Huwer. Some of this work, such as setting up the narrow-band qubit laser and atom-to-photon phase mapping, is described in more detail in their Ph.D. theses [93, 94].

---

<sup>2</sup>Non-heralded schemes: even though the fidelity in the case of a *successful* state transfer may be very high, the fidelity in a single experimental shot is limited by the photon-absorption probability ( $< 10\%$ ).

# Chapter 1

## Trapping ions

Singly ionized atoms from the alkaline earth group provide textbook examples for a quantum mechanical system. With their single valence electron, they are well understood by theory and the first choice for studying single atomic quantum systems. With the advent of laser cooling [95, 96, 97], control over the quantum state of single ions in all degrees of freedom by quantum-optical means came within reach [98, 99]. After being an interesting subject of study of its own, improved experimental control led to first applications of trapped ions as in the fields of time and frequency measurements [100, 101] and quantum information processing [102, 103, 104, 32].

However, experiments with trapped ions require a large technical overhead. Apart from the ion trap itself with the need for ultra-high vacuum conditions, complex laser systems and experimental control units are required. This chapter will give an overview of the theoretical part, including trapping of ions and light-matter interaction, as well as the experimental section covering details of the actual setup in our laboratory.

### 1.1 Trapping theory

The following section is dedicated to giving a brief insight into the theory of trapping and manipulating single ions. After illustrating the principle of the radio-frequency ion trap, the basics of light-matter interaction for cooling and coherently controlling single trapped ions will be presented.

#### 1.1.1 The Paul trap

The centerpiece of quantum-optical experiments using single trapped ions is the radio-frequency trap invented by Wolfgang Paul [105]. It is based on oscillating and static electric fields (as opposed to the Penning trap, which employs static electric and magnetic fields) and allows for confining ions over time scales of hours to days [106].

As the Paul trap facilitates control over all atomic degrees of freedom (electronic and motional) [107], it has become of high importance in the field of high-precision measurements, including atomic-mass spectrometry [108] and frequency measurements [100, 101].

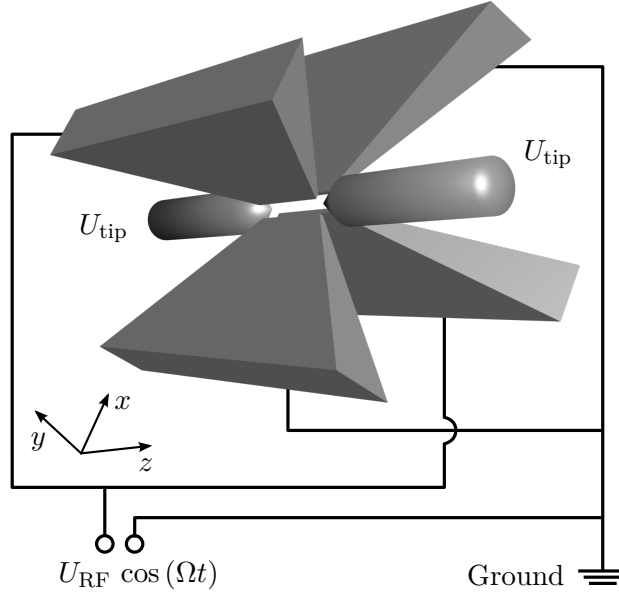


**Fig. 1.1:** Linear Paul trap for confining charged particles. Shown are the blade electrodes for radial and the end-tip electrodes for axial confinement.

Originally designed as an ion-mass filter [109], a linear version of the Paul trap became popular in the field of quantum information as it allows for performing quantum-logic operations in strings of trapped ions [41, 42].

In the following, I will illustrate the basic principle of the linear Paul trap, while more detailed descriptions are found in [110, 111, 112].

### Operating principle

As opposed to traps which make use of magnetic fields to confine charged particles, a Paul trap uses purely electric fields. A desirable trapping potential would be of harmonic shape,

$$\Phi(\vec{r}) = \Phi_0 (\alpha x^2 + \beta y^2 + \gamma z^2), \quad (1.1)$$

and attractive in all three dimensions, i.e.  $\alpha, \beta, \gamma > 0$  (for  $\Phi_0 > 0$ ). However, in order to satisfy Laplace's equation  $\Delta\Phi = 0$  (following from Maxwell's equations in free space), the condition

$$\alpha + \beta + \gamma = 0 \quad (1.2)$$

is derived, which means it is not possible to spatially confine charged particles in all three dimensions with purely static electric fields (Earnshaw's theorem [113]). This is resolved by using instead a temporally varying electric field in combination with a static field. A schematic of the type of linear Paul trap we use is shown in fig. 1.1. It comprises four diagonally arranged blade electrodes and two end-tip electrodes. Applying a radio-frequency voltage  $U(t) = U_{\text{RF}} \cos(\Omega t)$  to a pair of opposing trap blades while grounding

the others generates the electric quadrupole potential

$$\Phi_{\text{RF}}(\vec{r}) = \frac{U_{\text{RF}}}{2r_0^2} (r_0^2 + x^2 - y^2) \cos(\Omega t). \quad (1.3)$$

At the same time, a static potential

$$\Phi_{\text{tip}}(\vec{r}) = \frac{\alpha U_{\text{tip}}}{2l_0^2} (2z^2 - x^2 - y^2), \quad (1.4)$$

is superimposed by applying a static voltage  $U_{\text{tip}} > 0$  to the end-tip electrodes. Here  $r_0$  and  $l_0$  denote half the distance between opposing trap blades and the end tips, respectively. The geometry factor  $\alpha$  accounts for the deviation of the end-tip shape from an ideal hyperbolic surface. The net force from these potentials on an ion with a single positive charge is

$$\vec{F} = -e\vec{\nabla}(\Phi_{\text{RF}} + \Phi_{\text{tip}}). \quad (1.5)$$

From Newton's law  $\vec{F} = m\ddot{\vec{r}}$ , we derive the equations of motions for an ion of mass  $m$ :

$$\ddot{x} + \left( -\frac{\alpha U_{\text{tip}}}{l_0^2} + \frac{U_{\text{RF}}}{r_0^2} \cos(\Omega t) \right) \frac{e}{m} x = 0 \quad (1.6)$$

$$\ddot{y} + \left( -\frac{\alpha U_{\text{tip}}}{l_0^2} - \frac{U_{\text{RF}}}{r_0^2} \cos(\Omega t) \right) \frac{e}{m} y = 0 \quad (1.7)$$

$$\ddot{z} + 2 \frac{\alpha U_{\text{tip}}}{l_0^2} \frac{e}{m} z = 0 \quad (1.8)$$

Introducing the stability parameters

$$a_x = a_y = -\frac{a_z}{2} = -\frac{4\alpha e U_{\text{tip}}}{m l_0^2 \Omega^2} \quad (1.9)$$

and

$$q_x = -q_y = -\frac{2e U_{\text{RF}}}{m r_0^2 \Omega^2}, \quad q_z = 0 \quad (1.10)$$

yields the Mathieu equations of motion

$$\ddot{r}_i + (a_i - 2q_i \cos(\Omega t)) \frac{\Omega^2}{4} r_i = 0 \quad (1.11)$$

with  $i = x, y, z$ . As ansatz we choose a solution of the form

$$r_i(t) = r_{0,i} \cos(\omega_i t) \left( 1 - \frac{q_i}{2} \cos(\Omega t) \right), \quad (1.12)$$

representing a harmonic oscillation with frequency  $\omega_i$  (the secular motion), amplitude-modulated at the drive frequency  $\Omega$  (the micromotion<sup>1</sup>). This ansatz solves the Mathieu equation under the *pseudopotential* approximation [114]; we assume the secular motion to

---

<sup>1</sup>The term *micromotion* stems from its amplitude which is much smaller than that of the secular motion for typical values of  $q_i$ .

be at a much lower frequency than the micromotion ( $\omega_i \ll \Omega$ ). The ion's motion is thus governed by a quasi-static potential, the pseudopotential. After inserting the ansatz 1.12 into the differential equation 1.11, we take the time average of all fast-oscillating terms, i.e.  $\cos(\Omega t) \rightarrow 0$  and  $\cos^2(\Omega t) \rightarrow \frac{1}{2}$ , and obtain the condition

$$\omega_i = \frac{\Omega}{2} \sqrt{a_i + \frac{q_i^2}{2}} \quad (1.13)$$

for the secular frequency. Explicitly, the three frequencies are

$$\omega_z = \sqrt{\frac{2\alpha e U_{\text{tip}}}{m l_0^2}} \quad (1.14)$$

$$\omega_x = \sqrt{\omega_{x,0}^2 - \frac{1}{2}\omega_z^2} \quad (1.15)$$

$$\omega_y = \sqrt{\omega_{y,0}^2 - \frac{1}{2}\omega_z^2}, \quad (1.16)$$

with the bare radial frequencies ( $U_{\text{tip}} \rightarrow 0$ )

$$\omega_{x,0} = \omega_{y,0} = \frac{e U_{\text{RF}}}{\sqrt{2} m r_0^2 \Omega}. \quad (1.17)$$

Note the *defocusing effect* that reduces the secular frequency of the radial motion when the ion is more tightly confined along the axial direction.

We can now also more precisely quantify the validity of the pseudopotential approximation; the condition  $\omega_i \ll \Omega$  is fulfilled when the stability parameters satisfy the condition  $\sqrt{|a_i|}, |q_i| \ll 1$  for  $i = x, y, z$ .

### Excess micromotion

The above considerations are restricted to ideal trapping potentials generated purely by the trap electrodes. In a real experimental apparatus, however, we can expect external electric bias fields caused by electronic devices to couple to the ion's charge. Static fields are a major contribution and displace the ion from the trap center. For a field of magnitude  $E_i$  along direction  $i$ , we can easily modify the differential equation 1.11 and the ansatz 1.12 for the ion's motion to obtain the solution

$$r_i(t) = r_{0,i} \cos(\omega_i t) \left(1 - \frac{q_i}{2} \cos(\Omega t)\right) + r_{\text{dis},i} - \frac{q_i}{2} r_{\text{dis},i} \cos(\Omega t) \quad (1.18)$$

with the secular frequencies  $\omega_i$  defined as above and the ion displacement  $r_{\text{dis},i} = \frac{e E_i}{m \omega_i^2}$  from the trap center. Apart from this static displacement, an additional oscillating part, the excess micromotion, emerges. For sufficiently large bias fields it is no longer negligible compared with the secular motion. This has a number of adverse effects, e.g. sidebands at the micromotion frequency in absorption and emission spectra of the ion [115]. Besides, being a driven motion, the micromotion cannot be reduced using laser cooling techniques.

The standard way to overcome excess micromotion is the use of compensation electrodes placed between the trap blades [107, 112]. Carefully adjusting the static voltages on these electrodes allows one to shift the ion back to the trap center, eliminating any excess micromotion.

### 1.1.2 Basics of light-matter interaction

For most purposes of this work, it will be sufficient to treat all light fields interacting with the single trapped ion classically, since we use laser pulses of macroscopic optical power to manipulate the atomic state. On the other hand, we quantize the electronic and motional atomic degree of freedom, which leads us to the semiclassical approach [33]. Here, I restrict myself to the one-dimensional description.

The system Hamiltonian describing the atomic degrees of freedom is given by

$$H_{\text{sys}} = \frac{\hbar\omega_0}{2} (|e\rangle\langle e| - |g\rangle\langle g|) + \hbar\omega_{\text{T}} a^\dagger a. \quad (1.19)$$

The first part of  $H_{\text{sys}}$  describes the electronic degree of freedom as a two-level system of ground state  $|g\rangle$  and excited state  $|e\rangle$ , split by  $\hbar\omega_0$ , with the zero-point of energy centered between the two levels. The second part treats the ion as confined in a harmonic potential of trap frequency  $\omega_{\text{T}}$  (with the zero-point energy term omitted), making use of the ladder operators  $a$  and  $a^\dagger$  in the Fock basis  $\{|n\rangle\}$ .

For many purposes, it is sufficient to consider the interaction of a light field with an atomic electric-dipole transition. The light is described by a plane wave of the form  $E = E_0 \cos(kx - \omega_{\text{L}}t)$  with amplitude  $E_0$ , wave number  $k$  and frequency  $\omega_{\text{L}}$ , interacting with the atomic electric dipole  $\mu$ . The interaction Hamiltonian then reads

$$H_{\text{int}} = -\mu E_0 \cos(kx - \omega_{\text{L}}t) \quad (1.20)$$

$$= -\frac{1}{2} \mu E_0 \left( e^{i(kx - \omega_{\text{L}}t)} + \text{h.c.} \right) \quad (1.21)$$

$$= -\frac{E_0}{2} (|g\rangle\langle g| + |e\rangle\langle e|) \mu (|g\rangle\langle g| + |e\rangle\langle e|) \left( e^{i(kx - \omega_{\text{L}}t)} + \text{h.c.} \right). \quad (1.22)$$

Making use of the parity of atomic wave functions, i.e.  $\langle g|\mu|g\rangle = \langle e|\mu|e\rangle = 0$ , we find

$$H_{\text{int}} = -\frac{E_0}{2} (|e\rangle\langle e|\mu|g\rangle\langle g| + \text{h.c.}) \left( e^{i(kx - \omega_{\text{L}}t)} + \text{h.c.} \right). \quad (1.23)$$

Assuming the matrix element  $\langle e|\mu|g\rangle$  to be real, we define  $\Omega := -\frac{1}{\hbar} E_0 \langle e|\mu|g\rangle$  as the coupling strength<sup>2,3</sup>, more commonly termed Rabi frequency. Furthermore we express the position operator in terms of the ladder operators as  $x = \sqrt{\frac{\hbar}{2m\omega_{\text{T}}}} (a + a^\dagger)$  (with ion mass  $m$ ) and define the dimensionless Lamb-Dicke parameter

$$\eta = k \sqrt{\frac{\hbar}{2m\omega_{\text{T}}}}. \quad (1.24)$$

This quantity is proportional to the ratio of the spread of the motional ground-state wave function and the wavelength of the incident light. It thus describes how much the ion “perceives” of the spatial phase variation of the light wave.

---

<sup>2</sup>For electric-quadrupole transitions, which are equally important in our context, the coupling strength is found to be  $\Omega = \frac{1}{\hbar} \langle e|\frac{1}{6} \text{tr}[Q \cdot (\text{grad } E)]|g\rangle$  with the electric-quadrupole operator  $Q$ .

<sup>3</sup>Taking into account the micromotion of the ion in the radio-frequency trap, the coupling strength reduces to  $\frac{\Omega}{1+|q_x|/2}$  with the stability parameter  $q_x$  (see eqn. 1.10) [33].

With these definitions, the interaction Hamiltonian becomes

$$H_{\text{int}} = \frac{\hbar\Omega}{2} (|e\rangle\langle g| + |g\rangle\langle e|) \left( e^{i\eta(a+a^\dagger)} e^{-i\omega_L t} + e^{-i\eta(a+a^\dagger)} e^{i\omega_L t} \right). \quad (1.25)$$

As a next step, we transform the problem from the Schrödinger to the interaction picture through the unitary rotation  $U = e^{iH_{\text{sys}}t/\hbar}$ . Evaluating  $UH_{\text{int}}U^\dagger$  is rather tedious, and it is worth noting that this transformation is equivalent to moving to the Heisenberg picture instead when no interaction Hamiltonian is present. Thus the temporal evolution of the interaction Hamiltonian  $H_{\text{int}}^I$  in the interaction picture is governed by the Heisenberg equation:

$$\frac{d}{dt} H_{\text{int}}^I = \frac{i}{\hbar} [H_{\text{sys}}, H_{\text{int}}^I] + \frac{\partial H_{\text{int}}^I}{\partial t} \quad (1.26)$$

Using the relations

$$\frac{d}{dt} a = i\omega_T [a^\dagger a, a] \quad (1.27)$$

$$= -i\omega_T a \quad (1.28)$$

and

$$\frac{d}{dt} (|e\rangle\langle g|) = i\frac{\omega_0}{2} [|e\rangle\langle e| - |g\rangle\langle g|, |e\rangle\langle g|] \quad (1.29)$$

$$= i\omega_0 |e\rangle\langle g| \quad (1.30)$$

(and correspondingly for their hermitian conjugates), we find the transformed interaction Hamiltonian

$$H_{\text{int}}^I = \frac{\hbar\Omega}{2} \left( e^{i\omega_0 t} |e\rangle\langle g| + \text{h.c.} \right) \left( e^{-i\omega_L t} e^{i\eta(a(t)+a^\dagger(t))} + \text{h.c.} \right) \quad (1.31)$$

with  $a(t) = a e^{-i\omega_T t}$  and  $a^\dagger(t) = a^\dagger e^{i\omega_T t}$ . Upon expanding the parentheses in the equation above, we find terms oscillating at the sum and difference of the light frequency and the atomic resonance frequency, respectively. When the light field is tuned close to the atomic resonance, i.e.  $|\omega_L - \omega_0| \ll \omega_0$ , and assuming  $\Omega \ll \omega_0$ , the sum-frequency terms oscillate too fast to contribute significantly to the temporal evolution of the atomic state. The *rotating-wave approximation* [116] neglects these terms, and we find the simplification

$$H_{\text{int}}^I = \frac{\hbar\Omega}{2} \left( e^{-i\Delta t} e^{i\eta(a(t)+a^\dagger(t))} |e\rangle\langle g| + \text{h.c.} \right) \quad (1.32)$$

with the detuning parameter  $\Delta = \omega_L - \omega_0$ . When expanding the term  $e^{i\eta(a(t)+a^\dagger(t))}$  in a Taylor series, powers of the ladder operators emerge, rotating at integer multiples of the trap frequency. When excited resonantly, they couple the two electronic states and different motional states simultaneously. The effective Rabi frequency at which transitions of the form  $|g, n\rangle \leftrightarrow |e, n+m\rangle$  are driven amounts to [33]

$$\Omega_{n, n+m} = \Omega \left| \langle n+m | e^{i\eta(a+a^\dagger)} | n \rangle \right| \quad (1.33)$$

$$= \Omega e^{-\eta^2/2} \eta^{|m|} \sqrt{\frac{n_{<}!}{n_{>}!}} L_{n_{<}}^{|m|}(\eta^2) \quad (1.34)$$

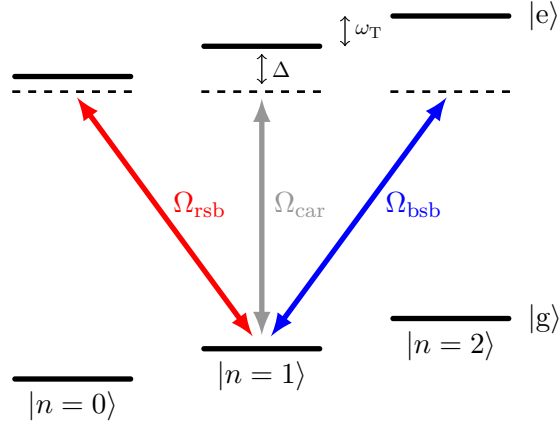


**Fig. 1.2:** The three lowest motional states of the ion for the two electronic states  $|g\rangle$  and  $|e\rangle$ . Motional side-band as well as carrier transitions are resonantly excited through proper choice of the light-field detuning.

with the associated Laguerre polynomials  $L$  and  $n_<$  ( $n_>$ ) as the lesser (greater) of  $n + m$  and  $n$ .

While the above expressions provide a very accurate treatment of the ion's dynamics, it is instructive to consider another simplification; if the spread of the ion's wave function is sufficiently small, i.e.  $\eta\sqrt{\langle(a + a^\dagger)^2\rangle} \ll 1$ , we enter the so-called *Lamb-Dicke regime* [117]. We then expand the exponential terms in eqn. 1.32:

$$H_{\text{int}}^{\text{LD}} = \frac{\hbar\Omega}{2} \left[ e^{-i\Delta t} \left( \mathbb{1} + i\eta a e^{-i\omega_{\text{T}}t} + i\eta a^\dagger e^{i\omega_{\text{T}}t} \right) |e\rangle \langle g| + \text{h.c.} \right] \quad (1.35)$$

For low light intensities ( $\Omega \ll \omega_{\text{T}}$ ), we identify three distinct types of transitions which can be selected through the detuning parameter (see fig. 1.2): for  $\Delta = 0$ , the interaction Hamiltonian reduces to

$$H_{\text{int}}^{\text{car}} = \frac{\hbar\Omega}{2} (|e\rangle \langle g| + |g\rangle \langle e|), \quad (1.36)$$

describing the *carrier* transitions  $|g, n\rangle \leftrightarrow |e, n\rangle$  at Rabi frequency<sup>4</sup>  $\Omega_{\text{car}} = \Omega$ . Exciting these transitions does not change the motional state of the ion. On the other hand, choosing  $\Delta = -\omega_{\text{T}}$  yields

$$H_{\text{int}}^{\text{rsb}} = i\eta \frac{\hbar\Omega}{2} (|e\rangle \langle g| a - |g\rangle \langle e| a^\dagger), \quad (1.37)$$

and the *red-sideband* transitions  $|g, n\rangle \leftrightarrow |e, n-1\rangle$  is driven. Exciting the electronic degree of freedom from the ground to the excited state will thus remove one quantum of motion from the ion (satisfying energy conservation). Compared with carrier transitions, the Rabi frequency on  $|g, n\rangle \leftrightarrow |e, n-1\rangle$  is reduced to  $\Omega_{\text{rsb}} = \eta\sqrt{n}\Omega$ . Accordingly, for the detuning  $\Delta = \omega_{\text{T}}$ , *blue-sideband* transitions  $|g, n\rangle \leftrightarrow |e, n+1\rangle$  are driven with Rabi frequency  $\Omega_{\text{bsb}} = \eta\sqrt{n+1}\Omega$ .

---

<sup>4</sup>For an expansion of the exponential terms in eqn. 1.32 up to second order of  $\eta$ , we find the carrier Rabi frequency reduced to  $\Omega_{\text{car}} = \Omega \left( 1 - \eta^2 \left( n + \frac{1}{2} \right) \right)$ .

### 1.1.3 Laser cooling trapped ions

Motional-sideband transitions allow e.g. for entangling the motional and electronic degrees of freedom of a single ion [118], engineering arbitrary states of motion [107] and using the common motion of several ions as a bus between the ions' electronic states [102, 44, 45, 42, 39]. However, this is in general only possible after cooling them to low-lying motional states or even to the ground state.

Another motivation for cooling arises in the context of addressing the ion with high-NA optics. In our setup, the diffraction-limited spot sizes easily come down to  $1\ \mu\text{m}$  [112], and it becomes necessary to reduce the extent of the ion's spatial wave function as far below this value as possible.

For the interested reader, an extensive review of laser-cooling theory is found in [96]. Following this reference, I will present a simplified picture sufficient to describe the particular situation of our experiment.

#### General approach

Cooling an ion means removing both energy and entropy from its motional degree of freedom, a process of dissipative nature. The basic model introduced in section 1.1.2, however, takes only coherent processes into account. The dissipative part of laser cooling arises from the interaction of the ion not only with the laser but with the vacuum field as well, introducing the theory of spontaneous emission [119]. Its most important aspect for our purposes is the finite lifetime of an electronic state when coupled, e.g. through electric-dipole transitions, to lower-lying states. This means that a two-level system, initially prepared in the excited state  $|e\rangle$ , will decay to the ground state  $|g\rangle$  with a characteristic rate  $\Gamma$ , scattering a single photon into the vacuum field. By time-energy uncertainty, the finite lifetime of the excited state makes its energy less well-defined. In turn, this yields the natural transition linewidth  $\Gamma$ .

As explained in section 1.1.2, the ion's motional state is described in the Hilbert space for which the Fock states  $\{|n\rangle\}$  form a basis. Initially, the ion may be in some arbitrary (mixed) motional state. Considering a particular Fock state  $|n\rangle$ , we identify loss processes, that remove population from it, and gain processes, that add population. Fig. 1.3 illustrates these processes for the Lamb-Dicke regime, i.e. in first order of the Lamb-Dicke parameter  $\eta$ .

In order to describe the dynamics of the cooling process, we need to find an expression for the rate at which loss and gain processes of the population  $p_n$  take place. For an analytic approach, we make the assumption of not saturating the electronic transition by the laser field, i.e.  $\Omega \ll \Gamma$ . With this, we express the steady-state population of the excited state  $|e\rangle$  as [119]

$$\rho(\Delta) = \left(\frac{\Omega}{\Gamma}\right)^2 W(\Delta) \quad (1.38)$$

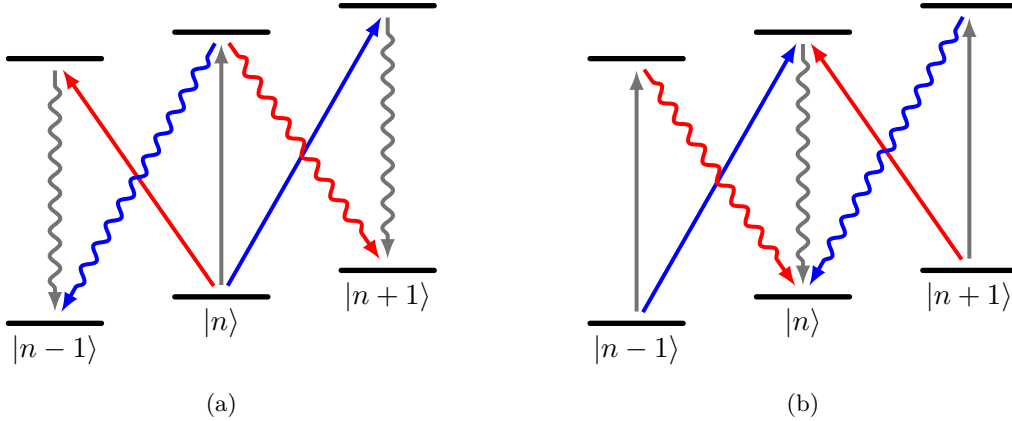


**Fig. 1.3:** Illustration of the (a) loss and (b) gain processes for the population  $p_n$  of the motional state  $|n\rangle$  in lowest order of the Lamb-Dicke parameter  $\eta$ .

with the line-shape function<sup>5</sup>

$$W(\Delta) = \frac{1}{1 + \left(\frac{\Delta}{\Gamma/2}\right)^2} \quad (1.39)$$

for a given detuning  $\Delta$  from the carrier transition. With these quantities, tab. 1.1 details the individual processes changing the population  $p_n$  of state  $|n\rangle$ . With the cooling rate  $A_-$  and heating rate  $A_+$ , defined as

$$A_- = \eta^2 \Gamma \left(\frac{\Omega}{\Gamma}\right)^2 (W(\Delta) + W(\Delta + \omega_T)) \quad (1.40)$$

$$A_+ = \eta^2 \Gamma \left(\frac{\Omega}{\Gamma}\right)^2 (W(\Delta) + W(\Delta - \omega_T)), \quad (1.41)$$

we write down the system of differential equations for the populations  $p_n$ :

$$\dot{p}_n = -n A_- p_n - (n+1) A_+ p_n + (n+1) A_- p_{n+1} + n A_+ p_{n-1} \quad (1.42)$$

For the moment, we are not interested in the actual distribution  $p_n$  of the populations, but only the expectation value  $\langle n \rangle = \sum_n n p_n$  of the motional quantum number  $n$ . Using eqn. 1.42, we readily obtain the differential equation

$$\frac{d}{dt} \langle n \rangle = -(A_- - A_+) \langle n \rangle + A_+. \quad (1.43)$$

Integrating this equation yields the solution

$$\langle n \rangle(t) = \langle n \rangle(0) e^{-Rt} + \langle n \rangle_{ss} (1 - e^{-Rt}) \quad (1.44)$$

<sup>5</sup>For multilevel atoms, exhibiting more complex excitation spectra, the line-shape function must be replaced accordingly.

Process	Involved transitions	$\dot{p}_n (\eta^2 \Gamma (\Omega/\Gamma)^2)$
Loss through cooling	$ g, n\rangle \rightarrow  e, n\rangle \rightarrow  g, n-1\rangle$	$-n W(\Delta)$
	$ g, n\rangle \rightarrow  e, n-1\rangle \rightarrow  g, n-1\rangle$	$-n W(\Delta + \omega_T)$
Loss through heating	$ g, n\rangle \rightarrow  e, n\rangle \rightarrow  g, n+1\rangle$	$-(n+1) W(\Delta)$
	$ g, n\rangle \rightarrow  e, n+1\rangle \rightarrow  g, n+1\rangle$	$-(n+1) W(\Delta - \omega_T)$
Gain through cooling	$ g, n+1\rangle \rightarrow  e, n+1\rangle \rightarrow  g, n\rangle$	$(n+1) W(\Delta)$
	$ g, n+1\rangle \rightarrow  e, n\rangle \rightarrow  g, n\rangle$	$(n+1) W(\Delta + \omega_T)$
Gain through heating	$ g, n-1\rangle \rightarrow  e, n-1\rangle \rightarrow  g, n\rangle$	$n W(\Delta)$
	$ g, n-1\rangle \rightarrow  e, n\rangle \rightarrow  g, n\rangle$	$n W(\Delta - \omega_T)$

**Tab. 1.1:** Detailed loss and gain processes for the population  $p_n$  of the motional state  $|n\rangle$  in lowest order of the Lamb-Dicke parameter. The relevant quantity is the time derivative  $\dot{p}_n$ , given in units of the Lamb-Dicke parameter  $\eta$ , Rabi frequency  $\Omega$  and linewidth  $\Gamma$ .

with the effective cooling rate  $R := A_- - A_+$  and the steady-state value

$$\langle n \rangle_{\text{ss}} := \langle n \rangle (t \rightarrow \infty) = \frac{A_+}{A_- - A_+}. \quad (1.45)$$

Note that this is a meaningful solution only for  $A_- > A_+$ . This corresponds to the basic idea of laser cooling, namely making transitions which lower the ion's kinetic energy more likely than those which raise it.

In the following, I will discuss two limiting cases, Doppler cooling ( $\Gamma \gg \omega_T$ ) and resolved-sideband cooling ( $\Gamma \ll \omega_T$ ).

### Doppler cooling

The term *Doppler cooling* is originally associated with laser cooling free or weakly bound atoms. This means that the laser cannot resolve the motional sidebands of the electronic transition as the atomic excitation spectrum covers many of the sideband transitions ( $\Gamma \gg \omega_T$ ).

We are now interested in the optimal choice for the laser detuning  $\Delta$  for the minimal steady-state value  $\langle n \rangle_{\text{ss}}$  of the mean motional quantum number. By the definition of the rates  $A_-$  and  $A_+$ , we find

$$\langle n \rangle_{\text{ss}} = \frac{W(\Delta) + W(\Delta - \omega_T)}{W(\Delta + \omega_T) - W(\Delta - \omega_T)}. \quad (1.46)$$

Minimizing this expression yields the well-known result for the optimal detuning:

$$\Delta_D = -\frac{\Gamma}{2} \quad (1.47)$$

This is the Doppler limit, and the steady-state value of  $\langle n \rangle$  and the effective cooling rate<sup>6</sup>

<sup>6</sup>Note that the maximal value for the effective cooling rate  $R$  is not found at  $\Delta = -\frac{\Gamma}{2}$  but at  $\Delta = -\frac{\Gamma}{2\sqrt{3}}$ .

become

$$\langle n \rangle_{\text{ss,D}} = \frac{1}{2} \left( \frac{\Gamma}{\omega_{\text{T}}} - 1 \right) \approx \frac{\Gamma}{2\omega_{\text{T}}} \quad (1.48)$$

and

$$R_{\text{D}} = 2\eta^2 \omega_{\text{T}} \left( \frac{\Omega}{\Gamma} \right)^2. \quad (1.49)$$

From the relation  $\frac{1}{2}k_{\text{B}}T = \langle E_{\text{kin}} \rangle = \frac{1}{2} \langle E \rangle$  between temperature  $T$ , kinetic energy  $E_{\text{kin}}$  and total energy  $E$ , we derive the Doppler temperature

$$T_{\text{D}} = \frac{\hbar \Gamma}{2k_{\text{B}}}. \quad (1.50)$$

This is the minimal temperature that can be achieved for weakly bound atoms ( $\Gamma \gg \omega_{\text{T}}$ ).

### Resolved-sideband cooling

In the opposite limiting case,  $\Gamma \ll \omega_{\text{T}}$ , the laser resolves the individual motional sidebands from the carrier transition. While the spontaneous-decay processes are left unchanged, the manner of absorption is significantly altered.

For the case of Doppler cooling, the laser excites many sideband transitions, and tuning its frequency brings about only a small imbalance in the absorption rates for the red and blue sidebands. However, resolving the individual sidebands strongly favors excitations on a particular sideband or the carrier transition.

Typically, the laser is tuned to the first motional sideband, i.e.  $\Delta = -\omega_{\text{T}}$ . This means that for almost every excitation  $|g, n\rangle \rightarrow |e, n-1\rangle$  from the electronic ground state, one quantum of motion is removed from the ion, since, in the Lamb-Dicke regime, spontaneous emission occurs mainly on the carrier transition. The steady-state value  $\langle n \rangle_{\text{ss}}$  then takes the form

$$\langle n \rangle_{\text{ss}} = \frac{W(-\omega_{\text{T}}) + W(-2\omega_{\text{T}})}{W(0) - W(-2\omega_{\text{T}})} \quad (1.51)$$

$$= \frac{5}{16} \left( \frac{\Gamma}{\omega_{\text{T}}} \right)^2 \quad (1.52)$$

$$\approx \left( \frac{\Gamma/2}{\omega_{\text{T}}} \right)^2 \ll 1, \quad (1.53)$$

with the effective cooling rate

$$R = \eta^2 \Gamma \left( \frac{\Omega}{\Gamma} \right)^2. \quad (1.54)$$

This means that resolved-sideband cooling facilitates motional ground-state cooling, i.e. a steady state with a population close to unity in the state  $|n=0\rangle$ .

### Thermal state

So far, we have been interested only in the mean value  $\langle n \rangle$  of the motional quantum number. However, it is instructive to examine also the distribution of the individual

states  $|n\rangle$ . Once the steady state has been reached, the distribution no longer depends on the initial quantum state.

We now make the assumption of *detailed balance* [120], i.e. we assume all loss and gain processes for a given population  $p_n$  to cancel out ( $\dot{p}_n = 0$ ). It is sufficient to consider only processes exchanging population of the state  $|n\rangle$  with one of the neighboring states, e.g.  $|n-1\rangle$ . We then arrive at the equation

$$\dot{p}_n = -\eta^2 \Gamma_n A_- p_n + \eta^2 \Gamma_{n-1} A_+ p_{n-1} \stackrel{!}{=} 0, \quad (1.55)$$

which directly yields

$$\frac{p_n}{p_{n-1}} = \frac{A_+}{A_-} \quad (1.56)$$

$$= \frac{\langle n \rangle}{\langle n \rangle + 1}. \quad (1.57)$$

This gives us the explicit form

$$p_n = \frac{\langle n \rangle^n}{(\langle n \rangle + 1)^{n+1}} \quad (1.58)$$

for the population of state  $|n\rangle$ , which is nothing but a Boltzmann (thermal) distribution.

#### 1.1.4 Atomic level scheme

The atomic species which we use in our setup is singly ionized calcium-40 ( $^{40}\text{Ca}^+$ ). It possesses no nuclear spin and thus no hyperfine structure. The five fine-structure manifolds relevant to our experiments are depicted in fig. 1.4. Details of the atomic states and transitions are given in app. A.1.

Apart from a stable  $S_{1/2}$  ground state, two short-lived and two long-lived (metastable) states are present. The  $P_{1/2}$  and  $P_{3/2}$  state each have a natural lifetime of  $\sim 7$  ns [121] and allow scattering light at high rate, e.g. for Doppler cooling. At the same time, the  $D_{3/2}$  and  $D_{5/2}$  lifetimes amount to  $\sim 1.2$  s [122], making the latter state well suited to form an optical qubit with the  $S_{1/2}$  state when manipulations occur on a  $\mu\text{s}$  or  $\text{ms}$  time scale.

#### 397/866 nm transition

The transition at 397 nm wavelength is a strong electric-dipole transition with a natural linewidth of 22.4 MHz (given by the  $P_{1/2}$ -state lifetime). As the  $P_{1/2}$  branching fraction amounts to 93.6 % on this transition [123], it is well suited for laser (Doppler) cooling and making the ion visible.

Apart from cooling the ion's motion, detecting light scattered on the 397 nm transition allows for efficient discrimination between the  $S_{1/2}$  and  $D_{5/2}$  state (see section 2.1.3). This provides a means of projecting the optical qubit onto the  $S_{1/2}$ - $D_{5/2}$  basis.

To prevent optical pumping to the long-lived  $D_{3/2}$  state, a repumping laser at 866 nm wavelength is needed.

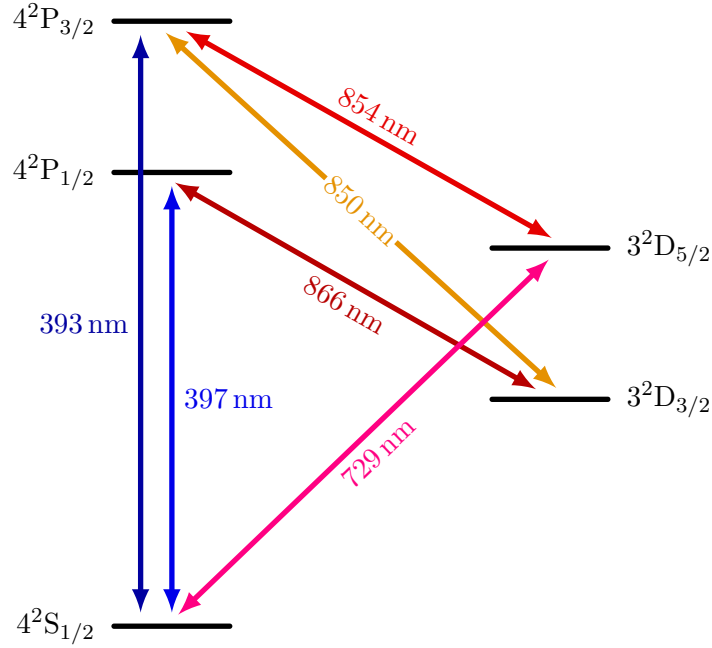


**Fig. 1.4:** Energy-level scheme of  $^{40}\text{Ca}^+$  with the lowest-lying fine-structure manifolds and all relevant optical transitions with their respective wavelengths.

### 729 nm transition

The electric-quadrupole transition at 729 nm wavelength couples the metastable  $D_{5/2}$  with the  $S_{1/2}$  ground state, resulting in the very small natural linewidth of 136 mHz. This makes it interesting for high-precision spectroscopic experiments [124] and optical clocks [100, 125]. For our purposes it is the transition used to address the qubit formed by the  $S_{1/2}$  and  $D_{5/2}$  state. Owing to the long lifetimes of the two states, long qubit coherence times have been demonstrated [126].

## 1.2 Experimental setup

The centerpiece of our experimental system are two ultra-high-vacuum chambers, each holding a linear Paul trap. The chambers are mounted on an optical table at  $\sim 1$  m distance (see fig. 1.5). Single ions are trapped independently and simultaneously in the two chambers. For historic reasons, the traps are called “Bright Trap” and “Dark Trap”.

For the major part, the laboratory was set up by Felix Rohde, Carsten Schuck, Marc Al-mendros and Markus Hennrich at the Institute of Photonic Sciences (ICFO) in Barcelona, Spain. Their Ph.D. theses [127, 112] document very well the details of the setup.

In 2010, the entire setup was moved to Saarland University in Saarbrücken. Regular work in the laboratory was resumed in 2011.

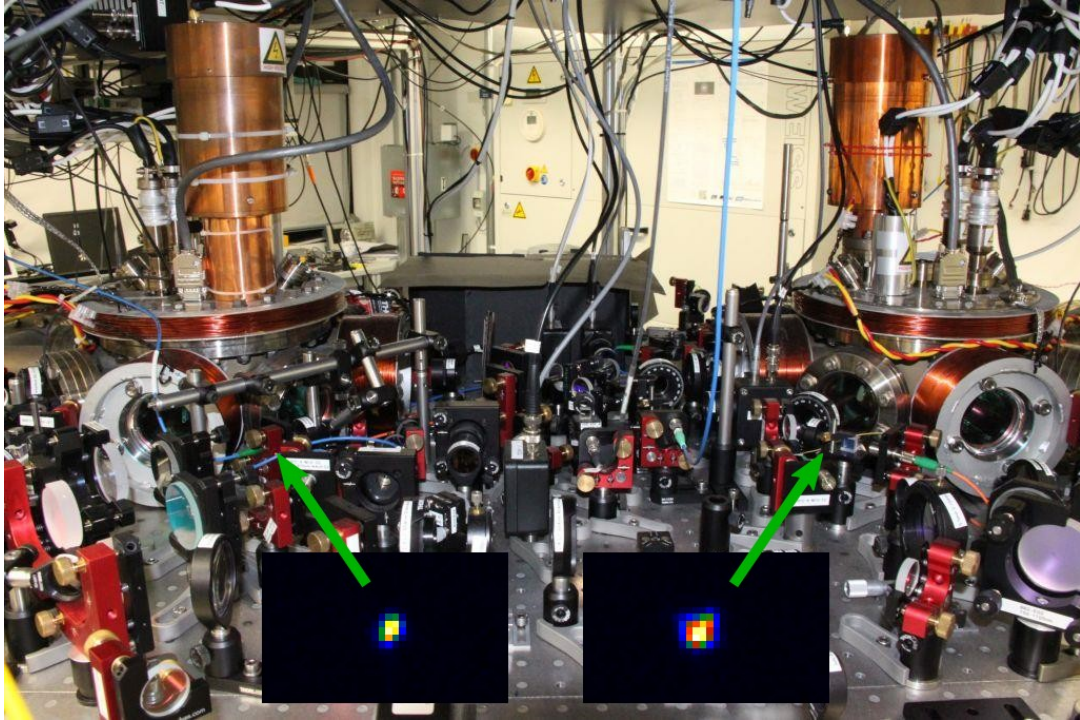


**Fig. 1.5:** Optical table with the vacuum chambers holding the linear Paul traps (picture taken at Saarland University). Left chamber: Dark Trap, right chamber: Bright Trap.

### 1.2.1 Trap apparatus

We operate two linear Paul traps which were designed in the *Quantum Optics and Spectroscopy Group* of Rainer Blatt at the University of Innsbruck [128, 111]. They were machined from nonmagnetic stainless steel and are compatible with ultra-high vacuum conditions.

The values for half the distance between opposing trap blades and the end tips are  $r_0 = 0.8$  mm and  $l_0 = 2.5$  mm, respectively, and the geometry factor (see eqn. 1.4) amounts to  $\alpha = 0.183$ .

#### Trap parameters

The experiments presented in this thesis were almost exclusively carried out with ions in the Bright Trap. For an end-tip voltage  $U_{\text{tip}} = 400$  V, we obtain the axial secular frequency  $\omega_z = 2\pi \cdot 1.20$  MHz. The trap is operated at the radio frequency  $\Omega = 2\pi \cdot 26.1$  MHz with an input power of 9.6 W. This corresponds to a radio-frequency voltage amplitude  $U_{\text{RF}} = 1.48$  kV applied to the blade electrodes and yields radial secular frequencies  $\omega_x = \omega_y = 2\pi \cdot 3.72$  MHz.

From these quantities, we extract the stability parameters  $a_x = a_y = -0.00420$ ,  $a_z = 0.00840$  and  $|q_x| = |q_y| = 0.413$  ( $q_z = 0$  by definition).

### Magnetic-field control

For most experiments, in addition to fundamental prerequisites like laser cooling, a static magnetic field at the position of the trapped ion is needed. To this end, three pairs of coils with mutually orthogonal axes were attached to each vacuum chamber [127]. This allows us to align the magnetic field along virtually any direction and to compensate for stray magnetic fields.

The coil current is controlled through commercial power supplies<sup>7</sup> with  $\sim 100 \mu\text{A}$  long-term stability. Typically, we operate the coils at 1 – 3 A current, yielding magnetic-field strengths of 3 – 6 G (depending on which pair of coils is used).

### 1.2.2 Optical access

Almost all interactions with an ion are carried out optically. This includes excitation through laser beams, which are typically focused onto the ion through standard lenses with focal lengths of 250 – 500 mm (with collimated-beam diameters of 1 – 2 mm). In addition, the ion is interfaced with light at the single-photon level with objectives of high numerical aperture (NA), as discussed in the next paragraph.

### HALOs

When interfacing single ions with light at the level of single photons, it is essential to use optics which subtend a large solid angle around the ion. Our approach is to use a pair of high-NA laser objectives (HALOs) in each vacuum chamber [84, 112]. Like the trap, they are mounted to the top flange of the chamber (see fig. 1.6). Three-axis piezo actuators integrated in the mounts allow moving the HALOs along all three axes in order to align them with the ion.

The HALOs have a numerical aperture of 0.4, subtending  $\sim 4.2\%$  of the total solid angle, a focal length of 25 mm and are diffraction limited and anti-reflection coated over the entire optical spectrum relevant for our atomic species (393 – 866 nm). Typical minimum spot diameters are 1.2  $\mu\text{m}$  at 397 nm and 2.6  $\mu\text{m}$  at 866 nm.

### Fluorescence detection

Light emitted by the ion is collected through one or both HALOs and then detected by either single-photon detectors or a camera [112].

Blue light from the ion is coupled to multi-mode optical fibers with  $\sim 85\%$  transmission and detected by photomultiplier tubes<sup>8</sup> (PMTs) of 28(1) % quantum efficiency. For isotropic emission, this yields a total detection efficiency of  $\sim 1\%$ . On the other hand, red light is coupled to single-mode fibers with  $\sim 60\%$  transmission and detected by avalanche photodiodes<sup>9</sup> (APDs) of 24(5) % quantum efficiency, yielding a total detection efficiency of  $\sim 0.6\%$ .

---

<sup>7</sup>Aim-TTi, QL355

<sup>8</sup>Hamamatsu, H7422P-40SEL

<sup>9</sup>Laser Components, COUNT-10C-FC

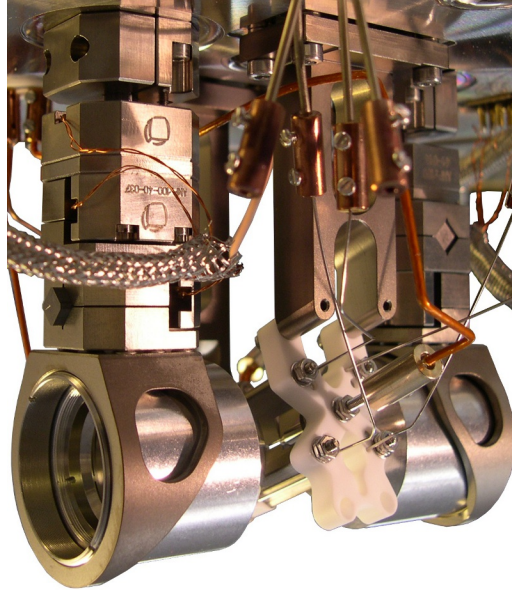


**Fig. 1.6:** Linear Paul trap for confining single ions. The two high-NA objectives mounted next to it can be moved along all three axes for alignment.

While loading ions into the trap, the fluorescence light is not fiber coupled but directly imaged onto an EMCCD camera<sup>10</sup>.

### 1.2.3 Laser system

Even in the absence of hyperfine splitting,  $^{40}\text{Ca}^+$  provides a rich structure of energy levels. Turning this into a useful feature requires control over almost all optical transitions. Except for the dipole transition at 393 nm wavelength<sup>11</sup>, lasers to control all wavelengths denoted in fig. 1.4 are available. All lasers in our laboratory are extended-cavity diode lasers (ECDLs) with a grating in Littrow configuration for optical feedback [129]. Unless specified otherwise, the spectral linewidths are 100 – 300 kHz. Details on the laser system are found in [127, 130].

#### Laser at 397 nm

The laser<sup>12</sup> to address the electric-dipole transition used for cooling and state discrimination runs at 794 nm wavelength. Its light is amplified in a tapered amplifier before being frequency doubled through a nonlinear crystal in an optical cavity. The typical output power amounts to 30 – 40 mW.

<sup>10</sup>Andor, iXon DV887DCS-BV

<sup>11</sup>A diode laser at 393 nm wavelength is currently being set up.

<sup>12</sup>Toptica, TA-SHG pro

### Lasers at 850/854/866 nm

The lasers<sup>13</sup> mainly used for repumping population from the metastable atomic states ( $D_{3/2}$ ,  $D_{5/2}$ ) are diode lasers with typical output powers of  $\sim 40$  mW. As these powers are sufficient for our purposes, no additional amplification stages are needed.

### Transfer lock

As with most lasers, diode lasers show spectral drifts which become too large for our purposes on a time scale of seconds to minutes. In addition, it is favorable to reduce their linewidth, which is typically 1 – 2 MHz when free-running. To this end, our group devised an active stabilization scheme termed “transfer lock” [127, 131, 130]. The principle is to stabilize the lengths of a number of optical resonators (“transfer cavities”) to a master laser which itself is stabilized to an absolute atomic reference. Then all of the above-mentioned lasers (397/850/854/866 nm) are stabilized each to one of the transfer cavities.

Both the transfer cavities and the lasers, including the master laser, are stabilized to their respective reference through the Pound-Drever-Hall technique [132]. The master laser runs at 852 nm wavelength and is referenced to a cesium atomic-vapor cell ( $D_2$  line) through Doppler-free absorption spectroscopy. This provides the necessary long-term stability for the other lasers. However, barometric changes during the course of the day result in a change of the effective lengths of the transfer cavities (which are not placed in vacuum) and hence in a shift of their resonance frequencies. Therefore, spectroscopy in order to calibrate the laser wavelengths must be performed on the ion every morning (see section 2.4). On the other hand, the feedback on the lasers through the Pound-Drever-Hall method allows to reduce their linewidths from 1 – 2 MHz to 100 – 300 kHz.

### Laser at 729 nm

The laser used for coherent manipulation of the  $S_{1/2}$ – $D_{5/2}$  qubit transition is an amplified ECDL<sup>14</sup> providing up to 500 mW of optical power. In order to make use of the potentially long coherence time of the atomic qubit, the laser itself is required to be very narrow-band and have good long-term stability. As the transfer lock does not offer this to a sufficiently high degree, the laser is stabilized to a high-finesse optical cavity with a linewidth of 4 kHz and a long-term drift of 80 mHz/s. The stabilization is accomplished by a very fast feedback loop through the Pound-Drever-Hall technique and yields a laser linewidth  $< 30$  Hz.

The laser as well as the high-finesse cavity were mostly set up by Jan Huwer and are accordingly described in his Ph.D. thesis [94]. I will give a brief overview of the laser system in section 2.1.1.

---

<sup>13</sup>Toptica, DL pro

<sup>14</sup>Toptica, TA pro

### Laser for photoionization

For loading single ions into one of the Paul traps, we employ a photoionization scheme [112] as an alternative to a thermionic emitter (“electron gun”). This allows us to efficiently select the desired isotope  $^{40}\text{Ca}^+$  from calcium with natural isotope abundance.

A resistively heated oven filled with metallic calcium granules directs a beam of neutral calcium atoms through the trap center. A free-running ECDL at 846 nm wavelength with a high-power diode<sup>15</sup> ( $\sim 130$  mW output power) is frequency doubled to 423 nm in a nonlinear crystal (single pass). The light is coupled to a multi-mode optical fiber, sending it through the trap center where it excites the calcium atoms on the  $4^1\text{S}_0-^1\text{P}_1$  transition. Light from a high-power LED<sup>16</sup> (70 – 85 mW output power) with 380 nm central wavelength is coupled to the same fiber and excites the atoms from the  $^1\text{P}_1$  state to Rydberg states, from where they are ionized through the electric fields present in the Paul trap (field ionization).

### Wavelength monitoring

A small portion of the light from each laser is sent to a wavelength meter<sup>17</sup>. An optical multi-channel switch multiplexes eight different sources of light into the wavelength meter in order to continuously monitor the wavelength values. Although the accuracy of the wavelength meter itself amounts to 60 MHz for our wavelength range, the effective accuracy is reduced to 150 MHz since we need to use a multi-mode optical fiber connecting the switch to the wavelength meter in order to accommodate all laser wavelengths.

### Acousto-optic modulators

Even simple quantum-optical experiments require the ability to control frequency, phase and power of the laser beams in a precise and fast manner. This is done through commercial acousto-optic modulators<sup>18</sup> (AOMs), set up in double-pass configuration. They are used e.g. for scanning the laser frequency when performing spectroscopy, active stabilization of the laser power at the position of the ion and fast switching of lasers during pulsed experimental sequences.

#### 1.2.4 Experimental control unit

As mentioned in the previous section, already simple quantum-optical experiments require fast and precise control over frequency, phase and power of the laser beams interacting with the ion. More complex experiments also require the ability to react to events like the detection of photons or the atomic-state read-out of the ion.

For this purpose, Marc Almendros dedicated part of his Ph.D. [131] to develop a versatile and modular backplane-based bus system, called *Hydra*. A digital signal processor

---

<sup>15</sup>Toptica, DL 100

<sup>16</sup>Nichia, NCCU001

<sup>17</sup>HighFinesse, WS/7 Super Precision

<sup>18</sup>Brimrose/IntraAction, various models

(DSP) controls up to 13 radio-frequency (RF) synthesizers which, on their part, control the laser beams through AOMs.

The core of each RF card is a direct digital synthesizer (DDS) which generates an RF signal with frequencies of 4.5 – 300 MHz and controlled phase. This signal is then passed through a digital-to-analog converter (DAC) which defines the signal amplitude. If required, a switchable attenuator provides an additional suppression of the signal by  $\sim 50$  dB. A field-programmable gate array (FPGA) controls the RF module with 80 MHz update rate (equivalent to 12.5 ns time base) and communicates with the DSP via the backplane. All DDSs are phase locked to an atomic clock<sup>19</sup> and facilitate phase-coherent frequency switching. In addition, some of the modules are equipped with an analog input channel which can read out photodiodes to measure the power of laser beams. Feedback onto the corresponding AOM thus allows to stabilize the optical power.

Furthermore, the DSP features 8 general-purpose counters (GPCs), 16 digital input (DI) and 16 digital output (DO) channels. The GPCs allow counting pulses from single-photon detectors for atomic spectroscopy and atomic-state detection. The DI channels are used to trigger an experimental sequence to an external event, e.g. the 50 Hz power-line signal. The DO channels, on the other hand, provide trigger signals for other experimental devices.

This version of Hydra lacks the ability to temporally resolve pulses from single-photon detectors. We thus time-tag photon-detection events through a commercial time-correlated single-photon counter<sup>20</sup>.

---

<sup>19</sup>Stanford Research Systems, FS725

<sup>20</sup>PicoQuant, PicoHarp 300



## Chapter 2

# Experimental tools for quantum-state manipulation

After an introduction to the theoretical and experimental principles in the first chapter, I will now present the experimental methods and tools required for the control and manipulation of the atomic quantum state. This includes a narrow-band laser resonant with the optical qubit transition, whose principle of operation will be explained briefly, followed by a characterization of the qubit itself. Besides the optical qubit, I will present a qubit formed by two Zeeman states coupled by a radio-frequency transition and addressed through a magnetic field, which offers certain advantages over the optical qubit. Furthermore, optical-pumping methods are introduced that are indispensable for initializing the atomic qubit in a pure quantum state. The chapter concludes with sections regarding spectroscopic methods for the calibration of laser frequencies and a technique for precise determination of the ion's temperature in the trap.

### 2.1 Coherent manipulations – optical qubit

As explained in section 1.1.4, the  $S_{1/2}$  ground state and the metastable  $D_{5/2}$  state form an optical qubit at 729 nm transition wavelength. The external static magnetic field lifts the degeneracy of the Zeeman states of the two fine-structure manifolds (see fig. 2.1). By virtue of different Landé factors of the two manifolds, the ten transitions allowed by electric-quadrupole selection rules ( $\Delta m_J = 0, \pm 1, \pm 2$ ) all have distinct resonance frequencies and can thus be addressed individually.

Exploiting the potentially long coherence time of the qubit [126], however, requires a very narrow-band and stable laser. After a brief overview of how to set up such a laser system, basic experimental concepts like the experimental sequence, probability estimation for atomic populations, spectroscopy and Rabi oscillations will be explained. As the qubit coherence time is limited also by fluctuations of the ambient magnetic field, a method to estimate these fluctuations will be introduced.

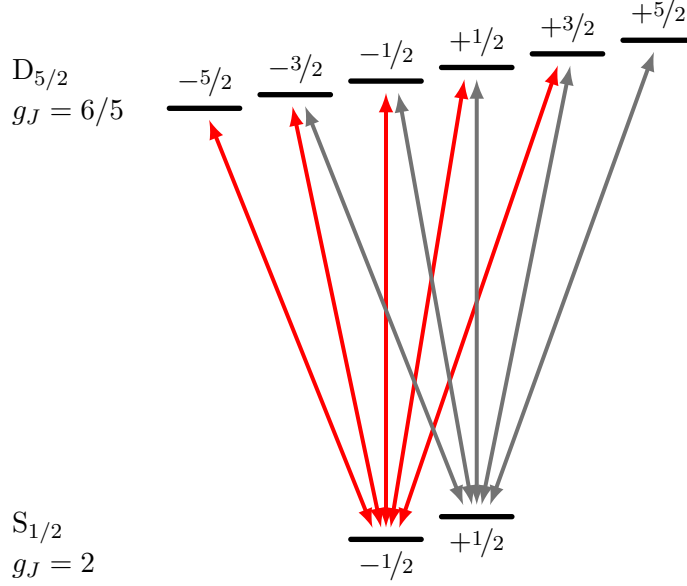


**Fig. 2.1:** Electric-quadrupole transitions between the Zeeman states of the  $S_{1/2}$  and  $D_{5/2}$  manifold. Denoted to the left are the Landé factors for each manifold, indicating the splitting of the Zeeman energy level in an external magnetic field.

### 2.1.1 Qubit laser at 729 nm

Within the framework of this thesis, the laser for controlling the optical-qubit transition was used for tasks such as unitary rotations on the Bloch sphere (see section 2.1.6), electron shelving (section 2.1.5 and app. A.2) and ion-temperature measurements (section 2.5). For the largest part, the laser was set up by Jan Huwer, who gives a detailed description in his Ph.D. thesis [94].

#### Amplified diode laser

As mentioned in section 1.2.3, the laser itself is an extended-cavity diode laser<sup>1</sup> with an integrated tapered amplifier and runs at 729.1467 nm (wavelength in air). A diffraction grating set up in Littrow configuration reflects the light in the first order of diffraction back into the diode, forming a laser cavity in addition to the one given by the two facets of the diode. Light from the zeroth diffraction order is then available as output. As with all our diode lasers, the free-running laser shows a linewidth on the order of 1 MHz.

A piezo actuator allows for tilting the diffraction grating and thus for tuning the laser frequency over the entire gain profile of the laser diode. As the bandwidth of the piezo is limited by its own resonance frequencies, which are in the range of 1 – 10 kHz, we use it to compensate slow drifts of the laser frequency. In order to achieve a narrow laser bandwidth, however, a fast feedback loop is required. This is facilitated by controlling the current through the laser diode itself.

<sup>1</sup>Toptica, TA pro

In order to achieve a sufficiently narrow bandwidth and good long-term stability, a frequency reference with just these properties is needed. Progress in the field of optical resonators nowadays provides cavities of very high finesse ( $10^5 - 10^6$ ) [133, 134] and thus, depending on the free spectral range, very small linewidths.

### High-finesse optical cavity

The optical cavity used to stabilize our qubit laser is a vertically and midplane mounted model from Advanced Thin Films. Its spectral linewidth was determined from a ring-down measurement to be 4.0 kHz. Together with 1.9 GHz free spectral range, this determines the cavity finesse to 480 000.

For good long-term stability (minutes to hours), the cavity spacers are made from ultra-low-expansion glass from Corning. This material has the property of a vanishing linear thermal expansion coefficient at a certain temperature. For our cavity, we found this to be at 22.3 °C. In addition, the cavity is placed inside an ultra-high-vacuum chamber for passive thermal isolation. Together with an active temperature stabilization realized with heater mats and Peltier elements, this provides a temperature stability on the order of 1 mK. To protect the cavity from acoustic noise, the vacuum chamber is placed on a passive vibration-damping platform<sup>2</sup>.

With all these measures taken, the only remaining effect degrading the long-term stability is aging of the cavity spacers, which cannot be circumvented by any means available to us. As the cavity is mounted vertically, gravity continuously changes the cavity-spacer length, shifting the resonance frequency by 80 mHz/s. However, this effect is usually negligible when it comes to addressing the ion with the qubit laser, as other effects, e.g. magnetic-field fluctuations, play greater roles. Hence it is sufficient to calibrate the laser frequency only once per day through atomic spectroscopy.

### Laser stabilization

We employ the well-established technique developed by Robert Pound and refined by Ronald Drever and John Hall [132] for stabilizing the qubit laser to the high-finesse cavity.

A small portion of the light from the laser is phase modulated by sending it through an electro-optic modulator (EOM) running at 20 MHz frequency. It is then coupled into the high-finesse cavity (TEM<sub>00</sub> mode), and the reflected part is detected with a fast photodiode. This signal is mixed with the local oscillator driving the EOM. Low-pass filtering the mixed signal then provides the error signal for feedback onto the laser frequency. It is fed into a high-speed analog controller<sup>3</sup> with a fast circuit branch for reducing the laser linewidth via the diode current and a slow branch for eliminating low-frequency drifts via the grating piezo.

The Pound-Drever-Hall technique proved to be very well suited for our purposes, yielding both a narrow laser linewidth ( $< 30$  Hz) and good long-term operation.

---

<sup>2</sup>Minus K, 100BM-4

<sup>3</sup>Toptica, FALC 110

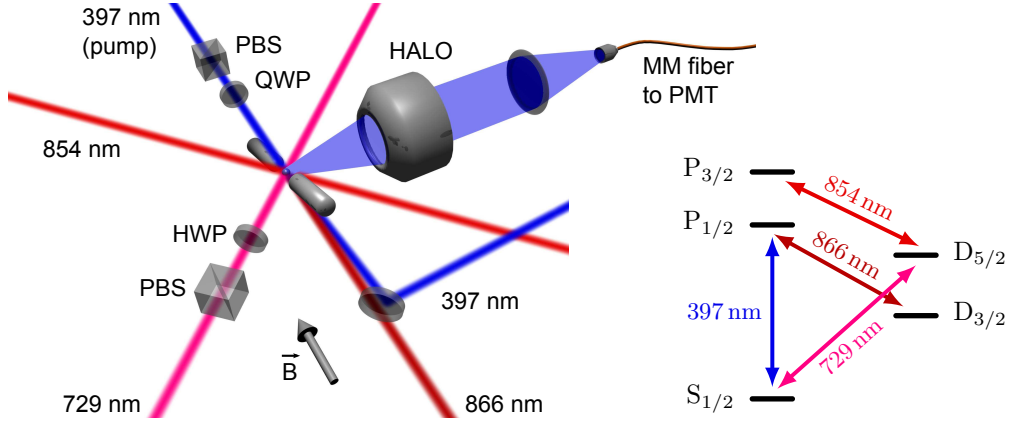


**Fig. 2.2:** Experimental setup for coherent manipulations on the optical qubit transition.  $\vec{B}$ : magnetic-field direction, HWP: half-wave plate, QWP: quarter-wave plate, PBS: polarizing beam-splitter cube, MM fiber: multi-mode optical fiber, PMT: photomultiplier tube. For clarity, the trap blades are not shown.

### 2.1.2 Experimental sequence

For coherent manipulations of the optical qubit, we use the experimental setup sketched in fig. 2.2. A single ion is addressed through a beam from the 729 nm qubit laser at  $45^\circ$  angle<sup>4</sup> with respect to the quantization axis defined by a static magnetic field  $\vec{B}$  (with a typical magnitude of  $B_{\text{stat}} \approx 3$  G). Under this angle, all ten transitions between the Zeeman states can be driven, their relative strengths defined by the light polarization which is set through a half-wave plate. A circularly polarized pump beam at 397 nm along the quantization axis prepares the ion in a pure quantum state prior to any coherent manipulations. Doppler cooling and state detection based on observation of fluorescence are performed through beams at 397 nm and 866 nm wavelength. A beam at 854 nm is used for repumping population from the  $D_{5/2}$  back to the  $S_{1/2}$  manifold after state detection. Fluorescence light at 397 nm from the ion is collected through one of the HALOs, coupled into a multi-mode optical fiber and detected by a photomultiplier tube.

#### Sequence timing

The timing of a typical experimental sequence is shown in fig. 2.3. First, the qubit is initialized by a pulse of light driving only the  $\sigma^-$  transition at 397 nm. This pumps the atomic population to the  $|S_{1/2}, m = -1/2\rangle$  state with  $\sim 99.9\%$  probability (see section 2.3.1). Subsequently, the 729 nm laser carries out the coherent manipulations on the qubit transition. This can include atomic spectroscopy, pulse-length scans, Ramsey experiments or more complex pulse sequences. Afterwards, the PMTs are gated on and state detection is performed by switching on the 397 nm and 866 nm laser. The detection of fluorescence from the ion then projects its quantum state onto the  $S_{1/2}$  and the absence of fluorescence

<sup>4</sup>The corresponding Lamb-Dicke parameters for the three trap axes are thus calculated as  $\eta_x = \eta_y = 0.036$  and  $\eta_z = 0.063$ .

## 2.1. Coherent manipulations – optical qubit

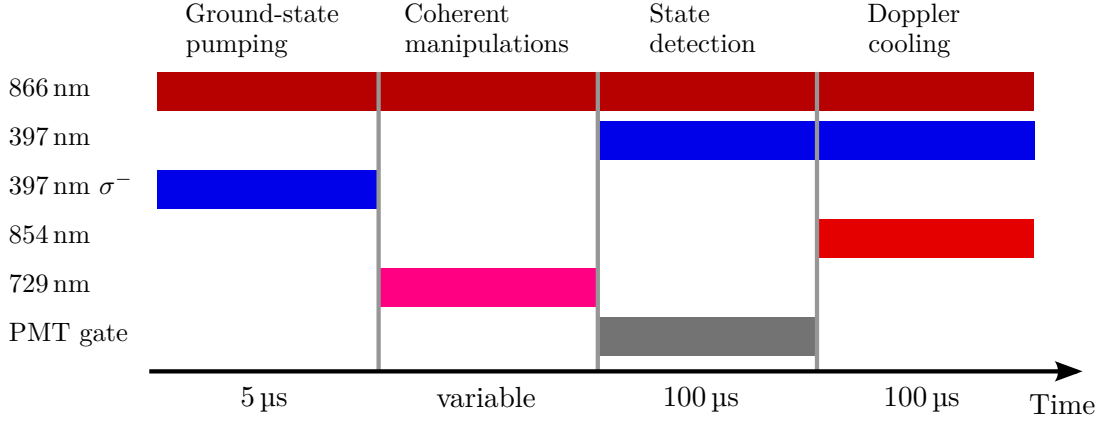


**Fig. 2.3:** Timing chart of a typical experimental sequence for coherently manipulating the optical qubit at 729 nm. The single laser pulse at 729 nm may be replaced by more complex pulse sequences.

onto the  $D_{5/2}$  manifold. Finally, the 854 nm laser is turned on to repump any population from  $D_{5/2}$  back to  $S_{1/2}$ . This allows for Doppler cooling the ion and subsequent ground-state pumping in the next sequence cycle.

### 2.1.3 Internal-state discrimination

As explained in the previous section, coherent manipulations of the atomic state are followed by a projection onto the basis formed by the  $S_{1/2}$  and  $D_{5/2}$  manifold. For that purpose, the cooling lasers are switched on and atomic fluorescence is collected through one of the HALOs and detected by a PMT. Since the  $D_{5/2}$  manifold is not addressed by the cooling lasers, a projection onto this state leaves the ion dark, and only detector dark counts and laser stray light are detected by the PMT (at rate  $R_d$ ). On the other hand, a projection onto  $S_{1/2}$  puts the ion in a bright state, scattering fluorescence light which is detected (at rate  $R_b$ ).

We then perform state discrimination by integrating the detector counts for a certain period (integration time) of length  $T$ . Receiving more counts than a given threshold  $n_{th}$  corresponds to the bright state, otherwise we assign the dark state to the ion. Our goal is to minimize the integration time, so the sequence runs at the highest possible repetition rate, while still being able to distinguish sufficiently well between the bright and dark state. Our criterion is the error probability  $\varepsilon$  to either identify the ion as dark while in the bright state or as bright while in the dark state. When not making any assumptions on the probability for the bright/dark state, the error probability is given by

$$\varepsilon = \frac{1}{2} [F(n_{th}, \bar{n}_b) + (1 - F(n_{th}, \bar{n}_d))] \quad (2.1)$$

with the Poisson cumulative distribution function

$$F(n, \lambda) = e^{-\lambda} \sum_{k=0}^n \frac{\lambda^k}{k!} \quad (2.2)$$

and expectation values  $\bar{n}_b = R_b T$  and  $\bar{n}_d = R_d T$  for the bright and dark state, respectively. Assuming Poissonian statistics is justified for laser stray light and detector dark counts, but also for fluorescence photons as we detect only a small portion ( $\sim 1\%$ , see section 1.2.2) of the light scattered by the ion.

The above treatment assumes the  $D_{5/2}$  state as stable, i.e. the possibility of spontaneous decay to the  $S_{1/2}$  ground state, turning the ion bright, is neglected. This effect, however, becomes relevant if the integration time  $T$  is no longer short compared with the  $D_{5/2}$ -state lifetime  $\tau = 1.17$  s [122]. If at any time  $t < T$ , the ion returns to the ground state during the integration period, the expectation value for the number of detector counts for the dark state is modified to

$$\bar{n}'_d(t) = R_d t + R_b (T - t). \quad (2.3)$$

As the probability  $dp$  for a spontaneous decay during the interval  $[t, t + dt]$  is given by

$$dp = \frac{1}{\tau} e^{-t/\tau} dt, \quad (2.4)$$

we obtain the mean modified expectation value

$$\bar{n}'_d = \int_0^T [R_d t + R_b (T - t)] \frac{1}{\tau} e^{-t/\tau} dt + \int_T^\infty R_d T \frac{1}{\tau} e^{-t/\tau} dt \quad (2.5)$$

$$= R_b T - (R_b - R_d) \tau (1 - e^{-T/\tau}), \quad (2.6)$$

which is simply to be substituted for  $\bar{n}_d$  in eqn. 2.1.

The threshold  $n_{\text{th}}$  is now chosen such that the error probability  $\varepsilon$  is minimized. Typical experimental values are detection rates  $R_b = 155 \cdot 10^3 \text{ s}^{-1}$  and  $R_d = 100 \text{ s}^{-1}$  for the bright and dark state, respectively, and integration time  $T = 100 \mu\text{s}$ . For these parameters, fig. 2.4 shows an experimental histogram of the numbers of detection events for an ion being in the  $D_{5/2}$  state with 13.2(1)% probability. The distributions for the bright and dark state, respectively, are clearly separated. The optimal threshold is found to be  $n_{\text{th,opt}} = 2$  (by minimizing expression 2.1), i.e. the ion is identified as bright for more than 2 detection events and as dark otherwise, yielding the error probability  $\varepsilon = 1.3 \cdot 10^{-5}$ .

### Bayesian probability estimation

The previous paragraph explained how to experimentally project the atomic state onto the  $S_{1/2}$ - $D_{5/2}$  basis. For many experiments, however, one is interested in estimating the underlying probability  $p$  for the ion to be in the  $D_{5/2}$  state after the coherent manipulations. It is thus not sufficient to execute the experimental sequence once, but one has to repeat the experiment multiple times in order to gather statistical information. Our goal is to derive an estimate for the probability  $p$  after performing the experiment  $n$  times,  $k$  out of which the ion was projected onto  $D_{5/2}$  (the dark state).

A common way to estimate  $p$  is the approach of frequentist inference [135], i.e. the underlying probability is assigned the relative frequency  $p = \frac{k}{n}$  with the uncertainty  $\Delta p = \sqrt{\frac{p(1-p)}{n-1}}$ . However, this approach fails when it comes to probabilities close to 0 or 1. In particular, for  $k = 0$  ( $k = n$ ), we obtain  $p = 0$  ( $p = 1$ ) and  $\Delta p = 0$ . For a finite number  $n$  of

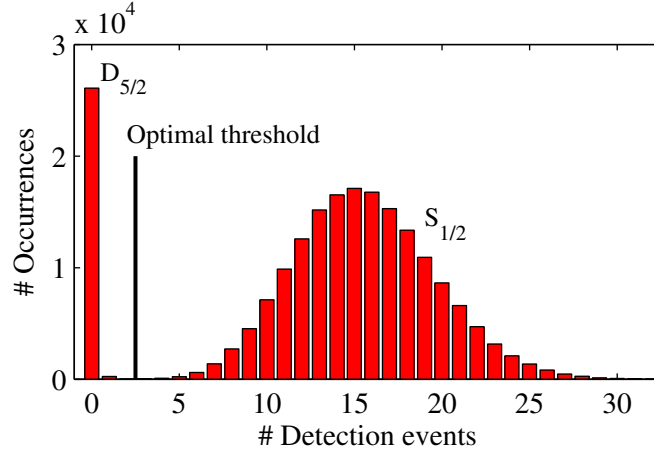


**Fig. 2.4:** Experimental histogram of the numbers of detection events for a  $D_{5/2}$ -state population of 13.2(1) % and a total of 199 000 trials. The underlying expectation values for the bright and dark state are  $\bar{n}_b = 15.5$  and  $\bar{n}_d = 0.01$ , respectively. The optimal threshold for discriminating between the two states is found to be  $n_{\text{th,opt}} = 2$ , which yields the error probability  $\varepsilon = 1.3 \cdot 10^{-5}$ .

trials, it is of course impossible to determine with certainty that the underlying probability  $p$  be 0 or 1.

The approach used by our group is the one of Bayesian inference [136], which is based on the notion of conditional probability. We ask for the probability distribution  $P(p)$  for the underlying probability  $p$  of finding the ion in the dark state. Before performing the first experimental cycle, we are completely ignorant of the probability  $p$ , which corresponds to a uniform distribution  $P(p) \equiv 1$  (the *prior*). With each experimental cycle, our knowledge of  $p$  is updated, and for more and more cycles we gain more and more information on  $p$ , i.e. the distribution  $P(p)$  becomes narrower.

The mathematical treatment starts off with the definition of conditional probability: the probability for an event A given event B is

$$P(A|B) := \frac{P(A \cap B)}{P(B)} \quad (2.7)$$

with the joint probability  $P(A \cap B)$  for events A and B and probability  $P(B)$  for event B. By formulating the analogous statement for  $P(B|A)$ , we eliminate  $P(A \cap B)$  and arrive at

$$P(A|B) = \frac{P(B|A) P(A)}{P(B)}. \quad (2.8)$$

Applied to our situation, the probability distribution  $P(p|k)$  for the underlying probability  $p$  given  $k$  projections onto the dark state becomes

$$P(p|k) = \frac{B(k|p) P(p)}{B(k)} \quad (2.9)$$

$$= \frac{B(k|p) P(p)}{\int_0^1 B(k|p) P(p) dp} \quad (2.10)$$

with the prior  $P(p) \equiv 1$ .  $B(k|p)$  denotes the binomial distribution for finding  $k$  projections onto the dark state for a given underlying probability  $p$ :

$$B(k|p) = \binom{n}{k} p^k (1-p)^{n-k} \quad (2.11)$$

Hence, we arrive at the explicit expression

$$P(p|k) = \frac{p^k (1-p)^{n-k}}{\int_0^1 p^k (1-p)^{n-k} dp} \quad (2.12)$$

$$= \frac{(n+1)!}{k!(n-k)!} p^k (1-p)^{n-k}. \quad (2.13)$$

This is a polynomial of order  $n$  and fully describes our knowledge of the probability  $p$ . We can now define our estimate for  $p$  after performing  $n$  trials as its expectation value with respect to  $P$ :

$$\langle p \rangle = \int_0^1 p P(p|k) dp \quad (2.14)$$

$$= \frac{k+1}{n+2} \quad (2.15)$$

Consequently, we define the uncertainty of our estimate as the standard deviation of  $P$ :

$$\Delta p = \sqrt{\langle p^2 \rangle - \langle p \rangle^2} \quad (2.16)$$

with

$$\langle p^2 \rangle = \int_0^1 p^2 P(p|k) dp \quad (2.17)$$

$$= \frac{(k+1)(k+2)}{(n+2)(n+3)} \quad (2.18)$$

From the equations above, it becomes apparent that even for  $k=0$  ( $k=n$ ), we find  $\langle p \rangle > 0$  ( $\langle p \rangle < 1$ ) with uncertainties  $\Delta p > 0$ , as expected for a finite number of trials (in contrast to frequentist inference).

Bayesian inference is the method chosen for estimating probabilities in all experiments presented in this thesis. Also, in most cases, we have chosen a default number of trials of  $n=500$ .

#### 2.1.4 Spectroscopy

The most basic type of coherent manipulation on the 729 nm transition is pulsed spectroscopy. We perform this routinely in order to characterize the static magnetic field applied to the ion as well as the frequency of the laser itself. For the work presented in this thesis, it was sufficient to calibrate these values once every morning, as they are sufficiently stable on a time scale of a few hours.

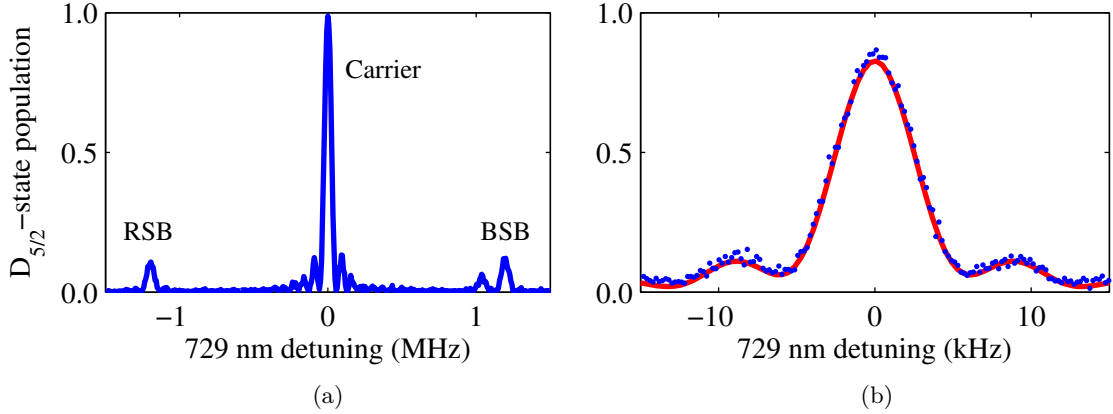


**Fig. 2.5:** Pulsed spectroscopy on the 729 nm qubit transition (light polarization chosen perpendicular to the quantization axis). (a) Overview spectrum of the  $|S_{1/2}, m = -1/2\rangle \leftrightarrow |D_{5/2}, m = -5/2\rangle$  transition for an excitation pulse of  $15 \mu\text{s}$  length at  $\sim 1 \text{ mW}$  optical power. Apart from the carrier transition, the first-order sidebands of the ion’s axial motion are visible (at  $1.20 \text{ MHz}$  from the carrier). (b) Precision spectroscopy on the carrier transition with an excitation pulse of  $150 \mu\text{s}$  length (corresponding to a Fourier-limited spectral width of  $1.1 \text{ kHz}$ ) at an optical power of  $\sim 1 \mu\text{W}$ . From the theoretical model fitted to the data ( $\chi^2 = 2.4$ ), we derive  $3.74(3) \text{ kHz}$  Rabi frequency and  $3.13(7) \text{ kHz}$  of incoherent contribution to the linewidth from magnetic-field fluctuations. The line center is determined to within  $26 \text{ Hz}$  accuracy.

Upon preparing the ion in the  $|S_{1/2}, m = -1/2\rangle$  ground state, we send a pulse of fixed length and variable frequency at  $729 \text{ nm}$  onto the ion. As we detune the laser frequency by means of an AOM and measure the  $D_{5/2}$  population, we obtain a spectrum of the qubit transition. Fig. 2.5(a) shows part of a typical overview scan of a carrier transition with its axial motional sidebands for a rather short and strong excitation pulse at  $729 \text{ nm}$ . This kind of pulse provides low spectral resolution, but is well suited for performing quick scans over a larger frequency span. For high-resolution spectroscopy, longer pulses of low intensity are used, as displayed in fig. 2.5(b). An excitation pulse of  $150 \mu\text{s}$  duration allows for a spectral resolution of  $1.1 \text{ kHz}$  (its Fourier width). This is below the width of the transition itself which is incoherently broadened by fluctuations of the static magnetic field<sup>5</sup>. The origins and a quantification of these will be described in detail in section 2.1.6. Nevertheless, the theoretical model fitted to the data allows us to determine the line center of the resonance with an uncertainty  $< 30 \text{ Hz}$ .

### 2.1.5 Rabi oscillations

Besides performing spectroscopy to determine the transition frequency between two particular Zeeman states of the  $S_{1/2}$  and  $D_{5/2}$  manifold, another essential type of coherent manipulation is to drive Rabi oscillations. The  $729 \text{ nm}$  laser is set on resonance with a

<sup>5</sup>Magnetic-field fluctuations were found to be the only relevant source of incoherent line broadening since the narrow linewidth of the qubit laser (see section 2.1.1) does not contribute significantly.

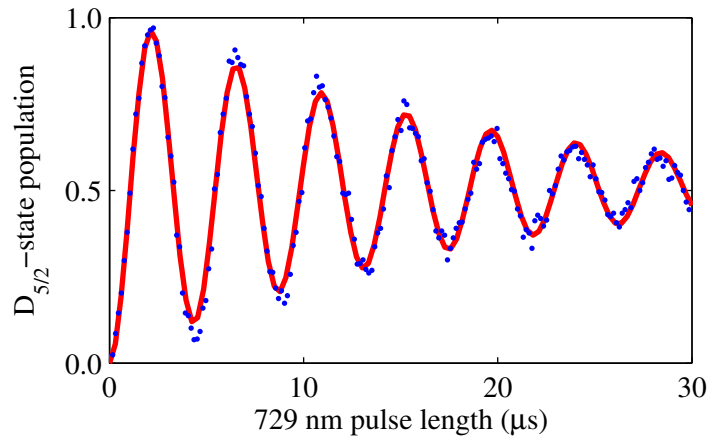


**Fig. 2.6:** Pulse-length scan on the  $|S_{1/2}, m = -1/2\rangle \leftrightarrow |D_{5/2}, m = -5/2\rangle$  carrier transition for 63.3 mW optical power (light polarization chosen perpendicular to the quantization axis). From the fit ( $\chi^2 = 2.5$ ), we obtain a Rabi frequency of 228.6(2) kHz.

(carrier) transition, and the length of the excitation pulse is successively increased. This pulse-length scan reveals the  $D_{5/2}$ -state population as a function of pulse length and allows us to determine the Rabi frequency on the transition with great accuracy. Fig. 2.6 shows such a pulse-length scan for an optical power of 63.3 mW, yielding a Rabi frequency of 228.6(2) kHz. For an isolated two-level scheme, we would expect entirely undamped oscillations (spontaneous decay from the  $D_{5/2}$  state is negligible on the relevant time scales). However, as described in app. A.2, the ion's finite temperature entangles its electronic with its motional state, which leaves the electronic state in a statistically mixed state after a sufficiently long period of excitation. On longer time scales, magnetic-field fluctuations cause additional decoherence of the electronic state and thus damping of the Rabi oscillations as well.

### 2.1.6 Characterization of magnetic-field noise

As noted in the two previous sections, the external magnetic field applied to the ion is not exactly static. Instead there is a number of sources for fluctuations of the magnetic-field strength on very different time scales, of which the three most relevant are:

- **White magnetic-field noise:** The electronics within many of our laboratory devices, in particular those with switched-mode power supplies, create magnetic fields in the 10 – 1000 kHz frequency range.
- **Power line:** The currents drawn by devices through cables create magnetic fields sinusoidally oscillating at 50 Hz frequency. Besides white magnetic-field noise, this is the major contribution of undesired field fluctuations.
- **Long-term drifts:** On the time scale of minutes to hours, changes in the amount of current drawn by our laboratory devices, but also by machines in the mechanical

workshop located beneath our laboratory, cause the magnitude of the magnetic field at the position of the ion to drift. Currently, this issue is resolved by performing atomic spectroscopy about once in ten minutes in order to determine the magnetic-field strength.

The magnetic-field fluctuations have a number of adverse effects, the most detrimental one being a significantly shortened coherence time of our atomic qubit. This arises from the magnetic field having slightly different magnitude from one experimental cycle to the next, changing the atomic resonance frequencies. This means that the “reference oscillator”, the 729 nm laser, is detuned from its resonance by a different amount in each cycle, which is equivalent to a loss in phase coherence between ion and laser – the qubit decoheres. It turns out that for our setup, magnetic-field fluctuations are by far the limiting factor for qubit coherence times.

One approach to strongly improve atomic coherence is the so-called *line-triggered* sequence mode; the experimental sequence is triggered by the slope of a 50 Hz signal derived from the power line. The sequence is thus “phase locked” to the power-line signal and the magnetic field from cables running close to the ion trap will cause a magnetic field of identical magnitude at each experimental cycle. Hence, the frequency detuning between atomic resonance and qubit laser is the same in each cycle and phase coherence between ion and laser is preserved. Although this technique has proven to enhance the qubit coherence time by roughly one order of magnitude, it is not well suited for most of the experiments described in this thesis; triggering the sequence by the power-line signal naturally restricts the experimental repetition rate to 50 Hz. However, as will be shown later, we require repetition rates of 1 – 10 kHz in order to gather sufficient statistics in a reasonable amount of measuring time.

As an alternative approach, we are developing an active magnetic-field compensation [137]. From a number of three-axis Hall sensors placed around the vacuum chambers, the magnetic field at the position of the ion is inferred. Compensation coils are then used for either feed-forward control to compensate fluctuations at 50 Hz (and higher harmonics) or for a closed feedback loop which should be able to eliminate fluctuations of up to 1 kHz frequency.

A third approach would be found in enclosing the vacuum chambers with mu-metal shielding. Considering their size, however, such a solution would be very costly and close to experimentally infeasible. Hence we are left only with the prospect of active magnetic-field stabilization.

### **Ramsey experiment**

A number of ways to determine qubit coherence times exist, one of the simplest being the observation of Rabi oscillations over a sufficiently long time scale. As the qubit state decoheres, the oscillations become damped, and the coherence time is determined as the characteristic time of this damping process. This method, however, cannot distinguish between damping caused by magnetic-field fluctuations and damping due to the finite ion temperature in the trap potential. In most of our experimental scenarios, the latter type

of damping occurs on a much shorter time scale than the former, hence this approach is not suited for estimating coherence times limited by magnetic-field noise.

A second, less direct approach is an adaptation of a method devised by Norman Ramsey [138]. A 729 nm laser pulse of pulse area<sup>6</sup>  $\frac{\pi}{2}$  creates a symmetric superposition of two atomic energy eigenstates. After a certain waiting period, the *Ramsey time*  $T$ , another  $\frac{\pi}{2}$  laser pulse with phase  $\phi$  (the *Ramsey phase*) relative to the first pulse is applied before projecting the atomic state onto the basis formed by the two energy eigenstates.

When starting off with the ion prepared in one of the  $S_{1/2}$  Zeeman states, the phase-dependent probability  $p(\phi)$  to project it onto the  $D_{5/2}$  Zeeman state during state detection is in general described by fringes of the form

$$p(\phi) = \frac{1}{2} (1 + V \cos(\phi)). \quad (2.19)$$

The fringe visibility  $V$  is a measure for the amount of coherence remaining between atomic qubit and laser after the Ramsey time  $T$ . Measuring this value for a number of Ramsey times then yields the time scale for decoherence caused by magnetic-field fluctuations. As the total pulse area applied to the ion amounts only to  $\pi$ , decoherence from entanglement of the electronic with the motional state is kept at a minimum. Even more importantly, this contribution to the total decoherence process is independent of the Ramsey time between the two laser pulses.

Fig. 2.7(a) shows Ramsey fringes for a Ramsey time  $T = 100 \mu\text{s}$ , from which we extract the visibility  $V = 0.968(3)$ . The slight phase shift of the fringes stems from a small detuning of  $\sim 0.1 \text{ kHz}$  between atomic resonance and laser. In order to estimate the qubit coherence time, the fringe visibility as a function of Ramsey time is measured (see fig. 2.7(b)). Before being able to draw meaningful conclusions from this data, we need to theoretically model the two major contributions to magnetic-field fluctuations, white noise and power-line fields. Empirically, we found that the white magnetic-field noise is well modeled by the Gaussian probability distribution

$$P_{\text{noise}}(B) = \frac{1}{B_{\text{noise}}} \sqrt{\frac{4 \ln 2}{\pi}} e^{-4 \ln 2 \left(\frac{B}{B_{\text{noise}}}\right)^2} \quad (2.20)$$

with the FWHM (full width at half maximum) value  $B_0$ . As derived in app. A.3, the 50 Hz field fluctuations from the power line are described by the modified arcsine distribution

$$P_{\text{line}}(B) = \frac{1}{\pi B_{\text{line}}} \frac{1}{\sqrt{1 - \left(\frac{B}{B_{\text{line}}}\right)^2}} \quad (2.21)$$

for a sinusoidally oscillating field<sup>7</sup>  $B(t) = B_{\text{line}} \sin(2\pi \cdot 50 \text{ Hz} \cdot t)$ . For both distributions, any static offset field has been set to zero without loss of generality. The joint probability distribution  $P_{\text{joint}}(B)$  for the two sources of field fluctuations is then given by the convolution of the individual distributions. As shown in app. A.4, the fringe visibility  $V(T)$  as

<sup>6</sup>The area of a pulse of Rabi frequency  $\Omega(t)$  is defined as  $A := \int \Omega(t) dt$ .

<sup>7</sup>Note that the 50 Hz oscillation frequency does not enter into the probability distribution  $P_{\text{line}}(B)$ .

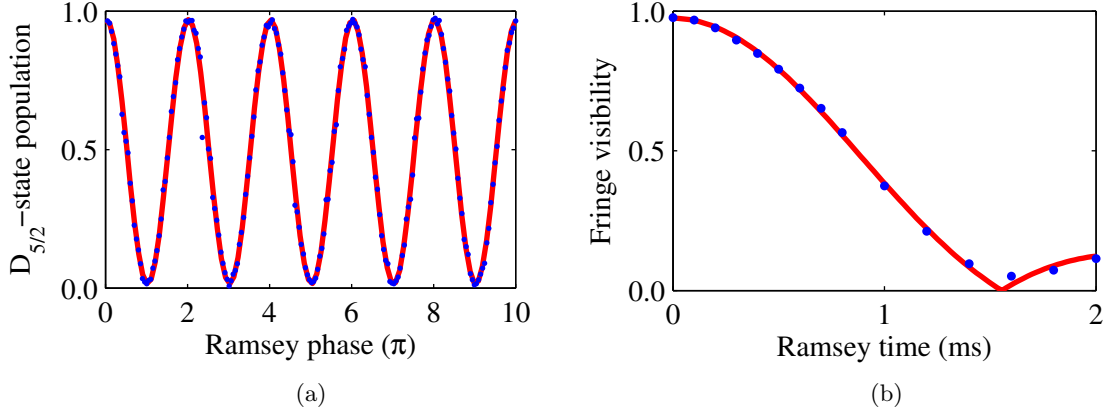


**Fig. 2.7:** (a) Ramsey experiment on the  $|S_{1/2}, m = -1/2\rangle \leftrightarrow |D_{5/2}, m = -1/2\rangle$  transition. The two  $\frac{\pi}{2}$  laser pulses have a length of  $0.885 \mu\text{s}$  each with a Ramsey time of  $100 \mu\text{s}$  between them. From the fit according to eqn. 2.19 ( $\chi^2 = 1.4$ ), we obtain the fringe visibility  $V = 0.968(3)$ . (b) Fringe visibility as a function of Ramsey time. Fitting the theoretical model from eqn. 2.23 ( $\chi^2 = 7.4$ ) yields the white-noise contribution  $B_{\text{noise}} = 0.183(8) \text{ mG}$  and the power-line contribution  $B_{\text{line}} = 0.440(4) \text{ mG}$ . Due to the thermal motion of the ion, the  $\frac{\pi}{2}$  pulses are not carried out with unity fidelity, resulting in a visibility  $V < 1$  even for very short Ramsey times. Error bars are smaller than the size of symbols.

a function of the Ramsey time  $T$  is the cosine transform of the probability distribution for the magnetic field,

$$V(T) = \int_{-\infty}^{\infty} P_{\text{joint}}(B) \cos\left(\frac{2\mu_B}{5\hbar} B \cdot T\right) dB, \quad (2.22)$$

which evaluates to

$$V(T) = \exp\left[-\left(\frac{1}{\sqrt{2}} \frac{2\mu_B}{5\hbar} B_{\text{noise}} \cdot T\right)^2\right] \cdot \left|J_0\left(\frac{2\mu_B}{5\hbar} B_{\text{line}} \cdot T\right)\right| \quad (2.23)$$

with the zeroth-order Bessel function of the first kind  $J_0$ . When applying this model to the data from fig. 2.7(b), we find the white-noise contribution  $B_{\text{noise}} = 0.183(8) \text{ mG}$  and the power-line contribution  $B_{\text{line}} = 0.440(4) \text{ mG}$ . This shows that the 50 Hz power line is the dominant source for magnetic-field fluctuations, but white noise from the laboratory electronics is not at all negligible.

For both white noise and power-line fields, we define the individual qubit coherence times  $T_{2,\text{noise}}^*$  and  $T_{2,\text{line}}^*$  as the points at which the visibilities drop to  $\frac{1}{e}$  and find

$$T_{2,\text{noise}}^* = 2.19(10) \text{ ms} \quad (2.24)$$

$$T_{2,\text{line}}^* = 1.13(1) \text{ ms}. \quad (2.25)$$

These are the figures of merit for the time scale on which coherent manipulations of the qubit state can be performed. It should be mentioned that these values for the coherence

times are specific to the  $|S_{1/2}, m = -1/2\rangle \leftrightarrow |D_{5/2}, m = -1/2\rangle$  transition; transitions between other Zeeman states show greater susceptibility to the magnetic field and thus shorter coherence times.

### Summary

In this section, I presented the implementation of an optical qubit in  $^{40}\text{Ca}^+$ , formed by the  $S_{1/2}$  ground state and  $D_{5/2}$  metastable state and controlled through a narrow-band laser at 729 nm. After establishing the basic tasks of spectroscopy and pulse-length scans necessary for calibrating the laser excitation, we investigated the qubit’s coherence properties. It turned out that fluctuations of the ambient magnetic field limit the coherence time to values on the order of 1 ms.

## 2.2 Coherent manipulations – radio-frequency qubit

The optical transition at 729 nm, coupling the  $S_{1/2}$  and  $D_{5/2}$  state, forms a qubit suitable for quantum-computational tasks. However, as detailed in the previous section, this particular choice for a qubit imposes a number of experimental challenges, such as the necessity for a very narrow-band and stable laser, a well-cooled ion and little fluctuations of the ambient magnetic field. When using Zeeman states in  $^{40}\text{Ca}^+$  for qubit states, an obvious alternative to an optical qubit is one formed by two Zeeman states of the same fine-structure manifold. A preferable choice is the  $S_{1/2}$  manifold, since it comprises only two Zeeman states and does not undergo spontaneous decay. For a typical value  $B_{\text{stat}} \approx 3$  G for the strength of the static magnetic field, the energetic splitting of the  $|\pm 1/2\rangle := |S_{1/2}, m = \pm 1/2\rangle$  states corresponds to a transition frequency of  $\omega_0 \approx 2\pi \cdot 8$  MHz, which lies in the high-frequency band of the radio spectrum. A qubit with a radio-frequency (RF) transition offers two particular advantages over optical qubits:

- **Reference oscillator:** A qubit is only as stable as its reference oscillator, i.e. long coherence times require a narrow-band and stable oscillator. For an optical qubit, setting up a laser with these properties is a rather involved task, whereas an RF qubit requires no more than a stable RF source. Such a source is provided by our sequence-control unit Hydra, which features direct digital synthesizers (DDSs) that are phase locked to our atomic clock. Each of these can be used as reference oscillator of narrow linewidth and great stability.
- **Thermal motion:** As explained in app. A.2, dynamics of the optical qubit through Rabi oscillations on the carrier transition are subject to decoherence as the ion’s electronic state is coupled to its motion. This coupling stems from the finite Lamb-Dicke parameter, i.e. the ion’s wave-packet size is not negligible compared with the wavelength of the laser light. At transition frequencies in the RF regime, the wavelengths are much larger and the ion “perceives” an almost perfectly homogeneous field. Hence the ion’s electronic state is no longer coupled to its motion, and even for hot ions, the qubit coherence is not affected by the ion’s motion.

The second point, however, may also be considered a disadvantage; as the ion’s electronic and motional state are not coupled, we cannot make use of the motion, e.g. as a quantum bus between ions. Also, given the RF wavelength, we cannot address ions in a string individually. However, there are research groups who make use of a gradient in their static magnetic field in order to circumvent both issues [37].

This section will start off with a theoretical model for the coherent control of the  $S_{1/2}$  RF qubit, before introducing the experimental implementation and concluding with the results characterizing our control over the RF qubit.

### 2.2.1 Magnetic-dipole transitions

In contrast to the electric dipole/quadrupole optical transitions introduced so far, the transition  $|+1/2\rangle \leftrightarrow |-1/2\rangle$  in the  $S_{1/2}$  manifold is a pure spin flip (the quantum number of orbital angular momentum is left unchanged), and hence a magnetic-dipole transition.

I will now show how magnetic-dipole transitions are driven through oscillating magnetic fields. In analogy to section 1.1.2, the system Hamiltonian for a two-level system with ground state  $|-1/2\rangle$  and excited state  $|+1/2\rangle$ , split by the energy  $\hbar\omega_0$ , is

$$H_{\text{sys}} = \frac{\hbar\omega_0}{2} (|+1/2\rangle \langle +1/2| - |-1/2\rangle \langle -1/2|). \quad (2.26)$$

The interaction Hamiltonian for a magnetic dipole  $\vec{\mu}$  in the presence of an external magnetic field  $\vec{B}$  is

$$H_{\text{int}} = -\vec{\mu} \cdot \vec{B}. \quad (2.27)$$

The magnetic-dipole operator, expressed in terms of the spin operator  $\vec{S}$ , is

$$\vec{\mu} = \gamma \vec{S} \quad (2.28)$$

with the gyromagnetic ratio  $\gamma = g\mu/\hbar$ , whereby for a single electron in the  $S_{1/2}$  state, the Landé factor<sup>8</sup> is  $g \approx 2$ , and the electron’s magneton is  $\mu = -\mu_B$ . The spin operator is expressed through the vector  $\vec{\sigma}$  of Pauli matrices via  $\vec{S} = \frac{\hbar}{2}\vec{\sigma}$ . Putting all this together, we find the interaction Hamiltonian

$$H_{\text{int}} = \mu_B \vec{\sigma} \cdot \vec{B}. \quad (2.29)$$

In order to efficiently couple the two energy eigenstates, the magnetic field needs to be polarized perpendicularly to the quantization axis. We hence choose  $\vec{B} = B_{\text{RF}} \cos(\omega_{\text{RF}} t) \vec{e}_x$ . With the Pauli matrix  $\sigma_x = |+1/2\rangle \langle -1/2| + |-1/2\rangle \langle +1/2|$  and the coupling strength (Rabi frequency)  $\Omega := \frac{1}{\hbar}\mu_B B_{\text{RF}}$ , we arrive at

$$H_{\text{int}} = \frac{\hbar\Omega}{2} (|+1/2\rangle \langle -1/2| + |-1/2\rangle \langle +1/2|) \left( e^{-i\omega_{\text{RF}} t} + e^{i\omega_{\text{RF}} t} \right). \quad (2.30)$$

This form is identical to eqn. 1.25 with the Lamb-Dicke parameter  $\eta = 0$ . Analogously, one can perform the transformation to the interaction picture, followed by the rotating-wave

---

<sup>8</sup>Precise value:  $g = 2.0023193$  [139]

approximation. When examined in closer detail, the latter is no longer exactly valid. As will be shown in 2.2.4, we achieve Rabi frequencies up to 100 kHz, which is not negligible compared with the transition frequency  $\omega_0 \approx 2\pi \cdot 8$  MHz. However, the resulting effects as e.g. the Bloch-Siegert shift [140] are still too small to play any significant role for our purposes. With the detuning parameter  $\Delta = \omega_{\text{RF}} - \omega_0$ , we obtain the final interaction Hamiltonian

$$H_{\text{int}}^I = \frac{\hbar\Omega}{2} \left( e^{-i\Delta t} |+\frac{1}{2}\rangle \langle -\frac{1}{2}| + e^{i\Delta t} |-\frac{1}{2}\rangle \langle +\frac{1}{2}| \right). \quad (2.31)$$

In conclusion, we can treat the  $S_{1/2}$  Zeeman qubit as a genuine two-level system with no motional sideband or other carrier transitions present.

### 2.2.2 Experimental implementation

The generation of an oscillating magnetic field at the ion's position can be achieved in various ways, e.g. by sending an oscillating current through one of the many electrodes present in an ion trap. For simplicity, however, we opted for ex-vacuo circuitry.

Both vacuum chambers are equipped with large viewports at the bottom sides. Below the Bright Trap viewport, we installed a two-loop copper-wire coil of 16 cm diameter and at 8 cm distance from the ion's position. Its inductance and an additional tunable capacitor form a series LC circuit. The capacitance is chosen as to shift the circuit resonance to the atomic transition frequency at  $\omega_0 \approx 2\pi \cdot 8$  MHz. The advantage of a resonant circuit lies in the enhancement of the current amplitude, which in turn enhances the strength of the magnetic field. The field itself points upwards and thus perpendicularly to the quantization axis. Hence we expect to efficiently couple the  $S_{1/2}$  Zeeman states and obtain the highest possible Rabi frequency. One of Hydra's DDSs provides the drive signal, which is sent through a 2 W amplifier<sup>9</sup> before entering the LC circuit.

Measurements characterizing the RF coil are presented in fig. 2.8. First, a network analysis is performed, determining the spectral response of the LC circuit. A commercial digital analyzer<sup>10</sup> is used to generate an RF signal at varying frequency that is sent to the LC circuit. The voltage induced in a small pick-up coil placed below the RF coil provides a measure for the amplitude of the oscillating magnetic field. In order not to feed the ion-trap drive at 26 MHz (which is picked up since the coils are close to the trap) into the network analyzer, we use a low-pass filter of 11 MHz cutoff frequency. We observe a steep resonance with a FWHM of 0.88 MHz at 8.35 MHz center frequency, indicating a significant enhancement of the RF current in the coil. Another peak is visible at 11.5 MHz, which is not yet fully understood, but can most likely be attributed to the massive steel vacuum chamber above the coil, constituting a resonance circuit in itself. The parametric excitation which is seen at twice the resonance frequency is already strongly suppressed by the low-pass filter.

In a second step, we determine the settling time of the LC circuit by feeding the signal from the pick-up coil into an oscilloscope. After switching on the DDS drive, the current in

<sup>9</sup>Mini-Circuit, ZHL-1-2W+

<sup>10</sup>Toptica, DigiLock 110

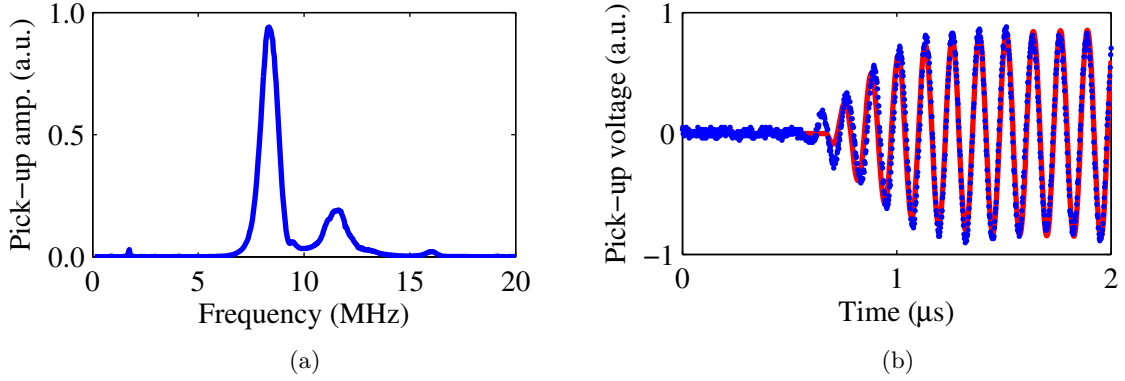


**Fig. 2.8:** Characterization of the RF coil. (a) Network analysis. Shown is the amplitude of the pick-up voltage as a function of the drive frequency, from which we estimate a resonance FWHM of 0.88 MHz at 8.35 MHz center frequency. (b) Build-up response after switching on the RF drive at 7.93 MHz. From the fit, we extract the settling time 0.24(1)  $\mu\text{s}$ .

the RF coil is built up with 0.24(1)  $\mu\text{s}$  settling time, which is compatible with the linewidth observed in the network analysis.

### Experimental sequence

Upon preparing the ion in the  $|{-1/2}\rangle$  state through optical pumping, the  $S_{1/2}$  Zeeman qubit is coherently manipulated through the RF coil. Afterwards, one usually wishes to measure the qubit in the  $\{|\pm 1/2\rangle\}$  basis. We do this by transferring (“shelving”) one of the two states, typically  $|+1/2\rangle$ , to the  $D_{5/2}$  manifold through a resonant pulse at 729 nm. State detection is performed in the usual way, as described in section 2.1.3, and hence the ion in the dark (bright) state after switching on the cooling lasers corresponds to a projection onto the  $|+1/2\rangle$  ( $|{-1/2}\rangle$ ) state.

### 2.2.3 Spectroscopy

The RF transition provides a direct means to determine the strength of the magnetic field at the ion’s position. In contrast, when using the 729 nm transition, spectroscopy of two individual lines is needed in order to account for the (initially) unknown frequency of the reference laser. Once the resonance frequency has been determined, high-fidelity qubit operations can be executed.

Spectroscopy on the RF transition is performed in analogy to the 729 nm transition; after preparing the ion in the  $|{-1/2}\rangle$  state, an RF pulse of fixed length and variable frequency is sent to the coil. We then measure the probability to project the ion onto the  $|+1/2\rangle$  state as a function of the RF detuning. Fig. 2.9 shows a spectrum for a pulse of 150  $\mu\text{s}$  duration, allowing for a Fourier-limited spectral resolution of 1.1 kHz. The line is centered at  $\omega_0 = 2\pi \cdot 7.927\,95(2)$  MHz, and via the relation  $\hbar\omega_0 = g_{\text{eff}} \mu_B B_{\text{stat}}$ , we find the magnitude  $B_{\text{stat}} = 2.828\,890(7)$  G of the static magnetic field during the measurement.

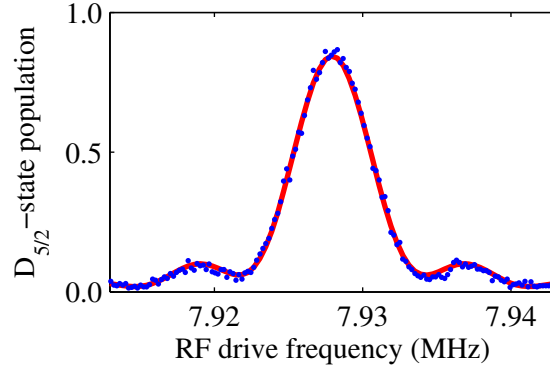


**Fig. 2.9:** Pulsed spectroscopy on the RF transition with an excitation pulse of  $150\ \mu\text{s}$  length (corresponding to a Fourier-limited spectral width of  $1.1\ \text{kHz}$ ) at an RF power of  $\sim 20\ \text{mW}$  sent to the coil. From the theoretical model fitted to the data ( $\chi^2 = 1.2$ ), we derive  $3.58(2)\ \text{kHz}$  Rabi frequency and  $3.21(5)\ \text{kHz}$  of incoherent contribution to the linewidth from magnetic-field fluctuations. The line center is determined to  $7.92795(2)\ \text{MHz}$ .

The incoherent contribution to the linewidth due to magnetic-field fluctuations is consistent with the value obtained from spectroscopy on one of the  $729\ \text{nm}$  transitions with a magnetic-field susceptibility similar to that for the RF transition ( $g_{\text{eff}} = 2.0023193$ ).

### 2.2.4 Rabi oscillations

After performing spectroscopy on the RF qubit, a pulse-length scan is needed to determine the Rabi frequency (for a given RF power) before any controlled coherent manipulations are carried out. The transition is driven resonantly, and the length of the excitation pulse is successively increased. Measuring the population of the  $|+1/2\rangle$  state as a function of the pulse length then allows us to determine the Rabi frequency on the RF transition with great accuracy. As shown in fig. 2.10, the pulse-length scan yields  $97.97(2)\ \text{kHz}$  Rabi frequency at  $\sim 900\ \text{mW}$  drive power. From the Rabi frequency, we reconstruct the amplitude  $B_{\text{RF}} = 70.00(1)\ \text{mG}$  of the oscillating magnetic field at the position of the ion. This, in turn, yields  $\sim 1.3\ \text{A}$  for the amplitude of the current in the RF coil, which is roughly in accordance with what we expect from the coil's properties.

In contrast to pulse-length scans on the  $729\ \text{nm}$  transition, the Rabi oscillations on the RF qubit are nearly completely undamped, as shown in fig. 2.10 for the first  $50\ \mu\text{s}$ . This proves that the ion's thermal motion ( $\langle n \rangle \approx 20$ ) has no impact on the RF transition owing to the very small Lamb-Dicke parameter. However, the transition is of course still susceptible to fluctuations of the static magnetic field. As will be shown in the next section, its coherence time is on the order of  $200\ \mu\text{s}$ , but the Rabi oscillations continue to much longer times. Extrapolation indicates that the oscillation visibility is expected to drop to  $\frac{1}{e}$  after  $24(1)\ \text{ms}$ . This can be understood by noting that the qubit's evolution in each experimental cycle is governed by the generalized Rabi frequency  $\Omega' = \sqrt{\Omega^2 + \Delta^2}$ , where  $\Delta$  is the RF-drive detuning from resonance and depends on the particular magnetic field during that cycle. Hence, the generalized Rabi frequency is slightly different in each cycle,

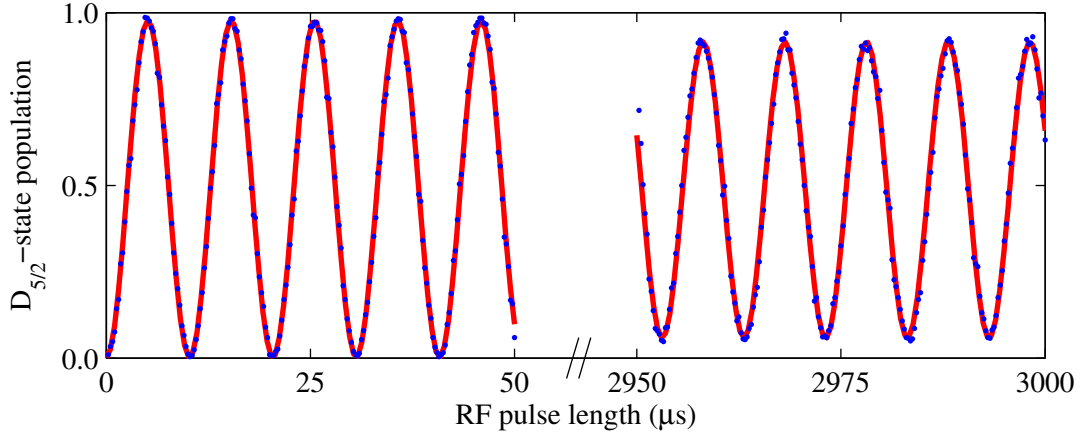


**Fig. 2.10:** Pulse-length scan on the RF transition for an RF power of  $\sim 900$  mW sent to the coil. From the fit ( $\chi^2 = 1.9$ ), we obtain a Rabi frequency of  $97.97(2)$  kHz and a damping-time constant of  $24(1)$  ms.

and for long excitation pulses, the Rabi oscillations lose their phase with respect to the beginning of the pulse. Averaging over many cycles thus leads to a loss of the oscillation visibility. For Rabi frequencies large compared with the average detuning, as in our case, the generalized Rabi frequency expands to  $\Omega' \approx \Omega + \frac{\Delta^2}{2\Omega}$  and depends only in second order on the detuning. The shift in the generalized Rabi frequency by the detuning is therefore suppressed by a factor  $\frac{\Delta}{2\Omega} \ll 1$ , which keeps the Rabi oscillations in phase for much longer than the transition coherence time.

In a larger context, this is a very simple realization of *dynamical decoupling* [141, 142], a family of experimental techniques employed to prolong qubit coherence times through rapid external control.

### 2.2.5 Ramsey experiment

Very much in analogy to section 2.1.6 that described a Ramsey experiment as a means to estimate the coherence time of the optical qubit, we conduct a similar experiment on the RF transition. Noise on the static magnetic field will change the energy of the  $S_{1/2}$  Zeeman states, causing the RF qubit to lose phase coherence with respect to its drive.

An RF pulse of pulse area  $\frac{\pi}{2}$  creates a symmetric superposition of two Zeeman states. After a certain waiting period, the Ramsey time, another  $\frac{\pi}{2}$  pulse with variable phase (the Ramsey phase) relative to the first pulse is applied before projecting the qubit onto the  $\{|\pm 1/2\rangle\}$  basis. The probability for a projection onto the  $|-1/2\rangle$  state as a function of the Ramsey phase is then expected to oscillate sinusoidally. From the decay of the visibility of these fringes for ever longer Ramsey times, we extract the qubit coherence time. Fig. 2.11 depicts one particular Ramsey fringe as well as the fringe visibility for different Ramsey times. From the latter, we obtain the coherence times  $T_{2,\text{noise}}^* = 211(16)$   $\mu\text{s}$  and  $T_{2,\text{line}}^* = 196(11)$   $\mu\text{s}$  for the white-noise and power-line contribution. This is in accordance with the values for the  $|S_{1/2}, m = -1/2\rangle \leftrightarrow |D_{5/2}, m = -1/2\rangle$  transition from section 2.1.6,

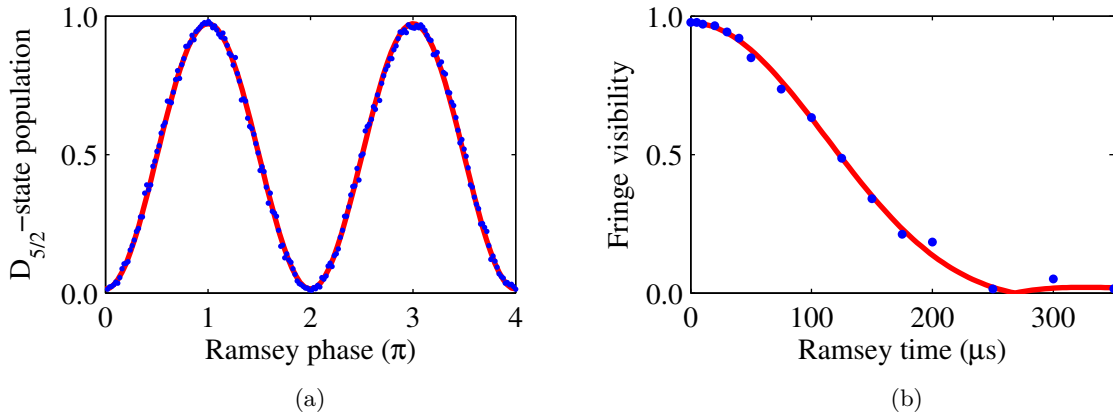


**Fig. 2.11:** (a) Ramsey experiment on the RF transition. The two  $\frac{\pi}{2}$  pulses have a length of  $2.811 \mu\text{s}$  each with a Ramsey time of  $10 \mu\text{s}$  between them. From the fit ( $\chi^2 = 0.95$ ), we obtain the fringe visibility  $V = 0.971(2)$ . (b) Fringe visibility as a function of Ramsey time. Fitting the theoretical model from eqn. 2.23 ( $\chi^2 = 36.7$ ) yields the white-noise contribution  $B_{\text{noise}} = 0.381(29) \text{ mG}$ , the power-line contribution  $B_{\text{line}} = 0.510(29) \text{ mG}$  and the qubit coherence times  $T_{2,\text{noise}}^* = 211(16) \mu\text{s}$  and  $T_{2,\text{line}}^* = 196(11) \mu\text{s}$ . Error bars are smaller than the size of symbols.

which are significantly longer as this transition is much less susceptible to magnetic-field fluctuations.

## Summary

In this section, I presented the implementation of a radio-frequency qubit, formed by the two  $S_{1/2}$  Zeeman states, as an alternative to the optical qubit. An ex-vacuo copper-wire coil facilitates simple and coherent control over this qubit, offering two particular advantages: insensitivity of qubit manipulations to the ion's thermal motion and the use of an easy-to-handle direct digital synthesizer (DDS) as a reference oscillator in place of the complex setup of a laser locked to a high-finesse optical cavity. Pulse-length scans showed Rabi frequencies as high as  $100 \text{ kHz}$ , comparable to those from the optical qubit.

## 2.3 Optical ground-state pumping

In the first two sections of this chapter, methods to coherently control the atomic qubit through optical and radio-frequency excitations were presented. A prerequisite for most of these operations is the ability to initialize the qubit in a pure quantum state prior to any coherent manipulations. In contrast, at the end of the experimental sequence (see fig. 2.3), the  $397 \text{ nm}$  cooling laser is switched off, leaving the ion in a statistical mixture of the  $|S_{1/2}, m = \pm 1/2\rangle$  Zeeman ground states. I will now discuss two schemes of preparing the ion in a particular one of the two states through optical pumping.

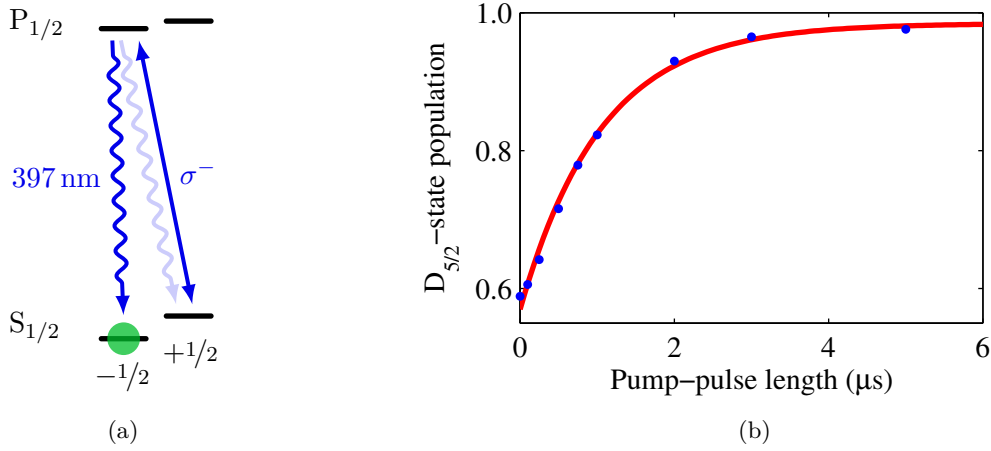


**Fig. 2.12:** (a) Level scheme for ground-state pumping on the  $S_{1/2}$ - $P_{1/2}$  transition. A laser at 866 nm repumps population from the  $D_{3/2}$  manifold (not shown). (b) Population of the  $D_{5/2}$  manifold after shelving the state  $|S_{1/2}, m = -1/2\rangle$  for various durations of the pump pulse. The exponential fit ( $\chi^2 = 9.3$ ) yields  $1.05(8) \mu\text{s}$  for the  $\frac{1}{e}$  time constant. Error bars are smaller than the size of symbols.

### 2.3.1 Pumping at 397 nm

For our purposes, we choose to initialize the atomic qubit in the  $|S_{1/2}, m = -1/2\rangle$  Zeeman state. The simplest way to achieve this is to drive the  $\sigma^-$  transition at 397 nm wavelength (see fig. 2.12(a)). This excites any unwanted population in  $|S_{1/2}, m = +1/2\rangle$  to  $|P_{1/2}, m = -1/2\rangle$  from where, in each excitation cycle, it decays with a fraction of  $\frac{1}{3}$  (given by the Clebsch-Gordan coefficients specific to this transition) to the desired  $|S_{1/2}, m = -1/2\rangle$  state.

As shown in fig. 2.2, we implement this scheme through a 397 nm beam with right-handed circular polarization<sup>11</sup> propagating antiparallel to the quantization axis (defined by the static magnetic field). A laser at 866 nm repumps any population decaying to the  $D_{3/2}$  manifold. Since the pump polarization is never perfectly circular, the  $|S_{1/2}, m = -1/2\rangle$  state will always be residually excited and thus never contain the entire population. This effect becomes more dramatic if the laser power is increased beyond saturation of the  $\sigma^-$  transition; since the  $\sigma^+$  transition is by far not saturated yet, more power will lead to a higher depopulation rate of the desired  $|S_{1/2}, m = -1/2\rangle$  state, while the pumping rate from  $|S_{1/2}, m = +1/2\rangle$  hardly increases any longer. As a compromise between pump efficiency and pump rate, we choose  $4 \mu\text{W}$  of optical power. At a spot diameter of  $\sim 60 \mu\text{m}$ , this corresponds roughly to the saturation power of the transition.

In order to determine the rate at which population is pumped to the  $|S_{1/2}, m = -1/2\rangle$  state, we measure its population as a function of pump duration (see fig. 2.12(b)). At the end of the pumping process, the population is shelved to the  $D_{5/2}$  manifold via the 729 nm

<sup>11</sup>Within this thesis, circular polarization is defined as the sense of rotation of the electric field when viewing the field along the quantization axis (defined by the static magnetic field).

transition. From an exponential fit, we derive the  $\frac{1}{e}$  time constant as  $1.05(8) \mu\text{s}$ . We thus consider it sufficient to choose  $5 \mu\text{s}$  pump duration. Note that the values for the population in fig. 2.12(b) are lower than the actual population in  $|S_{1/2}, m = -1/2\rangle$  since the shelving pulse is not perfect. The latter is accounted for by performing a second measurement during which the  $|S_{1/2}, m = +1/2\rangle$  is shelved for reference. For  $5 \mu\text{s}$  pump duration, we thus infer  $99.88(1)\%$  pump efficiency (and  $99.07(3)\%$  shelving efficiency).

### 2.3.2 Pumping at 729 nm

Due to its speed and simplicity, pumping at  $397 \text{ nm}$  is the method of choice for optical ground-state pumping for many experimental situations. As explained above, the circularly polarized pump beam needs to propagate along the quantization axis. For some experiments described in this thesis, the latter is oriented along the direction of fluorescence collection through one or both HALOs. This, however, means that the pump beam needs to be overlapped with the spatial mode of the weak atomic photon emission. For this arrangement, it has turned out that it is almost unavoidable to couple a significant amount of stray light from the pump beam into the optical fibers leading to the PMTs, yielding background rates as high as  $100 \cdot 10^3 \text{ s}^{-1}$  (not to mention the danger of permanently damaging the PMTs).

We have thus devised another scheme of optical ground-state pumping; the idea is to depopulate the  $|S_{1/2}, m = +1/2\rangle$  state in a frequency-selective instead of a polarization-selective way. As shown in fig. 2.13(a), we realize this by continuous excitation on the  $|S_{1/2}, m = +1/2\rangle \leftrightarrow |D_{5/2}, m = -3/2\rangle$  transition at  $729 \text{ nm}$ . Repumping is attained through a linearly polarized beam at  $854 \text{ nm}$  (and  $866 \text{ nm}$ , not shown), driving the transition  $|D_{5/2}, m = -3/2\rangle \leftrightarrow |P_{3/2}, m = -1/2\rangle$ . Population in the state  $|P_{3/2}, m = -1/2\rangle$  decays to the desired ground-state  $|S_{1/2}, m = -1/2\rangle$  with a fraction of  $\frac{2}{3}$ . Similarly to pumping at  $397 \text{ nm}$ , the final  $|S_{1/2}, m = -1/2\rangle$  population is limited by residual excitation, now stemming from off-resonant excitation at  $729 \text{ nm}$ . However, it has proven advisable to maximize the power of the  $729 \text{ nm}$  beam ( $63 \text{ mW}$  at  $\sim 80 \mu\text{m}$  spot diameter) in order to obtain an acceptable pump rate. Repumping from the  $D_{5/2}$  state at  $854 \text{ nm}$  artificially broadens the  $729 \text{ nm}$  transition, and the  $854 \text{ nm}$  power ( $4 \mu\text{W}$  at  $\sim 130 \mu\text{m}$ ) is chosen such as to maximize the rate of photons scattered on the  $S_{1/2}$ - $P_{3/2}$  transition and hence the pump rate. At the end of the pump sequence, the  $729 \text{ nm}$  beam is switched off and the  $854 \text{ nm}$  beam is set to saturate its transition for  $2 \mu\text{s}$  in order to quench any population in  $D_{5/2}$ .

Just as we did for pumping at  $397 \text{ nm}$ , we determine the rate at which population is transferred to the  $|S_{1/2}, m = -1/2\rangle$  state by measuring its population as a function of the pump-sequence duration via shelving to the  $D_{5/2}$  manifold. From the data shown in fig. 2.13(b), we infer  $4.2(4) \mu\text{s}$  for the  $\frac{1}{e}$  time constant. In order to account for the non-perfect shelving pulse, we perform a reference measurement during which the  $|S_{1/2}, m = +1/2\rangle$  state is shelved instead. For  $20 \mu\text{s}$  pump duration, we obtain  $99.58(2)\%$  pump efficiency.

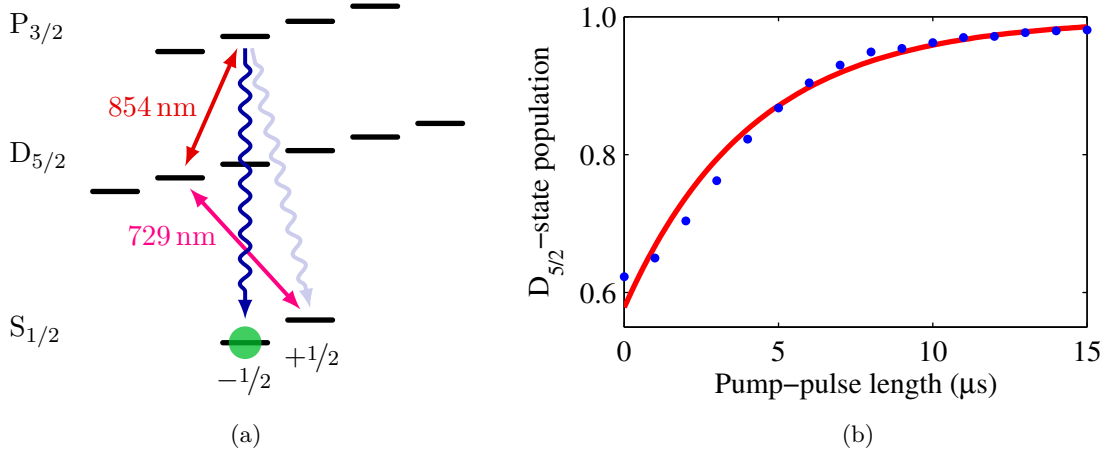


**Fig. 2.13:** (a) Level scheme for ground-state pumping on the  $S_{1/2}$ - $D_{5/2}$  transition. (b) Population of the  $D_{5/2}$  manifold after shelving the state  $|S_{1/2}, m = -1/2\rangle$  for various durations of the pump sequence. The exponential fit ( $\chi^2 = 26.0$ ) yields  $4.2(4) \mu\text{s}$  for the  $\frac{1}{e}$  time constant. Error bars are smaller than the size of symbols.

## 2.4 Auxiliary spectroscopy

As explained in section 1.2.3, all lasers except the qubit laser at 729 nm are stabilized to optical transfer cavities. Barometric changes, however, cause slow drifts of the cavity resonances on a day-to-day basis. Hence, it is necessary to calibrate the laser frequencies every morning by performing spectroscopy on the atomic transitions.

### 2.4.1 866 nm spectroscopy

The lasers at 866 nm and 397 nm are frequency-calibrated simultaneously by performing spectroscopy on the  $D_{3/2}$ - $P_{1/2}$  transition [143, 127]. In contrast to the experimental schemes presented so far in this thesis, this measurement is not conducted in pulsed mode but in a steady-state situation; for a given set of 397 and 866 nm laser parameters (Rabi frequencies, detunings from resonance, etc.), atomic fluorescence is detected and integrated for a fixed amount of time (typically 200 ms). The number of detected fluorescence photons is proportional to the steady-state population of the  $P_{1/2}$  state, and scanning either the 397 or 866 nm laser frequency yields an excitation spectrum from which we obtain all relevant laser parameters. Since the  $S_{1/2}$ - $P_{1/2}$  transition is used for Doppler cooling, it is advisable to choose the  $D_{3/2}$ - $P_{1/2}$  transition for spectroscopy.

A typical 866 nm spectrum is shown in fig. 2.14. Both the 397 and 866 nm laser are polarized perpendicularly to the quantization axis. From comparing the data and the theoretical model, we extract the two Rabi frequencies and calibrate the laser frequencies. As an alternative to 729 nm spectroscopy, it also yields an estimate for the strength of the static magnetic field.

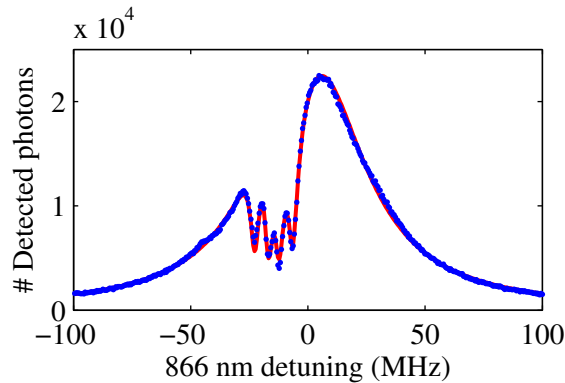


**Fig. 2.14:** Excitation spectroscopy on the  $D_{3/2}$ - $P_{1/2}$  transition at 866 nm for 200 ms integration of atomic fluorescence. The fit ( $\chi^2 = 7.8$ ), based on an 8-level Bloch-equation model [143, 127], allows us to calibrate the frequency axis (resonance at +1.1 MHz) and determine the 397 nm detuning from resonance (-15.8 MHz). Additionally, we find 6.1 MHz (13.5 MHz) Rabi frequency on the 866 nm (397 nm) transition and 2.6 G for the strength of the static magnetic field. The four distinctive dips are *dark resonances*, induced by coherent interaction of the two laser fields with the ion, forming an atomic steady state which couples only weakly to the light fields.

### 2.4.2 854 nm spectroscopy

Finally, the only remaining laser that needs frequency calibration prior to any advanced experiments is the one at 854 nm for addressing the  $D_{5/2}$ - $P_{3/2}$  transition. Like for all spectroscopy experiments except at 866 nm, we use a pulsed excitation scheme. First, the ion is prepared in the state  $|D_{5/2}, m = -5/2\rangle$  through a resonant pulse on the 729 nm transition. Then, with all other lasers off, a long and weak pulse (such as not to saturate and thus broaden the transition) at 854 nm, polarized perpendicularly to the quantization axis, is sent onto the ion. This removes population from  $D_{5/2}$  by repumping it back to the  $S_{1/2}$  ground state via the state  $|P_{3/2}, m = -3/2\rangle$  (see fig. 2.15(a)). Through the relation

$$p(\Delta) = p_0 e^{-R(\Delta) \cdot T} \quad (2.32)$$

for the remaining  $D_{5/2}$  population  $p$  (with initial population  $p_0$  and pulse duration  $T$ ), we obtain a spectrum of the detuning-dependent repumping rate  $R$  as shown in fig. 2.15(b). This, in turn, allows us to determine the resonance frequency of the  $|D_{5/2}, m = -5/2\rangle \leftrightarrow |P_{3/2}, m = -3/2\rangle$  transition and hence to calibrate the laser frequency. Besides, this kind of spectroscopy has turned out to yield the most accurate value for the Rabi frequency on the 854 nm transition.

## 2.5 Ion-temperature measurement

For all our experimental purposes so far, Doppler cooling on the  $S_{1/2}$ - $P_{1/2}$  transition has proven to cool the ion to a sufficiently low motional state, making advanced techniques like resolved-sideband cooling unnecessary. The latter, in particular, is a comparatively slow

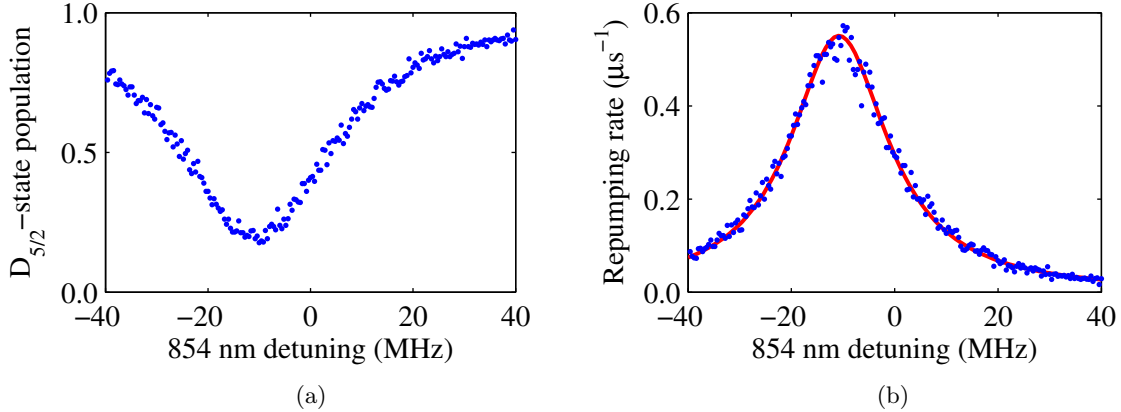


**Fig. 2.15:** Spectroscopy on the  $|D_{5/2}, m = -5/2\rangle \leftrightarrow |P_{3/2}, m = -3/2\rangle$  transition at 854 nm for a laser beam of  $1 \mu\text{W}$  optical power, focused to a spot of diameter  $\sim 250 \mu\text{m}$ , and polarized perpendicularly to the quantization axis. (a) Population remaining in the state  $|D_{5/2}, m = -5/2\rangle$  after a  $3 \mu\text{s}$  repumping pulse. (b) Repumping rate, from which we calibrate the frequency axis (resonance at  $-10.78(7)$  MHz) and extract  $1.469(4)$  MHz Rabi frequency ( $\chi^2 = 7.6$ ). The shape of the curve reflects the natural linewidth of  $\sim 23$  MHz of the 854 nm transition.

process, and is not suited for experimental schemes which require high sequence repetition rates.

Optimization of the cooling-laser parameters for a low ion temperature is described in detail in [94]. This section is meant to elaborate on our method of ion-temperature measurement, which, like other schemes, is based on measuring the strength of motional sidebands of the qubit transition at 729 nm. For a motional mode close to its ground state, most schemes compare the strength of the red and blue motional sideband, as their ratio directly yields the mean motional quantum number  $\langle n \rangle$  [48]. For higher motional states, however, those sidebands become more and more equal in strength, making it hard to obtain the temperature of this mode with sufficient accuracy. A much more robust method is to compare the strength of a sideband transition with that of the carrier transition instead.

### Carrier and sideband probing

As derived in section A.2 for a trapped particle in a one-dimensional harmonic potential, exciting (probing) one of the 729 nm carrier transitions with a pulse of length  $t$  will populate the  $D_{5/2}$  state with probability

$$p_{\text{car}}(t) = \frac{1}{2} \left( 1 - \sum_{n=0}^{\infty} p_n \cos(\Omega_{n,n} t) \right) \quad (2.33)$$

with Rabi frequencies  $\Omega_{n,n} = \Omega c_{n,n}$ , coupling-strength coefficients

$$c_{n,n} = \left| \langle n | e^{i\eta(a+a^\dagger)} | n \rangle \right| \quad (2.34)$$

$$= e^{-\eta^2/2} L_n^0(\eta^2), \quad (2.35)$$

associated Laguerre polynomials  $L$  and the thermal distribution  $p_n = \frac{\langle n \rangle^n}{(\langle n \rangle + 1)^{n+1}}$ . For known electronic Rabi frequency  $\Omega$  and Lamb-Dicke parameter  $\eta$ , one could derive the mean motional quantum number  $\langle n \rangle$  and hence the temperature directly from a fit to the damped Rabi oscillations described by eqn. 2.33. However, two major complications to this approach arise: first, the electronic Rabi frequency is typically not known with sufficient accuracy. Second, in a realistic situation in which the ion possesses not one but three motional modes (with in general different mean motional quantum numbers), all three contribute to damping the Rabi oscillations, and the individual contributions become hard to discern.

The solution to both issues lies in probing both a carrier and red-sideband transition (the following calculations are straightforward to modify for the blue sideband). For the red sideband, the  $D_{5/2}$  excitation probability becomes

$$p_{\text{rsb}}(t) = \frac{1}{2} \left( 1 - \sum_{n=1}^{\infty} p_n \cos(\Omega_{n,n-1} t) \right) \quad (2.36)$$

with Rabi frequencies  $\Omega_{n,n-1} = \Omega c_{n,n-1}$  and coupling-strength coefficients

$$c_{n,n-1} = \left| \langle n-1 | e^{i\eta(a+a^\dagger)} | n \rangle \right| \quad (2.37)$$

$$= \eta \frac{e^{-\eta^2/2}}{\sqrt{n}} L_{n-1}^1(\eta^2). \quad (2.38)$$

We now expand the functions describing the Rabi oscillations on the carrier and red-sideband transition, respectively, such that the ratio of the two becomes independent of the electronic Rabi frequency and the motional modes that we are not interested in (“spectator modes”). This expansion is justified for small pulse areas, i.e.  $\Omega_{n,n} t \ll 1$  for all  $n$  (since Rabi frequencies on sideband transitions are typically much weaker than on carrier transitions, this conditions implies  $\Omega_{n,n-1} t \ll 1$  as well). We then find for the excitation probability on the carrier transition

$$p_{\text{car}}(t) \approx \frac{1}{2} \left( 1 - \sum_{n=0}^{\infty} p_n \left( 1 - \frac{1}{2} (\Omega_{n,n} t)^2 \right) \right) \quad (2.39)$$

$$= \left( \frac{1}{2} \Omega t \right)^2 \sum_{n=0}^{\infty} p_n c_{n,n}^2 \quad (2.40)$$

and analogously for the red-sideband transition. It is important to note that the influence of the spectator modes on the Rabi frequencies is the same for the carrier ( $\Omega_{n,n}$ ) and

sideband transition ( $\Omega_{n,n-1}$ ). Hence the ratio  $p_{\text{rsb}}/p_{\text{car}}$  will not only be independent of the electronic Rabi frequency but of the quantum state of the spectator modes as well:

$$\frac{p_{\text{rsb}}}{p_{\text{car}}} = \frac{\sum_{n=1}^{\infty} p_n c_{n,n-1}^2}{\sum_{n=0}^{\infty} p_n c_{n,n}^2} \quad (2.41)$$

$$= \frac{\langle c_{n,n-1}^2 \rangle}{\langle c_{n,n}^2 \rangle}. \quad (2.42)$$

For a given Lamb-Dicke parameter  $\eta$ , the coupling-strength coefficients are readily calculated. The value  $\langle n \rangle$  of the mean motional quantum number is then found numerically from the measured ratio  $p_{\text{rsb}}/p_{\text{car}}$ . From the relation  $\frac{1}{2}k_{\text{B}}T = \langle E_{\text{kin}} \rangle = \frac{1}{2} \langle E \rangle$  between temperature  $T$ , kinetic energy  $E_{\text{kin}}$  and total energy  $E$ , we find the temperature of the motional mode in question:

$$T = \frac{\hbar\omega_{\text{T}}}{k_{\text{B}}} \langle n \rangle \quad (2.43)$$

## Experimental results

For probing the 729 nm transition, we choose the particular transition  $|S_{1/2}, m = -1/2\rangle \leftrightarrow |D_{5/2}, m = -5/2\rangle$ , since it lies at the very edge of the transitions between all the  $S_{1/2}$  and  $D_{5/2}$  Zeeman states, minimizing off-resonant excitations of unwanted transitions. We set the 729 nm laser power such that we attain a pulse area of  $\Omega_{n,n}t \approx 0.2\pi$  on the carrier transition for a 2  $\mu\text{s}$  probe pulse<sup>12</sup>. In order to obtain sufficient statistical data, we probe both the carrier and red-sideband transition  $10^5$  times and record the number of successful excitations of the  $D_{5/2}$  state.

For the axial mode of motion under standard Doppler-cooling conditions, we obtain 9.83(9) % and 0.76(3) % excitation probability on the carrier and red-sideband transition, respectively. From this, we derive the expectation value for the motional quantum number  $\langle n \rangle = 19.9(8)$  and the temperature  $T = 1.15(4)$  mK.

## Summary

In this chapter, I presented the experimental methods and tools required for controlling and manipulating the quantum state of  $^{40}\text{Ca}^+$ . In the first part, we established control over the optical qubit formed by the  $S_{1/2}$  ground state and the  $D_{5/2}$  metastable state by means of a narrow-band laser. We routinely perform spectroscopy and pulse-length scans in order to calibrate laser frequency and power. As such, we attain spectral resolutions on the order of 10 Hz and Rabi frequencies in the 100 kHz range. We also investigated the qubit's coherence time, which is on the order of 1 ms. As an alternative to this optical qubit, we make use of the two  $S_{1/2}$  Zeeman states in order to realize a radio-frequency qubit, which is not coupled to the ion's motion. We control the qubit by means of a copper-wire coil attached to the vacuum chamber and reach coupling strengths comparable to those

<sup>12</sup>For this pulse area, the approximation from eqn. 2.39 introduces a relative error  $< 1\%$ .

on the optical qubit. In order to prepare the atomic state for coherent manipulations, we implemented two complementary optical-pumping techniques. Among others, this task requires well-calibrated lasers for addressing the ion's electric-dipole transitions. To this end, I introduced spectroscopic techniques used routinely for laser calibration. Finally, I presented a robust method for determining the ion's temperature in the trap potential ( $\sim 1$  mK).

## Chapter 3

# Toward quantum networking

One of the essential ingredients to atom-based quantum networks [21, 61, 68, 144] is the ability to generate on-demand single photons that can be transmitted over distance [145, 146, 147, 148, 149, 88]. Acting as flying qubits, they allow distributing quantum information among spatially separated network nodes, mapping quantum information [150] or establishing entanglement between nodes [62, 64].

Various schemes and protocols exist that facilitate these purposes. One of them is based on the interference of two single photons that have each been entangled with a single atom. A projective measurement of the two-photon state then heralds entanglement between the atoms [64, 65, 66]. Another approach to creating entanglement between network nodes is to entangle an atom with a photon, then send the latter to another, remote atom by which it is absorbed [68]. To make these schemes feasible, a high rate of generated and collected photons in a well-defined quantum state is required.

In this chapter, I will first present both the theory and the experimental implementation of the controlled generation of single photons from a single ion. We are able to tune the temporal and spectral properties of the light emitted by the ion and quantify its single-photon character. As a prerequisite for the experiments presented in chapter 4, we show that the atomic coherence properties are faithfully transferred from the ion onto a photon.

### 3.1 Generation of single photons

Several methods for the generation of single photons from an atom or ion have proven practical in the past; one relies on Rayleigh scattering in an (effective) atomic two-level system, illustrated in fig. 3.1(a). Upon preparing such a system in the ground state  $|g\rangle$ , a laser pulse resonantly excites the typically short-lived upper state  $|e\rangle$  from which the atom spontaneously returns to the ground state, thereby emitting, i.e. scattering, a single photon [151, 152]. This scheme has two drawbacks: first, the exciting pulse is required to be much shorter than the excited-state lifetime, otherwise a non-negligible probability to scatter more than one photon arises. Second, the photon's spectral and temporal shape are determined solely by atomic properties, in particular the excited-state lifetime. We

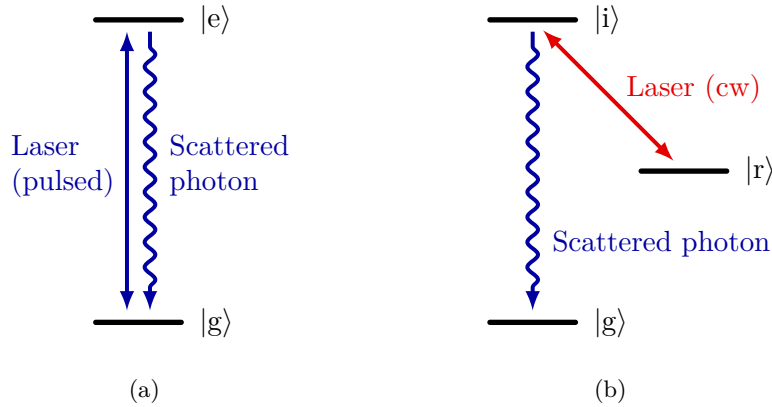


**Fig. 3.1:** Schemes for the generation of single photons from a single atom/ion. (a) Rayleigh scattering in a two-level system. (b) Raman scattering in a three-level system.

employ a more favorable scheme, the one of *spontaneous Raman scattering*, which we describe in the next section.

### 3.1.1 Spontaneous Raman scattering

In contrast to Rayleigh scattering, the process of Raman scattering refers to the effect that the initial atomic state differs from that after the scattering process. The effect is based on absorbing a photon from the light field on a certain transition and subsequently emitting a photon on a different transition. Hence Raman scattering can only be observed in multi-level systems. The Raman process is called *vacuum-stimulated* or *spontaneous* if, as in our case, the scattered photon is emitted into free space (as opposed to emission into another light field, which would be *stimulated* Raman scattering).

Fig. 3.1(b) shows the process of Raman scattering; after preparing the atom in the (meta)stable state  $|r\rangle$ , a laser couples the state to the intermediate, short-lived state  $|i\rangle$  which has, in general, decay channels to both  $|r\rangle$  and the ground state  $|g\rangle$ . Continuously exciting the transition  $|r\rangle \leftrightarrow |i\rangle$  will hence transfer all population to the ground state, scattering a single Raman photon at a frequency different from that of the driving laser field. The rate at which population is transferred from  $|r\rangle$  to  $|g\rangle$  is not only a function of the atomic properties but of the laser parameters as well. For example, if the laser excites the atom very weakly, i.e. the Rabi frequency is small compared with the natural transition linewidth, the population is transferred to the ground state on a time scale much longer than the natural lifetime of the intermediate state  $|i\rangle$ . Hence also the temporal shape (wave packet) of the scattered Raman photon is much longer than the natural lifetime. This is in contrast to the excitation of a two-level system by a short laser pulse, which yields Rayleigh-scattered photons of exponential temporal shape with the  $\frac{1}{\epsilon}$  time given by the excited-state lifetime. This tunability of the Raman process will be treated in more detail in the next paragraph.

### Raman-scattering tunability

In order to describe the properties of a Raman-scattered photon, we need to analyze the atomic dynamics first. A simple rate-equation model was found sufficient for most of our purposes. We assume that any population in the intermediate state  $|i\rangle$  will decay to states  $|g\rangle$  and  $|r\rangle$  at partial rates  $\Gamma_{i,g}$  and  $\Gamma_{i,r}$ , respectively. These rates are related to the total decay rate  $\Gamma_i$  and lifetime  $\tau_i$  of state  $|i\rangle$  via

$$\Gamma_i = \frac{1}{\tau_i} = \Gamma_{i,g} + \Gamma_{i,r}. \quad (3.1)$$

The *branching fraction* for a transition to state  $|g\rangle$  is defined as

$$f_{i,g} := \frac{\Gamma_{i,g}}{\Gamma_i} = \frac{\Gamma_{i,g}}{\Gamma_{i,g} + \Gamma_{i,r}}, \quad (3.2)$$

representing the probability for population in state  $|i\rangle$  to decay to  $|g\rangle$ . The branching fraction  $f_{i,r}$  for a transition to state  $|r\rangle$  is defined analogously.

For the generation of a Raman photon emitted on the transition from  $|i\rangle$  to  $|g\rangle$ , we initially prepare the atom in state  $|r\rangle$ . For most of our purposes, as we will see later, it is favorable to generate photons of long temporal shape. Thus we enter the regime of weak excitation, as mentioned above, implying  $\Omega \ll \Gamma_i$  for the Rabi frequency  $\Omega$  of the laser coupling states  $|r\rangle$  and  $|i\rangle$ . Similar to a two-level system, we can define a *quasi-steady state*: since the atomic system relaxes at rate  $\Gamma_i$ , much faster than the Rabi frequency  $\Omega$ , no coherent atomic dynamics evolve. Instead, the subsystem of the two states  $|r\rangle$  and  $|i\rangle$  relaxes into a steady state at rate  $\Gamma_i$  with a low population in state  $|i\rangle$ . Thus population loss from the subsystem through decay to the ground state  $|g\rangle$  occurs on a much longer time scale than the relaxation, and we may hence call the state of the subsystem quasi-steady. At time  $t = 0$ , the quasi-steady population of state  $|i\rangle$  is [119]

$$\rho_i = \frac{\Omega^2}{(2\Delta)^2 + \Gamma_i^2} \quad (3.3)$$

with the detuning  $\Delta$  of the laser from the atomic resonance. On longer time scales, population loss to state  $|g\rangle$  becomes noticeable; the rate at which population accumulates in  $|g\rangle$  is given by the quasi-steady population of state  $|i\rangle$  and the decay rate to  $|g\rangle$ :

$$\dot{\rho}_g = \Gamma_{i,g} \cdot \rho_i \quad (3.4)$$

This population transfer makes the quasi-steady state population of state  $|i\rangle$  time-dependent, changing eqn. 3.3 accordingly:

$$\rho_i(t) = \frac{\Omega^2}{(2\Delta)^2 + \Gamma_i^2} (1 - \rho_g(t)) \quad (3.5)$$

Taking the time derivative then yields a differential equation,

$$\dot{\rho}_i = -\frac{\Omega^2}{(2\Delta)^2 + \Gamma_i^2} \dot{\rho}_g \quad (3.6)$$

$$= -\Gamma_{i,g} \frac{\Omega^2}{(2\Delta)^2 + \Gamma_i^2} \rho_i, \quad (3.7)$$

from which we readily obtain the population of the intermediate state,

$$\rho_i(t) = \rho_i(0) e^{-Rt}, \quad (3.8)$$

with transfer rate  $R := \Gamma_{i,g} \frac{\Omega^2}{(2\Delta)^2 + \Gamma_i^2}$  and initial value  $\rho_i(0) = \frac{\Omega^2}{(2\Delta)^2 + \Gamma_i^2}$ .

The temporal behavior of  $\rho_i(t)$  is directly reflected in the temporal envelope (shape) of the scattered Raman photon; since the probability for the emission of a photon at any point  $t$  in time is proportional to the intermediate-state population, the probability distribution for detecting the photon at a certain time  $t$  is

$$p(t) = \frac{1}{\tau_{\text{ph}}} e^{-t/\tau_{\text{ph}}} \Theta(t) \quad (3.9)$$

with the photon duration  $\tau_{\text{ph}} := 1/R$  and the Heaviside step function  $\Theta$ . Thus the Raman process yields a single photon with exponential temporal shape of which we can tune the duration through intensity and detuning of the driving laser field. In particular, we find  $\tau_{\text{ph}} \propto 1/\Omega^2$ .

We should mention at this point that we cannot assign an electromagnetic wave to the photon as we would to a classical light field (e.g. a laser field). As described in detail in [153], the expectation value for the electric-field operator in the case of a *photon number state* (the quantum-mechanical description of a single photon) yields zero. In particular, such a state does not possess a defined phase, making it differ greatly from classical fields. The operator for the field intensity, however, yields non-zero values for such non-classical states. Thus the single photon may very well be described by a temporal intensity distribution, which is proportional to the detection probability distribution  $p(t)$ .

Complementary to the photon's temporal shape, we will discuss its spectral properties in the next section.

### Photonic spectrum

As mentioned earlier, the properties of a single photon scattered from a two-level atom under pulsed excitation are solely determined by atomic properties. This includes the photonic spectrum, its bandwidth given by the decay rate of the excited state. In the case of Raman-scattered photons, however, this issue is very different.

We will first discuss the case  $\Gamma_{i,r} \ll \Gamma_{i,g} \approx \Gamma_i$ , i.e. we assume spontaneous decay from state  $|i\rangle$  back to  $|r\rangle$  to be negligible compared with decay to the ground state  $|g\rangle$ . Under this condition, the atom is coherently transferred from  $|r\rangle$  to  $|g\rangle$  under emission of a single photon. *Coherently* in this context means that during the emission process, no quantum information leaks from the joint system of atom and photon to the environment. Loss of quantum information from the joint system would be perceived as decoherence, instead the system remains in a pure quantum state. Since the atom is in a pure state before as well as after the scattering process, so must the photon. The interpretation of this pure photonic state lies in a Fourier relation between its temporal and spectral shape, i.e. its spectrum is directly determined by its temporal shape through Fourier transformation. Interestingly, this means that for long wave packets (from weak laser excitation), the photonic spectrum is much narrower than the natural transition linewidth  $\Gamma_i$ .

### 3.1. Generation of single photons

---

It is instructive to consider the problem from another point of view, namely in terms of time-energy uncertainty. Population is transferred from the initial state  $|r\rangle$  to the final state  $|g\rangle$ , i.e. the lifetime of state  $|r\rangle$  is artificially shortened to the value  $1/R = \tau_{\text{ph}}$  by the laser excitation. According to the principle of time-energy uncertainty, the state's energy is thus only defined within  $\sim \hbar R$ , and due to energy conservation, this uncertainty must be reflected in the photonic spectrum. Again, the intermediate-state decay rate  $\Gamma_i$  is not a limiting factor.

For our photonic wave packets, their temporal probability distribution  $p(t)$  being of exponential shape with  $\frac{1}{e}$  duration  $\tau_{\text{ph}}$ , the spectral probability distribution is given by the Fourier transform and yields a Lorentzian shape,

$$S(\omega) = \frac{2}{\pi \tau_{\text{ph}}} \frac{1}{4(\omega - \omega_0)^2 + 1/\tau_{\text{ph}}^2}, \quad (3.10)$$

with angular frequency  $\omega$  and carrier frequency  $\omega_0$  (see app. A.5 for a derivation). Note that the FWHM value of the distribution is directly given by the inverse photon duration  $1/\tau_{\text{ph}}$ , thus long photons (created by weak excitation) will have a bandwidth much smaller than the natural transition linewidth.

Like the photon's bandwidth, we can tune its carrier frequency  $\omega_0$  as well. Since the scattering process starts and ends with the atom in a state of well-defined energy, a change in the detuning  $\Delta$  of the driving laser is directly reflected in the photonic carrier frequency. More precisely, with energies  $\hbar\omega_i$  and  $\hbar\omega_g$  of the states  $|i\rangle$  and  $|g\rangle$ , respectively, the carrier frequency is given by

$$\omega_0 = \Delta + (\omega_i - \omega_g). \quad (3.11)$$

Thus we can generate single photons whose spectrum is shifted from the atomic-transition resonance by much more than the photonic bandwidth. Obviously, for ever larger detuning values, the transfer rate becomes lower (for equal excitation power) and thus the photonic wave packet longer, but this can in part be compensated for by an increase of the driving-laser intensity. For detunings large compared with the natural transition linewidth  $\Gamma_i$ , the condition of "weak excitation" relaxes from  $\Omega \ll \Gamma_i$  to  $\Omega \ll \Delta$ .

At this point, we should mention the effect of a finite linewidth of the driving laser: if the laser source contains incoherent frequency contributions, the detuning between excitation and atomic transition becomes less well-defined. In detail, the photonic spectrum is now given by the convolution of the photonic spectrum from eqn. 3.10 and the laser's spectral distribution. Thus a sufficiently incoherent excitation considerably broadens the photonic spectrum. However, in the experimental realization shown in section 3.1.2, this effect is negligible.

All the considerations so far concerning the photonic spectrum were made for the special case of negligible spontaneous decay back to the initial state  $|r\rangle$ , and we will now discuss the more general case.

#### Decoherence through parasitic spontaneous decay

In the case where spontaneous decay from state  $|i\rangle$  to state  $|r\rangle$  during the scattering process is no longer negligible, photons scattered on the transition between states  $|i\rangle$  and  $|r\rangle$  must

be taken into account. We call these photons *parasitic* as they break up the Fourier limitation of the Raman photons emitted on the transition from  $|i\rangle$  to  $|g\rangle$ . Intuitively, this can be understood as decoherence, caused by the leakage of quantum information from the joint system of atom and Raman photon. We will now discuss this issue in more detail.

Populating the intermediate state  $|i\rangle$  yields a certain probability for the emission of a Raman and a parasitic photon, respectively, the ratio of the two given by the ratio of the decay rates  $\Gamma_{i,g}$  and  $\Gamma_{i,r}$ . The expectation value for the number of parasitic photons scattered before the Raman photon is emitted thus amounts to

$$\bar{n} = \frac{\Gamma_{i,r}}{\Gamma_{i,g}} = \frac{f_{i,r}}{f_{i,g}}, \quad (3.12)$$

and the individual numbers  $n$  of parasitic photons follow the exponential distribution

$$P(n) = \frac{\bar{n}^n}{(\bar{n} + 1)^{n+1}}. \quad (3.13)$$

We will now first consider the individual cases of  $n = 0, 1, 2, \dots$  parasitic photons, the probabilities of which are given by  $P(n)$ . Conditioned on the event of no parasitic photons,  $n = 0$ , the spontaneous decay from state  $|i\rangle$  to  $|g\rangle$  occurs at the *full* decay rate  $\Gamma_i$ , not the partial rate  $\Gamma_{i,g}$ . This is because the process is conditioned on not scattering any parasitic photons, thus the decay of state  $|i\rangle$  is exclusively directed toward state  $|g\rangle$ . The duration of the Raman wave packet described by

$$p^{(0)}(t) = p(t) = \frac{1}{\tau_{\text{ph}}} e^{-t/\tau_{\text{ph}}} \Theta(t) \quad (3.14)$$

is hence

$$\tau_{\text{ph}} = \left( \Gamma_i \frac{\Omega^2}{(2\Delta)^2 + \Gamma_i^2} \right)^{-1}. \quad (3.15)$$

Conditioned on the emission of exactly one parasitic photon,  $n = 1$ , the Raman photon is “delayed” by however long it takes to scatter the parasitic photon. The latter is given by the probability distribution of the parasitic photon, which is identical to that for the Raman photon. This may be understood by noting that, although the probabilities for a Raman and parasitic photon are different, their temporal structure is not. The temporal shape of the Raman photon is then calculated by convolving the probability distributions of the Raman and parasitic photon:

$$p^{(1)}(t) = (p * p)(t) \quad (3.16)$$

We now make use of the convolution power, the  $k$ -fold convolution of a function  $p$  with itself:

$$p^{*k} = p * p^{*(k-1)} \quad (3.17)$$

with  $p^{*0} = \delta$ , the Dirac delta function. Then we express the probability distribution of the Raman photon conditioned on  $n$  parasitic photons as

$$p^{(n)}(t) = p^{*(n+1)}(t), \quad (3.18)$$

### 3.1. Generation of single photons

---

which is evaluated analytically to yield

$$p^{(n)}(t) = \frac{1}{n!} \left( \frac{t}{\tau_{\text{ph}}} \right)^n \frac{1}{\tau_{\text{ph}}} e^{-t/\tau_{\text{ph}}} \Theta(t) \quad (3.19)$$

$$= \frac{1}{n!} \left( \frac{t}{\tau_{\text{ph}}} \right)^n p(t). \quad (3.20)$$

Since all the probability distributions  $p^{(n)}(t)$  are realized with probabilities  $P(n)$ , we take the weighted average

$$\bar{p}(t) = \sum_{n=0}^{\infty} P(n) p^{(n)}(t). \quad (3.21)$$

This describes an incoherent mixture of photonic wave packets, which pertains to our situation since the emission of parasitic photons is a stochastic process. Analytic evaluation finally yields the prolonged temporal probability distribution for the Raman photon

$$\bar{p}(t) = \frac{1}{\bar{\tau}_{\text{ph}}} e^{-t/\bar{\tau}_{\text{ph}}} \Theta(t) \quad (3.22)$$

with the modified photon duration

$$\bar{\tau}_{\text{ph}} = \tau_{\text{ph}} (\bar{n} + 1). \quad (3.23)$$

Hence the Raman photon is still of exponential shape, as in the case of negligible decay back to state  $|r\rangle$ , but is longer by a factor of  $\bar{n} + 1$ . Expressing both  $\bar{n}$  and  $\tau_{\text{ph}}$  in term of the decay rates (eqns. 3.12 and 3.15) yields

$$\bar{\tau}_{\text{ph}} = \left( \Gamma_i \frac{\Omega^2}{(2\Delta)^2 + \Gamma_i^2} \right)^{-1} \left( \frac{\Gamma_{i,r}}{\Gamma_{i,g}} + 1 \right) \quad (3.24)$$

$$= \left( \Gamma_{i,g} \frac{\Omega^2}{(2\Delta)^2 + \Gamma_i^2} \right)^{-1}. \quad (3.25)$$

Now we have come full circle; this expression for  $\bar{\tau}_{\text{ph}}$  corresponds to what we found earlier for the transfer rate from state  $|r\rangle$  to  $|g\rangle$ , not taking into account parasitic photons but using the partial decay rates instead. The interesting part, however, lies in the spectrum corresponding to the temporal shape  $\bar{p}(t)$ . Since  $\bar{p}(t)$  describes an incoherent mixture of photonic wave packets, its spectrum is given by the corresponding mixture of the individual photonic spectra.

Let us examine these spectra a little more closely; in the event of no parasitic photons,  $n = 0$ , the temporal shape is  $p^{(0)}(t) = p(t)$ , and its spectral probability distribution  $S(\omega)$  is given by the Fourier transform from eqn. 3.10. For exactly one parasitic photon,  $n = 1$ , we need to make yet another assumption: in principle, it is possible to detect the point in time at which the parasitic photon was emitted. This detection process projects the atom back onto state  $|r\rangle$ , from which it is re-excited, this time scattering the Raman photon. Using the detection event as the zero point in time, the Raman photon's temporal shape is once more given by  $p(t)$ , and hence its spectral shape is described by the Fourier

transform  $S(\omega)$  as well. However, since we are not concerned with detecting parasitic photons, the zero point in time is uncertain by the probability distribution of the parasitic photon, as described above. This results in the modified temporal shape  $p^{(1)}(t)$ , which is a stochastic effect, leaving the spectrum unaffected. Thus all contributions  $p^{(n)}(t)$  possess the same spectral properties (and so does the total distribution  $\bar{p}(t)$ ), namely those of the distribution  $S(\omega)$ ; the FWHM value of this Lorentzian spectrum is  $1/\tau_{\text{ph}}$  and *not*  $1/\bar{\tau}_{\text{ph}}$ .

Although both the temporal and spectral properties of the resulting Raman photon are functions of the driving-laser properties, the time-bandwidth product depends on atomic properties only:

$$\bar{\tau}_{\text{ph}} \cdot \frac{1}{\tau_{\text{ph}}} = \left( \Gamma_{\text{i,g}} \frac{\Omega^2}{(2\Delta)^2 + \Gamma_{\text{i}}^2} \right)^{-1} \Gamma_{\text{i}} \frac{\Omega^2}{(2\Delta)^2 + \Gamma_{\text{i}}^2} \quad (3.26)$$

$$= \frac{\Gamma_{\text{i,r}}}{\Gamma_{\text{i,g}}} + 1 \quad (3.27)$$

$$= \bar{n} + 1 \quad (3.28)$$

The time-bandwidth product is a measure for the purity of a photonic state and, for many application, should be close to 1. Values much greater than 1, however, indicate significant decoherence of the photonic state through the emission of parasitic photons. Such states are usually unsuited for the faithful representation and transfer of quantum information.

## Summary

In conclusion, spontaneous Raman transitions in a suitably chosen three-level system allow for the generation of single photons tunable both temporally and spectrally through intensity and detuning of the driving laser. In principle, the photon duration as well as the center of the photonic spectrum can be tuned over an arbitrarily wide range.

However, these photons are in general not Fourier-limited and hence not in a pure quantum state, owing to the emission of parasitic photons on the transition excited by the driving laser. In the case of an unfavorable ratio of the partial decay rates, the time-bandwidth product exceeds the desired value of 1 significantly.

### 3.1.2 Experimental realization

After discussing the theoretical background on single photons generated from spontaneous Raman processes, I now present the experimental implementation. After introducing the experimental sequence, I will present the configuration of our setup for the generation and collection of single photons, followed by the results benchmarking the quality of our single-photon source.

#### Experimental sequence

We implement the three-level system used in the theoretical description above through three of the five fine-structure manifolds of  $^{40}\text{Ca}^+$ . While the intermediate state  $|i\rangle$  is

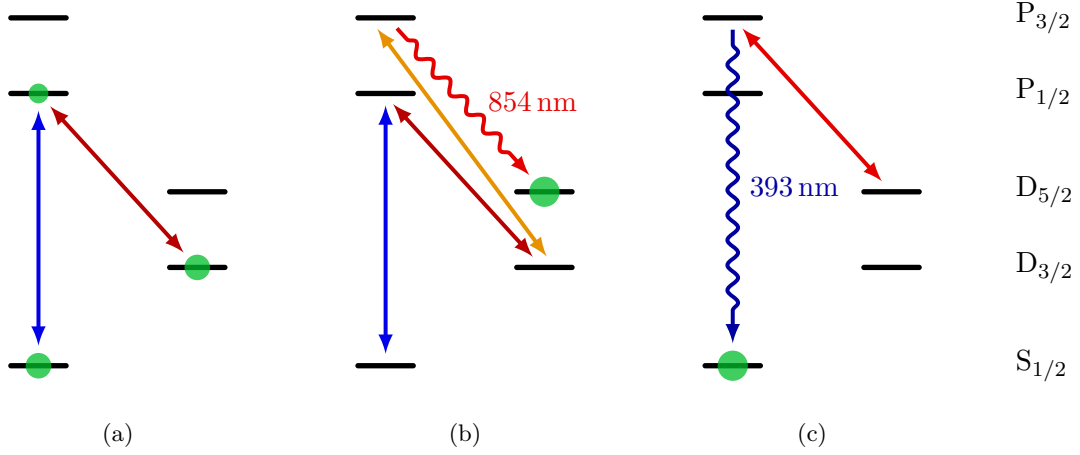


**Fig. 3.2:** Experimental sequence for the alternating generation of single Raman photons at two different wavelengths. (a) Doppler cooling of the atomic motion. (b) Generation of a single photon at 854 nm scattered on the  $D_{5/2}$ - $P_{3/2}$  transition. (c) Generation of a single photon at 393 nm scattered on the  $S_{1/2}$ - $P_{3/2}$  transition.

realized through the  $P_{3/2}$  manifold, the  $S_{1/2}$  and  $D_{5/2}$  states are used interchangeably for implementing the initial state  $|r\rangle$  and the final state  $|g\rangle$ .

The experimental cycle, sketched in fig. 3.2, starts with Doppler cooling the ion's motion on the  $S_{1/2}$ - $P_{1/2}$  transition at 397 nm, typically for  $0.6 - 1 \mu\text{s}$ . This is facilitated by repumping population from the metastable  $D_{3/2}$  state through a laser at 866 nm. Next, the generation of a single photon at 854 nm wavelength is initiated by switching on an additional laser at 850 nm, resonant with the  $D_{3/2}$ - $P_{3/2}$  transition. The Rabi frequencies and detunings of the three lasers with respect to their transitions are optimized as to realize a three-photon resonance that effectively couples the  $S_{1/2}$  and  $P_{3/2}$  state. Ideally, this excitation will not populate the  $P_{1/2}$  or  $D_{3/2}$  state, but instead will transfer all population from  $S_{1/2}$  to  $D_{5/2}$  through the emission of a spontaneous Raman photon on the 854 nm transition. The duration of this process depends on the transfer rate, given by the parameters of the three lasers, and is in the range of  $5 - 30 \mu\text{s}$ .

In the final step of the sequence, the three lasers are turned off, and a laser at 854 nm is switched on instead. This repumps all population from the  $D_{5/2}$  back to the ground state, scattering a single Raman photon on the  $S_{1/2}$ - $P_{3/2}$  transition at 393 nm. Typical values for the duration of this step are  $2 - 7 \mu\text{s}$ . This completes the experimental cycle before Doppler cooling is resumed.

For more technical details, see Michael Schug's Ph.D. thesis [93].

### Experimental configuration

A well-established method to enhance the collection of light scattered from an atom is found in cavity QED [145, 146, 147, 154]. Placing a single atom (or ion) inside an optical cavity of sufficient finesse and solid angle subtended greatly increases the light-collection

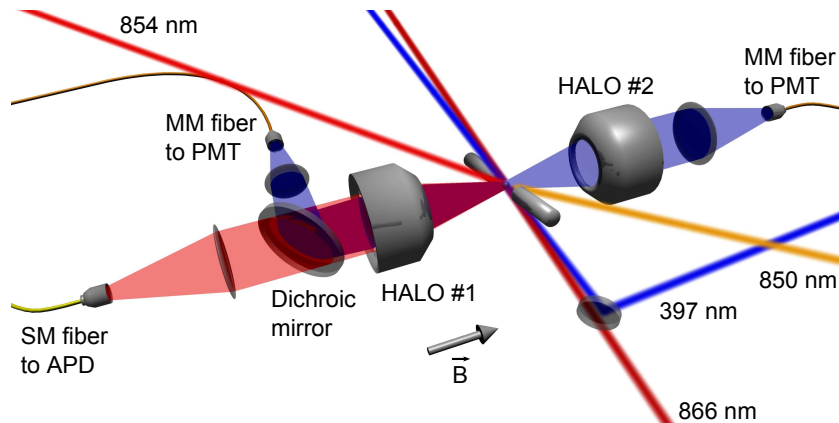


**Fig. 3.3:** Experimental setup for the generation of single Raman photons at 854 nm and 393 nm wavelength.  $\vec{B}$ : magnetic-field direction, SM fiber: single-mode optical fiber, MM fiber: multi-mode optical fiber, PMT: photomultiplier tube.

efficiency. However, combining this technique with ion traps for local multi-qubit information processing is technically challenging, since the size of a cavity around an ion trap is not easily reduced below the mm-scale.

Instead of a cavity, we make use of our two high-NA laser objectives (HALOs). As described in section 1.2.2, they each collect  $\sim 4.2\%$  of the light scattered by the ion (in the case of isotropic emission). The use of both HALOs simultaneously enables us to collect light at two different wavelengths and hence to generate and collect photons from both the transition at 854 nm and at 393 nm. Since the lenses that compose the HALOs exhibit significant dispersion, each HALO must be aligned individually with respect to the ion in order to efficiently collect light at the respective wavelength. With the aid of additional optics, we even use one of the HALOs for both wavelengths at the same time.

The experimental setup is depicted in fig. 3.3; HALO #1 is positioned via its piezo actuators such that its focal spot for light at 854 nm coincides with the ion's position. By means of a confocal telescope, the beam diameter is reduced such as to couple the light efficiently to a single-mode optical fiber ( $\sim 60\%$  coupling efficiency). At the same time, the HALO is used for the collection of light at 397 nm (not 393 nm) for the purpose of detecting atomic fluorescence from the  $S_{1/2}$ - $P_{1/2}$  cooling transition. This is facilitated by a dichroic mirror which separates blue from red light. Since the HALO shows normal dispersion, blue light exits the vacuum chamber in a slightly convergent beam. A non-confocal telescope collimates the beam before it is coupled to a multi-mode optical fiber with  $\sim 55\%$  efficiency. The coupling efficiency is significantly lower as compared with the case of the HALO being aligned with the ion for blue light (see below), as only the latter makes full use of the HALO's numerical aperture. When collecting light at 393 nm instead, we must once more compensate for the optics' dispersion by the combination of a convex and concave lens behind the telescope. Placed on a magnetic mount, this enables flexible switching between efficient collection at 397 nm and 393 nm, respectively. HALO #2, on the other hand, is aligned for light at 397 nm, again optimized for the collection

### 3.1. Generation of single photons

---

of atomic fluorescence. By means of another composite compensation lens placed on a magnetic mount, 393 nm light collected by HALO #2 is coupled to a second multi-mode fiber with  $\sim 85\%$  efficiency.

The light coupled to the optical fibers is detected by single-photon detectors; for the light at 854 nm, we employ an avalanche photodiode (APD) of 24(5) % quantum efficiency, while at 393 nm, we use photomultiplier tubes of 28(1) % quantum efficiency. The detector output pulses are then fed into our time-correlated single-photon counter (PicoHarp), time-tagging the individual photon-detection events and saving them on a computer for analysis.

All laser beams are focused onto the ion from collimated beams of 2.15 mm diameter through simple plano-convex lenses. The focal-spot diameters are  $\sim 120\ \mu\text{m}$  (397 nm),  $250\ \mu\text{m}$  (866 nm) and  $125\ \mu\text{m}$  (850 nm and 854 nm).

#### Single photons at 854 nm

For the detection and evaluation of single Raman photons at 854 nm wavelength, the APD is connected to one of PicoHarp's inputs. The APD is gated on during photon generation only, discarding detection events outside this time window. PicoHarp's second input is used to record the time base by receiving a trigger signal from the sequence-control unit (Hydra) each time the laser at 850 nm is switched on, signaling the beginning of the photon generation. The recorded data is analyzed by time-correlating the photon-detection events with the trigger and sorting them into an arrival-time histogram. Such a histogram directly reflects the temporal shape of the photonic wave packet. Fig. 3.4(a) displays arrival-time histograms for different values of the 850 nm laser power. The higher the power, the higher the rate at which population is transferred to the  $D_{5/2}$  state and hence the shorter the photonic wave packet. In this particular experiment, we tuned the photon's duration<sup>1</sup> from  $\sim 0.8\ \mu\text{s}$  to  $\sim 3.3\ \mu\text{s}$  by appropriately choosing the 850 nm laser power. This time scale is much longer than the  $P_{3/2}$ -state lifetime ( $\sim 7\ \text{ns}$  [121]), which defines the rate at which the ion relaxes to the quasi-steady state. This means that the requirements for describing the photonic wave packets by the theoretical model from section 3.1.1 are fulfilled.

From the shortest photons generated in this experiment, we obtain a detection efficiency of 0.481(3) %. This value differs from the one stated in section 1.2.2 ( $\sim 0.6\%$ ) since at this point, the fiber coupling was not yet fully optimized. At a sequence repetition rate of 55.5 kHz and accounting for the APD quantum efficiency, we obtain single-mode coupled photons at a rate of  $1.1(2) \cdot 10^3\ \text{s}^{-1}$ . However, after further optimizing both the experimental sequence and the fiber coupling, we could increase the repetition rate to 125 kHz and achieve  $3.0(6) \cdot 10^3\ \text{s}^{-1}$  fiber-coupled photons [155].

#### Single photons at 393 nm

For the generation of single Raman photons at 393 nm, the output pulses from the two PMTs are combined and fed into PicoHarp, gated on while repumping the atomic popula-

---

<sup>1</sup>We define the photon's duration as the  $\frac{1}{e}$  time of an exponential function fitted to the falling slope of the wave packet.

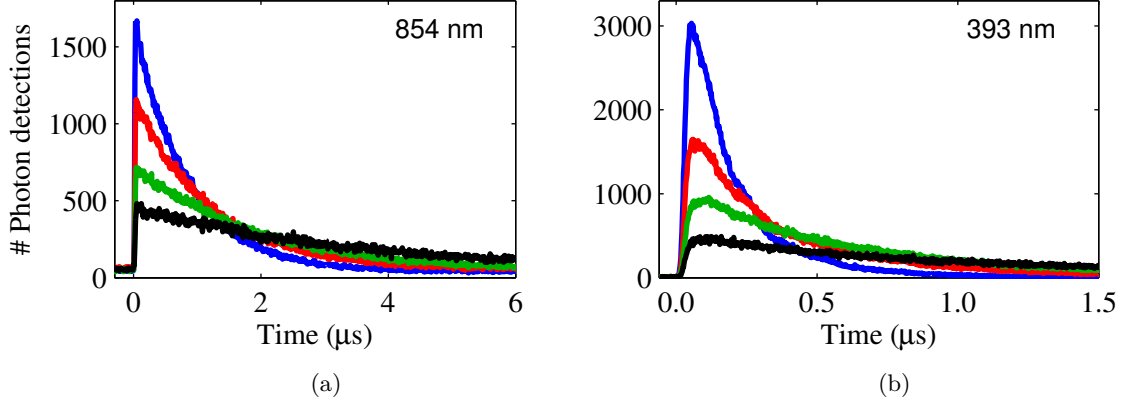


**Fig. 3.4:** Arrival-time histograms for the generation and detection of single Raman photons. (a) Raman photons at 854 nm, emitted on the  $D_{5/2}$ - $P_{3/2}$  transition. The bin size is 10 ns and the measurement time per histogram is 15 min. The photon duration is 0.83(3)  $\mu$ s (blue curve, 316  $\mu$ W of 850 nm laser power), 1.186(7)  $\mu$ s (red, 158  $\mu$ W), 1.95(1)  $\mu$ s (green, 79  $\mu$ W) and 3.42(5)  $\mu$ s (black, 40  $\mu$ W). (b) Raman photons at 393 nm, emitted on the  $S_{1/2}$ - $P_{3/2}$  transition. The bin size is 2 ns and the measurement time per histogram is 6 min. The photon duration is 157.0(6) ns (blue curve, 14  $\mu$ W of 854 nm laser power), 292(1) ns (red, 7  $\mu$ W), 547(4) ns (green, 3.5  $\mu$ W) and 770(20) ns (black, 1.75  $\mu$ W).

tion from the  $D_{5/2}$  to the ground state. The trigger from Hydra used for the time base now marks the onset of the 854 nm laser light which generates the 393 nm photon. Arrival-time histograms for various values of 854 nm laser power are shown in fig. 3.4(b), exhibiting wave-packet durations between  $\sim 160$  ns and  $\sim 770$  ns. Although, as for our 854 nm photons, the wave-packet duration is appreciably longer than the  $P_{3/2}$ -state lifetime, the rising slope becomes noticeable. This is an artifact of the acousto-optic modulator used for controlling the 854 nm beam, its switching time being in the range of 20 – 30 ns.

In order to maximize the rate of fiber-coupled photons, calculations showed that it is optimal to pump 73 % of the atomic population into the  $D_{5/2}$  manifold before generating the photon. This yields a lower probability for a photon in a single cycle but increases the repetition rate accordingly. For the shortest photons shown in fig. 3.4(b), we measured 0.905(2) % combined detection efficiency, once more lower than the optimized values that we achieved at a later stage of the experiment. At 171 kHz repetition rate, we thus obtain  $5.5(2) \cdot 10^3 \text{ s}^{-1}$  multi-mode coupled photons. Similar values are found in our publication [88].

### Single photons in comparison

The most prominent difference between our single photons at 854 nm and at 393 nm are their durations and the laser power/intensity at which these are attained. While for photons at 854 nm, several hundred  $\mu$ W of light at 850 nm are required to bring the wave-packet duration below 1  $\mu$ s, the same is achieved at 393 nm with merely  $\sim 1$   $\mu$ W of 854 nm light. The reason for this is twofold: (i) The three-photon coupling between states  $S_{1/2}$

### 3.1. Generation of single photons

---

and  $P_{3/2}$  is far less efficient than the direct excitation of an electronic transition, i.e. the effective Rabi frequency is much lower on the  $S_{1/2}$ - $P_{3/2}$  than on the  $D_{5/2}$ - $P_{3/2}$  transition. (ii) The branching fractions of the two transitions are  $f_{393} = 0.935$  and  $f_{854} = 0.0587$  [156], thus population in the  $P_{3/2}$  state will predominantly decay to the ground state. Hence even for similar Rabi frequencies on the two transitions, scattering a photon at 854 nm takes much longer than at 393 nm.

The second point leads us directly to the question of the photonic spectrum; as elaborated on in the theoretical section 3.1.1, the ratio of branching fractions is decisive in whether a single-photon state is Fourier-limited. For the remainder of the discussion, we will neglect spontaneous decay on the  $D_{3/2}$ - $P_{3/2}$  transition at 850 nm as its branching fraction amounts to  $6.6 \cdot 10^{-3}$  only [156]. When generating single photons at 854 nm, the mean number of parasitic photons at 393 nm is  $\bar{n}_{393} = f_{393}/f_{854} = 15.9$ , resulting in a time-bandwidth product of photons at 854 nm of  $\sim 17$ . Hence these photons are far from Fourier-limited. However, temporal selection allows for reducing the time-bandwidth product; as explained in detail in app. A.6, the later the Raman photon is detected, the greater the number of parasitic photons that may have been emitted before. Hence selecting Raman photons from only a small time window at the beginning of the wave packet significantly reduces the time-bandwidth product. Of course, this method reduces the rate of usable photons accordingly.

Matters are different for single photons at 393 nm; with a mean number of parasitic photons at 854 nm of  $\bar{n}_{854} = f_{854}/f_{393} = 0.0628$ , Raman photons at 393 nm would be very close to the Fourier limit if it were not for the Zeeman substates of the three fine-structure manifolds. Since a static magnetic field is needed for efficient Doppler cooling, the Zeeman levels are no longer degenerate. By the simple sequence employed here, the ion is not prepared in a specific Zeeman state but rather a statistical mixture. The subsequent Raman photon will thus be in a mixture of polarization and frequency states, once more increasing the time-bandwidth product. However, as demonstrated in [88, 93], we have developed a technique based on optical pumping in order to prepare the ion in a specific  $D_{5/2}$  state. By virtue of the favorable branching fractions, we were able to generate single Fourier-limited Raman photons at 393 nm in a quantum state of pure polarization and frequency.

I should mention at this point that we are planning on experimentally determining the photonic spectra both at 854 nm and 393 nm; Fabry-Pérot cavities, acting as spectral filters, with resolutions of  $\sim 1$  MHz are currently being set up. Measuring the rate of single photons behind such a cavity while scanning its resonance frequency will give us knowledge of the photons' spectral probability distributions.

#### **Characterization of multi-photon contribution**

In the above sections, we have discussed the temporal and spectral properties of our single photons both at 854 nm and 393 nm wavelength as well as the rate and efficiency at which they can be generated. The only relevant aspect not yet mentioned is the multi-photon contribution, i.e. the likelihood that a photonic wave packet contains more than one photon. In theory, our scheme allows for no more than exactly one Raman photon

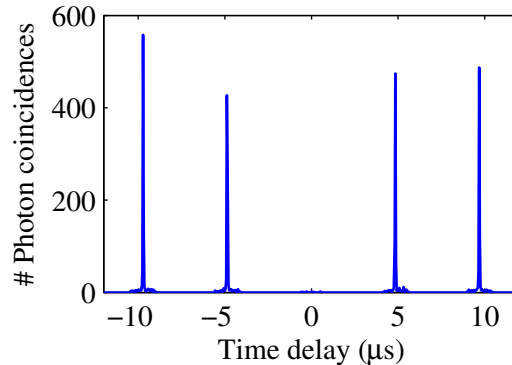


**Fig. 3.5:** Intensity autocorrelation function for single Raman photons at 393 nm wavelength. The bin size is 40 ns and the measurement time is 6 min. The repetition rate is 206 kHz, corresponding to 4.9  $\mu$ s spacing between neighboring peaks.

emitted by the ion; once a photon has been scattered, the ion is projected onto the final state  $|g\rangle$ , from which it cannot be re-excited by the driving laser. Under realistic conditions, however, there is a chance that the ion is excited from the final state by the laser(s) that had prepared the ion in the initial state  $|r\rangle$ . Typically, this effect stems from the acousto-optic modulators used to switch the state-preparation lasers. Since both their switching times and attenuations are different from zero, light that excites the ion from the final state might be present during photon generation. However, as we will see, the multi-photon contribution is very low, and we will hence restrict ourselves to the case of single-photon and two-photon events. We define the two-photon contribution  $p_2$  as the probability for the ion to emit a second Raman photon after the detection of the first projected the ion onto the final state  $|g\rangle$ .

For the experimental determination of the two-photon contribution, one could for example make use of photon-number-resolving detectors. Since, however, we employ “conventional” single-photon detectors in our setup, we resort instead to a Hanbury-Brown-Twiss (HBT) interferometer [157]. It is based on a non-polarizing beam splitter which has a chance of separating photons that impinge simultaneously on the beam splitter. The coincidental detection of photons in both beam-splitter outputs then signals the presence of at least two photons. The histogram of coincidences between detection events in the two outputs then represents the *intensity autocorrelation function* ( $g^{(2)}$  function) of the photonic light field, as shown in fig. 3.5 for the case of single photons at 393 nm. Here, the ion itself plays the role of the beam splitter, as we use both HALOs simultaneously to collect and detect light at 393 nm. The autocorrelation function is reconstructed by temporally correlating the detection events of the two PMTs. As is seen from fig. 3.5, the central correlation peak at zero time delay is very small compared with the neighboring peaks, the latter representing coincidences from photon detections at different experimental cycles. As shown in app. A.7, the ratio of number of events from the central peak and one of the others is sufficient to derive the two-photon probability  $p_2$ . From 12 detection events in the central peak, 785 events in the one at 5  $\mu$ s delay and accounting for detector

dark counts (see app. A.7), we deduce  $p_2 = 0.33(15)\%$ . Thus the light field scattered by the ion at 393 nm exhibits an excellent single-photon character.

Unfortunately, we were unable to characterize the quality of single photons at 854 nm wavelength. Since only one of the HALOs is aligned for the collection of light at 854 nm, we tried using a fiber beam splitter for light coupled to the single-mode optical fiber. This beam splitter, however, showed significant losses up to the point where true two-photon events were no longer discernible from the background induced by detector dark counts.

#### Summary

In conclusion, we have experimentally demonstrated the generation of single Raman photons at two different wavelengths (854 nm and 393 nm), tunable both temporally and spectrally and using one and the same experimental sequence. For photons at 393 nm, the Fourier limit may be attained through additional optical-pumping techniques. At this wavelength, we also assessed the single-photon character of the light field by means of the intensity autocorrelation function, yielding a very low multi-photon probability.

## 3.2 Atom-to-photon phase mapping

In the first part of this chapter, I presented both the theoretical background and the experimental implementation for the generation of single Raman photons from a single ion. Although we could tune the photons' temporal and spectral properties through the power of the driving laser, we did not use the photons as carriers of quantum information. In this section, I briefly describe two schemes that allow us to map atomic phase information onto the quantum state of a single photon. This is a summary of a part of Michael Schug's Ph.D. thesis [93]; details are found therein, as well as in our publication [89].

### 3.2.1 Quantum beats

In the first of two experimental schemes ("A scheme"), we realize atom-to-photon phase transfer through the interference of two absorption paths, as illustrated in fig. 3.6(a). After preparing a superposition of two atomic energy eigenstates ( $|D_{5/2}, m = -3/2\rangle$  and  $|D_{5/2}, m = +1/2\rangle$ ), a driving laser couples the two states simultaneously to one and the same excited state ( $|P_{3/2}, m = -1/2\rangle$ ). Population from the excited state decays predominantly to the  $S_{1/2}$  ground-state, releasing a single Raman photon. For an appropriate phase between the two absorption paths, their interference is constructive, i.e. population is transferred from the  $D_{5/2}$  to the  $S_{1/2}$  state at an increased rate as compared with non-interfering absorption paths. The interference may become destructive as well, resulting in suppression of population transfer. The phase between the absorption paths, given by the superposition phase, hence determines the rate at which the Raman photon is generated and thus its temporal shape.

In the second scheme ("V scheme"), we make use of interference of two emission paths, as shown in fig. 3.6(b). The ion is prepared in a superposition of two energy eigenstates ( $|D_{5/2}, m = -5/2\rangle$  and  $|D_{5/2}, m = +3/2\rangle$ ) which are coupled to distinct excited states,

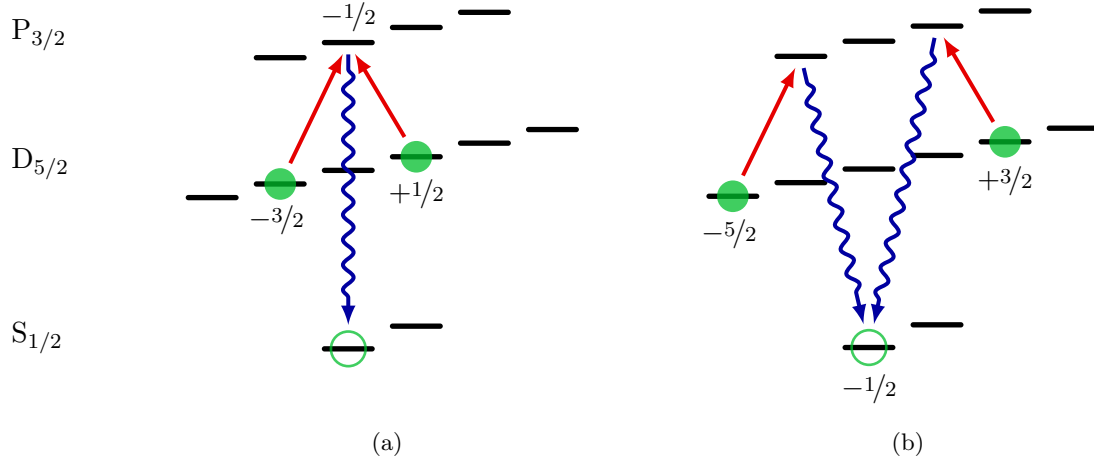


**Fig. 3.6:** Schemes for atom-to-photon phase mapping through interference. (a)  $\Lambda$  scheme: interference in the absorption paths of a photon on the  $D_{5/2}$ - $P_{3/2}$  transition. (b)  $V$  scheme: interference in the emission paths of a photon on the  $S_{1/2}$ - $P_{3/2}$  transition.

hence the absorption paths do not interfere. Interference takes place instead between the emission paths from the excited states to the ground state ( $|S_{1/2}, m = -1/2\rangle$ ). One emission path yields a Raman photon in the quantum state  $|\sigma^+\rangle$ , the other a photon in state  $|\sigma^-\rangle$ . The relative phase between the two emission paths, given by that of the initial superposition, in turn determines the phase between the photon's  $|\sigma^+\rangle$  and  $|\sigma^-\rangle$  component. In contrast to the  $\Lambda$  scheme, the temporal shape of the photonic wave packet remains unaffected by this type of interference. Instead, as will be shown below, the photonic phase becomes visible by an appropriate projective measurement.

In our setup, the phase of the initially prepared  $D_{5/2}$  superposition is not constant in time; since we apply a static magnetic field at the ion's position, the two  $D_{5/2}$  Zeeman states are non-degenerate, and the phase of their superposition evolves at the corresponding Larmor frequency. Hence the phase of interference evolves at the Larmor frequency as well. For the  $\Lambda$  scheme, this results in a temporal modulation of the population of the  $P_{3/2}$  state, and hence of the photon-scattering rate (quantum beat). For the  $V$  scheme, it is the phase between the photon's  $|\sigma^+\rangle$  and  $|\sigma^-\rangle$  component that evolves at the Larmor frequency.

### 3.2.2 Experimental realization

Our experimental setup for atom-to-photon phase mapping is shown in fig. 3.7; following optical ground-state pumping into one of the  $S_{1/2}$  Zeeman states, the  $D_{5/2}$  superposition is created through two consecutive pulses at 729 nm. Then a linearly polarized pulse at 854 nm generates the single Raman photon on the  $S_{1/2}$ - $P_{3/2}$  transition. The photons are collected through one of the HALOs, oriented perpendicularly to the quantization axis. A polarizer allows us to project the light onto a specific polarization. For the  $\Lambda$  scheme,

### 3.2. Atom-to-photon phase mapping

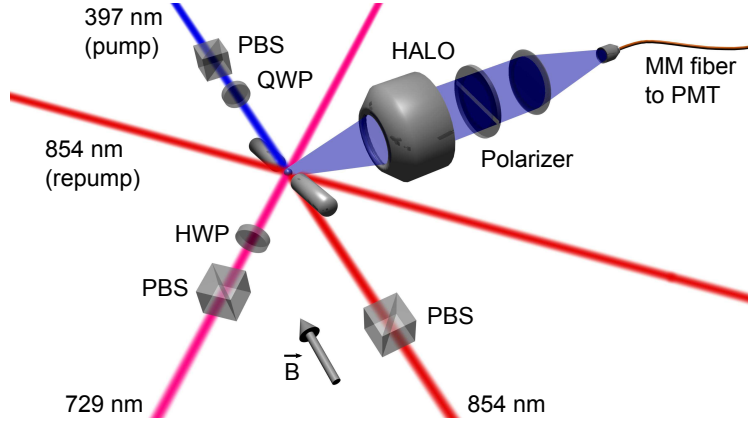


**Fig. 3.7:** Experimental setup for atom-to-photon phase mapping.  $\vec{B}$ : magnetic-field direction, HWP: half-wave plate, QWP: quarter-wave plate, PBS: polarizing beam-splitter cube, MM fiber: multi-mode optical fiber, PMT: photomultiplier tube. For clarity, the cooling beams at 397 nm and 866 nm are not shown.

the transmitted polarization is chosen parallel to the quantization axis in order to select photons scattered on the  $\pi$  transition only. For the V scheme, on the other hand, we rotate the polarizer by  $90^\circ$  in order to select photons scattered on the two  $\sigma$  transitions. At the same time, this projects the two  $|\sigma\rangle$  components onto the same linear polarization, which is a prerequisite for their interference.

#### 3.2.3 Results

The results for the realization of the  $\Lambda$  scheme are presented in fig. 3.8(a) in the form of arrival-time histograms. The photonic wave packets exhibit quantum beats, as expected from the theoretical considerations above. The beat period  $T$  is related to the energetic splitting of the  $|D_{5/2}, m = -3/2\rangle$  and  $|D_{5/2}, m = +1/2\rangle$  state and hence the magnetic-field strength ( $B = 2.79$  G) through

$$T = \frac{h}{2.4 \mu_B B} = 106 \text{ ns.} \quad (3.29)$$

The blue and red data points in fig. 3.8(a) reflect the temporal shape of the photonic wave packet for two  $D_{5/2}$  superposition states whose phases<sup>2</sup> are set to differ by  $\pi$ . In order to interpret the experimental data, we use a fit based on a numerical 18-level Bloch-equation model which fully describes the dynamics of the ion's electronic degree of freedom [158]. One of the fit parameters is the relative phase between the two quantum beats, which is found to be  $\phi = 1.006(3) \pi$ . As expected, this value is very close to the preset value of  $\pi$ .

Just as for the  $\Lambda$  scheme, the implementation of the V scheme shows quantum beats in the photon arrival-time histograms (see fig. 3.8(b)). As touched on in the theoretical

<sup>2</sup>The phase of the  $D_{5/2}$  superposition is set through the direct digital synthesizer that drives the acousto-optic modulator of the 729 nm beam.

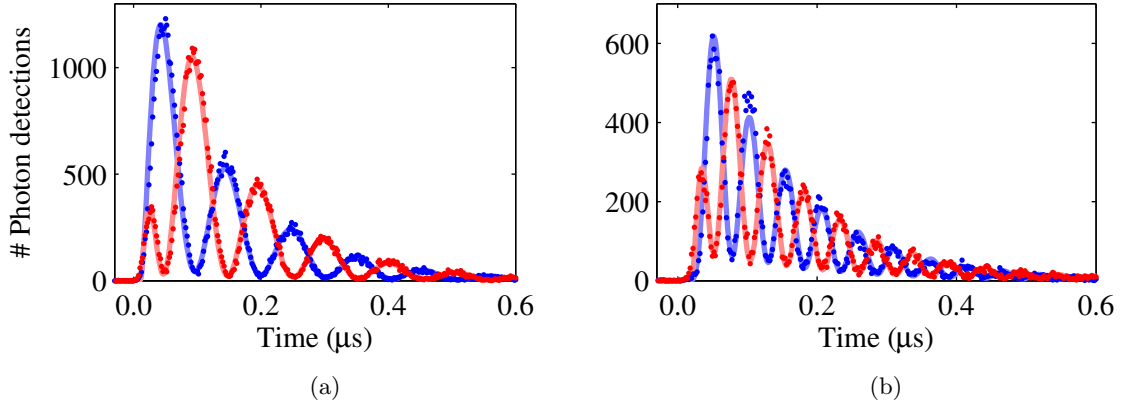


**Fig. 3.8:** Arrival-time histograms of single Raman photons at 393 nm wavelength in atom-to-photon phase mapping. Shown are quantum beats for two  $D_{5/2}$  superposition states with their phases differing by  $\pi$ . (a)  $\Lambda$  scheme (b)  $V$  scheme. For both schemes, the bin size is 2 ns and the measurement time per histogram is 6 min.

section, the photonic wave packet itself shows no temporal modulation since the quantum interference takes place between the  $\sigma^+$  and  $\sigma^-$  emission channel. The relative phase of the photon's two  $\sigma$  components has no influence on the rate at which the photon is generated but on its spatial emission pattern. In contrast to the  $\Lambda$  scheme, the emission pattern rotates about the quantization axis at the Larmor frequency of the initial  $D_{5/2}$  superposition state. Since we collect light from the ion along an axis perpendicular to the quantization axis, the spatial rotation is converted into a temporal modulation. Since the energetic splitting of the  $D_{5/2}$  superposition is twice as much as for the  $\Lambda$  scheme, the beat period is halved to  $T = 53$  ns. Again, the blue and red data points in fig. 3.8(b) represent Raman photons for  $D_{5/2}$  superposition states with phases differing by  $\pi$ . The fit of the theoretical model yields the relative phase  $\phi = 1.008(6)\pi$ , well in accordance with the expected value of  $\pi$ .

### Summary

In conclusion, I have presented a first step toward mapping the quantum state of a single ion onto a single Raman photon. Making use of two distinct quantum-interference schemes, we succeeded in transferring the phase information of an atomic superposition state onto the photonic state, visible as a quantum beat in the photon's temporal shape. The first scheme relies on the interference of absorption paths of the driving laser, resulting in a temporal modulation of the photonic wave packet. The second scheme, on the other hand, is based on the interference of emission paths of the single photon and yields a temporal modulation of the photon's spatial pattern. Both approaches, however, allowed us to faithfully map the phase encoded in the superposition state onto the photon.

## Chapter 4

# Quantum-networking experiments

A basic prerequisite for atom-based quantum networks [21, 61, 68, 144] are atom-photon interconnects that serve as bidirectional interfaces between flying qubits (photons) and network nodes (atoms) [159, 160]. They allow mapping quantum information between atoms and photons in a reversible manner [150] and establishing entanglement across the network [62, 64].

Chapters 2 and 3 discussed experimental methods and techniques that facilitate atom-photon interfaces by means of coherent control over the ion's quantum state (optical and radio-frequency qubits) and efficient light-matter coupling by virtue of our high-NA laser objectives (HALOs, see section 1.2.2). With these tools at hand, we are ready for proof-of-principle experiments that realize basic quantum-networking functionalities like photon-to-atom quantum-state transfer and atom-photon entanglement. In the first part of this chapter, I will present an experimental protocol for mapping the polarization state of a single photon onto the spin state of a single ion. A modification of this protocol then allows for the realization of atom-photon entanglement, presented in the second part of the chapter.

### 4.1 Protocol for photon-to-atom quantum-state transfer

A quantum-network scenario that employs single atoms (or ions) as network nodes requires the atoms to function as both senders and receivers of quantum information. However, the efficiencies associated with mapping quantum information from a photon onto an atom are limited by the inability to fulfill time-reversal symmetry [67, 161, 162, 163]; in principle, a photon emitted by a sender atom is absorbed with unity probability by a receiver atom if the absorption process is made the time reversal of the emission process. This includes both the spatial and temporal behavior of the emission. While the single photon can be temporally shaped through appropriate excitation in order to account for the temporal aspect [68], the spatial aspect is experimentally much more challenging. In free space, the photonic wave packet emitted by the sender atom possesses a certain spatial pattern (typically a dipole emission pattern), which would have to be reproduced at the position of the receiver atom. In other words, a large spatial overlap between the photonic mode and

the atomic absorption profile is desired. Promising approaches are found in high-aperture objective [83, 84] or deep parabolic mirrors [86, 87] that subtend a very large fraction of the atom's solid angle. An alternative lies in optical cavities [81, 91, 68] that strongly modify the mode structure of the electromagnetic field and thus allow for enhanced atom-light coupling. However, none of these schemes come close to unity absorption probability.

The true problem of non-unity efficiencies, however, lies not in a lower net rate at which quantum information is transmitted across the network but in seriously degrading the fidelity of the transferred quantum state. Since one cannot simply measure the quantum state of the receiver atom in order to determine if the state transfer has succeeded, the atomic state cannot be used reliably for further quantum information processing. We plan to overcome this issue by a scheme that makes the fidelity of the atomic quantum state independent of the transfer efficiency through an appropriate *heralding signal*. Very much in analogy to remote atom-atom entanglement [62, 164, 64, 65, 66], where the detection of two photons heralds entanglement between the atoms, schemes for the heralded transfer of a photonic polarization qubit onto the spin state of a single atom have been proposed [71, 72, 73]. The detection of a Raman-scattered photon heralds a successful absorption event and makes the transfer fidelity independent of its efficiency. In our previous works, the absorption of a single photon by the ion was signaled through a fluorescence signal [165, 166, 155], which, however, did not preserve the stored quantum state. In this section, I present a proof-of-principle experiment in order to demonstrate our protocol for heralded photon-to-atom quantum-state transfer. The results of this experiment have been published in [90].

#### 4.1.1 Quantum-state transfer scheme

Our protocol for heralded photon-to-atom quantum-state transfer allows us to map the polarization state of a photon absorbed on the  $D_{5/2}$ - $P_{3/2}$  transition onto the  $S_{1/2}$  Zeeman qubit. The experimental scheme, illustrated in fig. 4.1, starts with preparing the ion for absorption: optical pumping initializes the ion in the state  $|S_{1/2}, m = -1/2\rangle$ . Then a radio-frequency (RF) pulse resonant with the Zeeman-qubit transition prepares a symmetric superposition of the qubit states  $|+1/2\rangle$  and  $|-1/2\rangle$ . The RF source is thus the oscillator to which any superposition state must be referenced. State preparation is completed through two phase-coherent pulses at 729 nm that transfer the state to a symmetric superposition of the states  $|D_{5/2}, m = +3/2\rangle$  and  $|D_{5/2}, m = -3/2\rangle$ .

Next, we send a resonant laser pulse at 854 nm wavelength onto the ion. For the demonstration of our protocol, this pulse contains much more than one photon in order to increase the probability for an absorption event. However, there is no fundamental issue in implementing the protocol with true single photons. The laser pulse co-propagates along the quantization axis and thus drives only  $\sigma^+$  and  $\sigma^-$  transitions in the atomic reference frame. Light of right-handed circular polarization<sup>1</sup> exclusively excites  $\sigma^+$  transitions, while left-handed circularly polarized light excites  $\sigma^-$  transitions only. Accordingly, any

---

<sup>1</sup>Within this thesis, circular polarization is defined as the sense of rotation of the electric field when viewing the field along the quantization axis (defined by the static magnetic field).

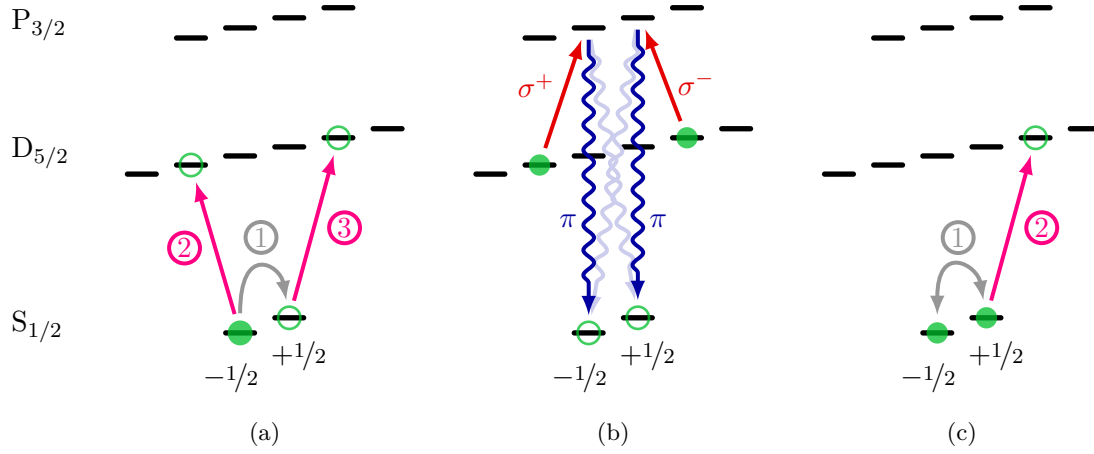


**Fig. 4.1:** Experimental scheme for photon-polarization storage. (a) Preparation of a superposition of the  $|D_{5/2}, m = \pm 3/2\rangle$  states by a sequence of a radio-frequency (RF) and two optical pulses. (b) Storage of the polarization state of a photon absorbed on the  $D_{5/2}$ - $P_{3/2}$  transition at 854 nm, heralded by a  $\pi$ -polarized photon at 393 nm. (c) Read-out of the atomic state through electron shelving. Depending on the desired measurement basis, another RF pulse is applied before.

superposition of the two circular polarizations (e.g. linearly polarized light) will drive the respective superposition of the two  $\sigma$  transitions. As given by the  $P_{3/2}$  branching fractions [156], the absorption of a photon transfers the ion back to the  $S_{1/2}$  state with 93.5% probability and releases a single Raman photon (heralding photon) at 393 nm. If we select for detection only photons emitted on the  $\pi$  transitions, then the superposition of  $\sigma^+$  and  $\sigma^-$  is mapped directly onto a corresponding superposition of the states  $|+1/2\rangle$  and  $|-1/2\rangle$  of the  $S_{1/2}$  ground state. In essence, the polarization state of the absorbed 854 nm photon has been mapped onto the ion's  $S_{1/2}$  Zeeman qubit, heralded by the detection of a single photon.

In the final step of the scheme, the atomic state is analyzed, conditioned on the detection of a heralding photon in state  $|\pi\rangle$ , in order to characterize the fidelity of our mapping protocol (state-mapping verification). This requires the atomic qubit to be projected onto different measurement bases. For a projection onto the  $\sigma_z$  basis<sup>2</sup>, formed by the energy eigenstates  $|+1/2\rangle$  and  $|-1/2\rangle$ , we apply another pulse at 729 nm that transfers (shelves) any population in state  $|+1/2\rangle$  to one of the  $D_{5/2}$  states. Subsequent atomic-state detection (switching on the cooling lasers and collecting atomic fluorescence) then allows us to discriminate between the two states with very high fidelity. However, in order to project the atomic state onto the superposition basis  $\sigma_\phi = \cos(\phi)\sigma_x - \sin(\phi)\sigma_y$ , another RF pulse prior to the shelving pulse effects a basis rotation. As we will see later, the phase  $\phi$  is determined by the detection time of the heralding photon.

<sup>2</sup>The operators  $\sigma_x$ ,  $\sigma_y$  and  $\sigma_z$  denote the Pauli matrices.

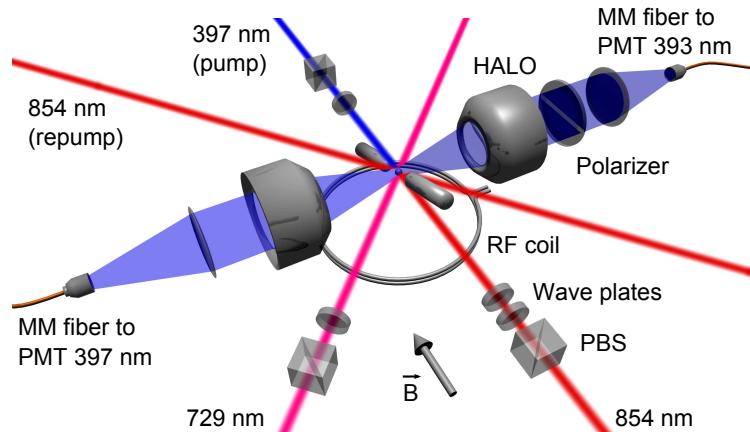


**Fig. 4.2:** Experimental setup for photon-to-atom quantum-state transfer.  $\vec{B}$ : magnetic-field direction, Wave plates: one half-wave and one quarter-wave plate, PBS: polarizing beam-splitter cube, MM fiber: multi-mode optical fiber, PMT: photomultiplier tube. For clarity, the cooling beams at 397 nm and 866 nm are not shown.

#### 4.1.2 Experimental realization

For this protocol, we make use of almost all tools and techniques presented in chapters 2 and 3. Our experimental setup is shown in fig. 4.2.

##### Light collection

We use both HALOs for the collection of blue light from the ion. One of them collects single photons at 393 nm, which are polarization-filtered by means of a polarizer. Transmitting only light polarized parallel to the quantization axis (given by the magnetic-field direction) selects only photons emitted on  $\pi$  transitions. The light is then coupled to a multi-mode optical fiber and detected by a photomultiplier tube (PMT). The detector output pulses are fed into the sequence-control unit (Hydra) and in addition time-tagged and stored for later analysis. At the same time, fluorescence light at 397 nm is collected by the second HALO, coupled to a multi-mode optical fiber and detected by another PMT. Its output pulses are fed into the sequence-control unit for atomic-state detection.

##### Input polarization state

The laser beam at 854 nm whose polarization is to be mapped onto the atomic quantum state is sent onto the ion along the quantization axis. Following a polarizing beam-splitter cube used to clean the light's polarization, a combination of a half-wave and a quarter-wave plate sets the polarization to any desired value. Using different input polarizations and analyzing the resulting atomic state will allow us to characterize the fidelity of the mapping process. Performing independent spectroscopy on the  $D_{5/2}-P_{3/2}$  transition (see section 2.4.2) allows for setting the laser frequency to the line center of the transition. This yields equal detunings from the two  $\sigma$  transitions that are to be excited, which is

#### 4.1. Protocol for photon-to-atom quantum-state transfer

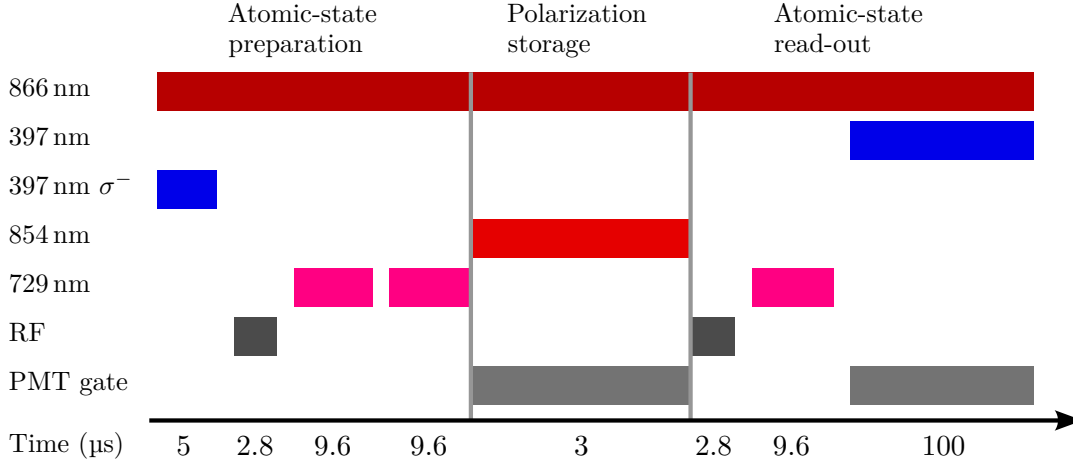


**Fig. 4.3:** Timing chart of the experimental sequence for photon-to-atom quantum-state transfer. Atomic-state read-out is performed only if the Raman photon has been detected. The RF pulse during state read-out is applied only if a rotation of the measurement basis is desired. Not shown: Doppler cooling at the end of the sequence.

crucial for avoiding any imbalance in the absorption probabilities on the two transitions that does not stem from the laser polarization.

#### Quantum-state manipulation

A circularly polarized beam at 397 nm, propagating antiparallel to the quantization axis, facilitates ground-state pumping (see section 2.3.1). For coherent manipulations on the  $S_{1/2}$ – $D_{5/2}$  transition, we make use of our narrow-band laser at 729 nm wavelength (see section 2.1.1). We also coherently control the  $S_{1/2}$  Zeeman qubit by means of our RF coil, placed below the vacuum chamber (see section 2.2.2). For a magnetic field of strength  $B = 2.8$  G, the atomic transition frequency is found at 7.8 MHz. An additional beam at 854 nm serves for repumping from  $D_{5/2}$  to the ground state. All laser beams are focused onto the ion from collimated beams through simple plano-convex lenses. The focal-spot diameters are  $\sim 60$   $\mu\text{m}$  (397 nm pump beam), 80  $\mu\text{m}$  (729 nm), 250  $\mu\text{m}$  (854 nm) and 125  $\mu\text{m}$  (854 nm repump beam).

#### Experimental sequence

The experimental sequence, depicted in fig. 4.3, starts with a 5  $\mu\text{s}$  long pump pulse at 397 nm that initializes the atomic qubit in the state  $|S_{1/2}, m = -1/2\rangle$  with 99.82(1) % probability, followed by a resonant RF pulse of 2.8  $\mu\text{s}$ , corresponding to a  $\frac{\pi}{2}$  pulse area<sup>3</sup>, that creates the  $S_{1/2}$  qubit in the symmetric superposition state. The subsequent pulses at 729 nm of pulse area  $\pi$  transfer the  $|S_{1/2}, m = \pm 1/2\rangle$  state to  $|D_{5/2}, m = \pm 3/2\rangle$ . The duration of these pulses is chosen rather long, 9.6  $\mu\text{s}$  each, in order to avoid off-resonant excitations of transitions to other  $D_{5/2}$  Zeeman states. After completing state preparation,

<sup>3</sup>The area of a pulse of Rabi frequency  $\Omega(t)$  is defined as  $A := \int \Omega(t) dt$ .

the 854 nm beam whose polarization is to be stored in the atomic qubit is switched on for 3  $\mu$ s. An optical power of 12  $\mu$ W yields  $\sim 9$  MHz Rabi frequency. Returning to the  $S_{1/2}$  state, the ion emits a single Raman photon at 393 nm wavelength. If the photon is detected, we perform atomic-state analysis; for a projection onto the superposition basis  $\sigma_\phi$ , another  $\frac{\pi}{2}$  RF pulse which effects the basis rotation is applied first. Then a pulse at 729 nm, again of 9.6  $\mu$ s duration, shelves any population in the state  $|S_{1/2}, m = +1/2\rangle$  to  $|D_{5/2}, m = +3/2\rangle$ , before we switch on the cooling lasers. A projection onto  $S_{1/2}$  causes the ion to emit fluorescence light which we detect at a rate of  $107 \cdot 10^3 \text{ s}^{-1}$ . On the other hand, a projection onto  $D_{5/2}$  leaves the ion dark and we detect PMT events from detector dark counts and laser stray light at  $60 \text{ s}^{-1}$ . For 100  $\mu$ s integration period, we can discriminate between the states  $S_{1/2}$  and  $D_{5/2}$  with 99.986 % fidelity (see section 2.1.3). If the heralding photon is not detected, as in most cases, the ion is Doppler cooled for 10  $\mu$ s. Including delays in the sequence-control unit, we attain 18 kHz repetition rate.

### 4.1.3 State transfer in circular polarization basis

In a first experiment, we would like to investigate how the state of circularly polarized light is mapped onto the atomic qubit. To this end, we choose the 854 nm light to be right-handed circularly polarized. In the atomic reference frame, this excites only the state  $|D_{5/2}, m = -3/2\rangle$  on the  $\sigma^+$  transition, but ideally leaves the population in  $|D_{5/2}, m = +3/2\rangle$  untouched. The detection of a Raman photon in state  $|\pi\rangle$  then heralds the projection of the ion onto the  $|-1/2\rangle$  ground state. Upon the detection of the heralding photon, we analyze the atomic state in the  $\sigma_z$  basis<sup>4</sup>. According to the measurement outcome (projection onto  $|+1/2\rangle$  or  $|-1/2\rangle$ ), the photon is sorted into one of two arrival-time histograms, shown in fig. 4.4(a). As expected, almost all photon-detection events are followed by projecting the atomic state onto  $|-1/2\rangle$ . In order to quantify the fidelity of the atomic state with respect to the ideally expected state, we need to compare the number of events in the two histograms. For this, however, we need to define a time window from which detection events are selected. If we choose this window too long, the number of dark-count events increases faster than the number of true photon detections. This degrades the fidelity of the atomic state since the ion is projected onto the desired state by the detection of a heralding photon only. On the other hand, if we choose the time window too short, the effective detection efficiency decreases and the mapping protocol becomes inefficient. As a reasonable trade-off between the two effects, we choose a window of 450 ns length, which corresponds to  $\sim 90$  % of the photonic distribution. The ratio of the numbers of events in the conditional arrival-time histograms then yields 97.8(1) % probability to find the ion in state  $|-1/2\rangle$ , which represents also the fidelity of the measured atomic state with respect to  $|-1/2\rangle$ . Analogously, we repeat the measurement with left-handed circularly polarized light at 854 nm, arriving at 96.4(3) % fidelity with respect to state  $|+1/2\rangle$ . We explain the difference between the two fidelity values by the difficulty in adjusting the two circular polarizations sufficiently well.

<sup>4</sup>The measured probability for a projection onto the state  $|+1/2\rangle$  is corrected for the shelving efficiency  $p_{\text{shelving}} = 99.1(3)$  %.

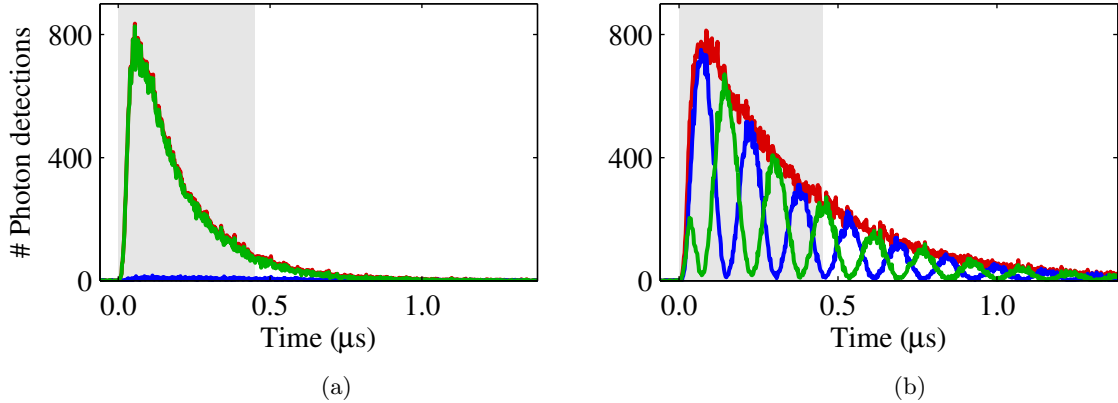


**Fig. 4.4:** Conditional arrival-time histograms of single 393 nm photons. Blue curve: ion in state  $|+1/2\rangle$ , green curve: ion in state  $|-1/2\rangle$ , red curve: unconditional arrival-time distribution (sum of the conditional histograms). (a) Projection onto the  $\sigma_z$  basis for right-handed circularly polarized 854 nm light. (b) Projection onto the  $\sigma_\phi$  basis for linearly (vertically) polarized 854 nm light. The shaded areas represent the time window used for data analysis. For each graph, the bin size is 2 ns and the measurement time is 20 min.

#### 4.1.4 State transfer of linear polarization

In a second step, we investigate our mapping protocol for the case of linearly polarized light at 854 nm. As explained above, this should drive the two  $\sigma$  transitions with equal amplitude and a relative phase that is given by the angle of the linear polarization. The latter is defined with respect to the plane spanned by the axis of fluorescence collection and the quantization axis, which coincides with the plane of the optical table. Exemplarily, we choose the light to be vertically polarized, i.e. polarized perpendicularly to aforementioned plane. The detection of a Raman photon in state  $|\pi\rangle$  then heralds the projection of the atomic qubit onto a symmetric superposition of  $|+1/2\rangle$  and  $|-1/2\rangle$ . Conditioned on the photon detection, we analyze the qubit in the superposition basis  $\sigma_\phi$  in order to characterize the amplitudes and phase of the superposition state. As explained in section 4.1.1, this is done through a basis rotation, realized by another RF pulse prior to electron shelving. As we did for circularly polarized 854 nm light, we sort the photon-detection events into histograms for a projection onto state  $|+1/2\rangle$  and  $|-1/2\rangle$ , respectively, after the basis rotation. From fig. 4.4(b), we observe oscillations in the conditional arrival-time distributions that resemble very much the quantum beats described in section 3.2. In fact, they stem from the same physical origin; the phase of the initially prepared superposition of  $|D_{5/2}, m = \pm 3/2\rangle$  evolves at the Larmor frequency given by the energetic splitting of the two Zeeman states. Detecting the heralding photon projects the initial superposition onto the final superposition of  $|S_{1/2}, m = \pm 1/2\rangle$ , whose phase now evolves at the Larmor frequency given by the  $S_{1/2}$  Zeeman splitting. The  $D_{5/2}$  splitting is larger than the  $S_{1/2}$  splitting; therefore, the longer the ion remains in the  $D_{5/2}$  superposition, the larger the phase it accumulates before being projected onto the  $S_{1/2}$  superposition. More precisely, the rate at which the phase accumulates is given by the difference of the two Larmor

frequencies. The probability to project the final atomic state onto a given superposition state hence oscillates at the difference frequency. Taking into account the Landé factors, the oscillation period (the *effective* Larmor period) which is seen in fig. 4.4(b) is found to be

$$T = \frac{h}{1.6 \mu_B B} = 160 \text{ ns} \quad (4.1)$$

for our static magnetic field  $B = 2.8 \text{ G}$ . Another way of viewing the accumulated phase is to consider the measurement basis time-dependent; the time  $t$  of a photon detection determines the phase  $\phi$  of the observable  $\sigma_\phi = \cos(\phi) \sigma_x - \sin(\phi) \sigma_y$  through

$$\phi = 2\pi \frac{t \bmod T}{T}. \quad (4.2)$$

Future implementations of our mapping protocol that employ true single photons for absorption will need to take the detection time of the heralding photon into account in order to compensate for the additional atomic phase. If this phase information is discarded, the  $S_{1/2}$  superposition must be considered decohered. For the characterization of our protocol, however, the effect is advantageous; since the phase of the measurement basis is chosen randomly by the photon detection, we do not need three sets of measurements ( $\sigma_x, \sigma_y, \sigma_z$ ) but only two ( $\sigma_\phi, \sigma_z$ ) in order to perform full quantum-state tomography of the atomic state.

### Indistinguishability of 393 nm photons

As seen in fig. 4.4, the photon wave packet is approximately twice as long when the ion is excited with linearly polarized light as when excited with circular polarization since the relative overlap of linearly polarized light with  $\sigma$  transitions is only  $\frac{1}{\sqrt{2}}$ . This results in lower excitation rates and thus longer wave packets (cf. section 3.1.1). At this point, one might think that the detection time of a heralding photon yields information about the polarization state mapped onto the ion (which would be perceived as decoherence). For example, the later the photon is detected, the more likely the polarization was linear, not circular. This is true, however, only for an excitation with a laser pulse that provides a large number of photons in a single mapping attempt. For future implementations of the protocol that use single photons, the relevant quantity is the height of the initial peak in the arrival-time distributions, which is the same for the two polarizations; the subsequent shape of the distributions only reflects the temporal evolution of the  $D_{5/2}$  state due to the laser excitation.

On a different matter, it is interesting to note that the two  $\pi$  channels of the  $S_{1/2}^- - P_{3/2}$  transition yield photons that are distinguishable in frequency due to the Zeeman splitting. In principle, this implies leakage of quantum information from the ion regarding its  $S_{1/2}$  qubit state, causing the qubit to decohere. However, we resolve the photons not spectrally, but temporally; with a timing uncertainty of  $\sim 300 \text{ ps}$  (given by the PMT transit-time spread), which is small compared with the effective Larmor period  $T = 160 \text{ ns}$ , the frequency information is erased and coherence is preserved. This *quantum-eraser* [167, 168, 169] point of view is simply another way of accounting for the atomic phase acquired through Larmor precession.

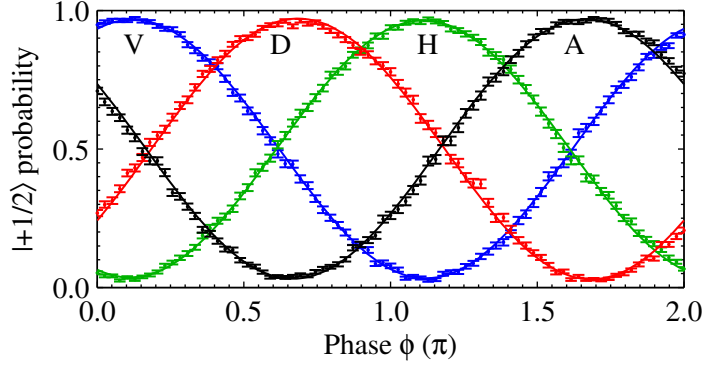


**Fig. 4.5:** Atomic-phase histograms. Shown is the probability to project the ion onto state  $|+1/2\rangle$  after the basis rotation as a function of the atomic phase  $\phi$  for the 854 nm light polarizations vertical (V), horizontal (H), diagonal (D) and antidiagonal (A). The solid lines are sinusoidal fits ( $\chi^2 \approx 2$ ).

### Atomic-phase histograms

In order to properly characterize the quality of the atomic superposition created by excitation with linearly polarized light, we need to quantify visibility and phase of the oscillations in the photon arrival-time distributions. We do this by means of an atomic-phase histogram; each detected heralding photon is assigned the value of the phase  $\phi$  left on the atomic superposition. These phase values are then sorted into two intermediate histograms, according to the outcome of the measurement in the superposition basis. From these two histograms, the probability to project the ion onto the state  $|+1/2\rangle$  after the basis rotation as a function of the atomic phase  $\phi$  is derived. Fig. 4.5 displays such atomic-phase histograms for four distinct linear polarizations of the 854 nm light. As expected, the fringes exhibit consecutive relative phase shifts of  $\frac{\pi}{2}$  going from V to D, H and A polarized light. We attribute deviations from  $\frac{\pi}{2}$  to the difficulty in adjusting the angle of the linear polarization sufficiently well. From sinusoidal fits, we infer visibility  $V$  and phase  $\phi$  of the atomic-phase histograms. Since we consider deviations between the measured and expected phase values not to result from the mapping process itself, only the fringe visibility enters into the fidelity of the atomic state<sup>5</sup>. For the polarizations V, H, D and A, we obtain the fidelities 96.7(1) %, 96.4(1) %, 97.0(2) % and 96.9(2) %, respectively.

Including the fidelities measured for circularly polarized 854 nm light, we arrive at 96.9(1) % fidelity averaged over the six input polarization states.

<sup>5</sup>The visibility  $V$  of the fringes amounts to the length of the projection of the ion's Bloch vector onto the plane of superposition states. If the ion is in an ideal superposition state (fidelity  $F = 1$ ), we thus find  $V = 1$ . In contrast, the states  $|+1/2\rangle$ ,  $| -1/2\rangle$  and any statistical mixture of the two possess fidelity  $F = 0.5$  and yield  $V = 0$ . In general, fidelity and visibility are related through  $F = \frac{1}{2}(1 + V)$ .

### 4.1.5 Quantum-process tomography

In addition to the average quantum-state fidelity quoted above, another way of assessing the quality of our mapping protocol is to perform quantum-process tomography [1]. This procedure describes the mapping protocol as a quantum process and allows us to fully characterize how an arbitrary polarization state (input state) is mapped onto the atomic qubit (output state). This section briefly summarizes the notion of quantum-process tomography; a more detailed treatment is found, for example, in [170].

A quantum process is described by a completely positive map  $\varepsilon$  that maps an input state  $\rho$  onto an output state  $\varepsilon(\rho)$ . In the case of a single qubit, this superoperator can be written in the *operator-sum representation* [171],

$$\varepsilon(\rho) = \sum_{i=1}^4 A_i \rho A_i^\dagger, \quad (4.3)$$

in which the so-called Kraus operators  $A_i$  fully characterize the quantum process. Knowledge of the Kraus operators, however, usually does not provide much physical insight into the quantum process. Instead, the map  $\varepsilon$  can also be expressed in terms of an orthonormal basis for the vector space of operators acting on the single-qubit Hilbert space. In particular, the Pauli operators  $\{\sigma_{i=1,\dots,4}\} = \{\mathbb{1}, \sigma_x, \sigma_y, \sigma_z\}$  (extended by the identity operator) form such a basis and are directly associated with physical processes such as unitary operations, projective measurements and decoherence. The quantum process then takes the form

$$\varepsilon(\rho) = \sum_{m,n=1}^4 \chi_{mn} \sigma_m \rho \sigma_n, \quad (4.4)$$

and the coefficient matrix  $\chi$  is called the *process matrix*. Its identity part,  $\chi_{11}$ , is termed the *process fidelity* and is our figure of merit besides the average quantum-state fidelity. It is computed using four input states which are mutually linearly independent and the respective output states. As input states, we choose the polarizations R, L, V and D. For each input state, we perform full tomography of the atomic quantum state by projections onto both the  $\sigma_\phi$  and  $\sigma_z$  basis. From this and by the method described in [170], we reconstruct the process matrix, depicted in fig. 4.6(a), and obtain the process fidelity  $|\chi_{11}| = 95.0(2)\%$ .

### 4.1.6 State-transfer fidelity vs. heralding probability

Besides quantum-state and quantum-process fidelity, a crucial point in our mapping protocol is the *heralding probability*, i.e. the probability to detect the Raman photon that heralds a successful photon-to-atom quantum-state transfer. For a detection time window of 450 ns, we achieve 0.438(1)% average heralding probability for the six input polarization states discussed above. It is instructive, however, to analyze this efficiency value as well as the transfer fidelities for different choices of the detection time window. Fig. 4.6(b) illustrates the interplay of efficiency and fidelity of our protocol; for short time windows and thus small heralding probabilities, both the quantum-process and average quantum-state

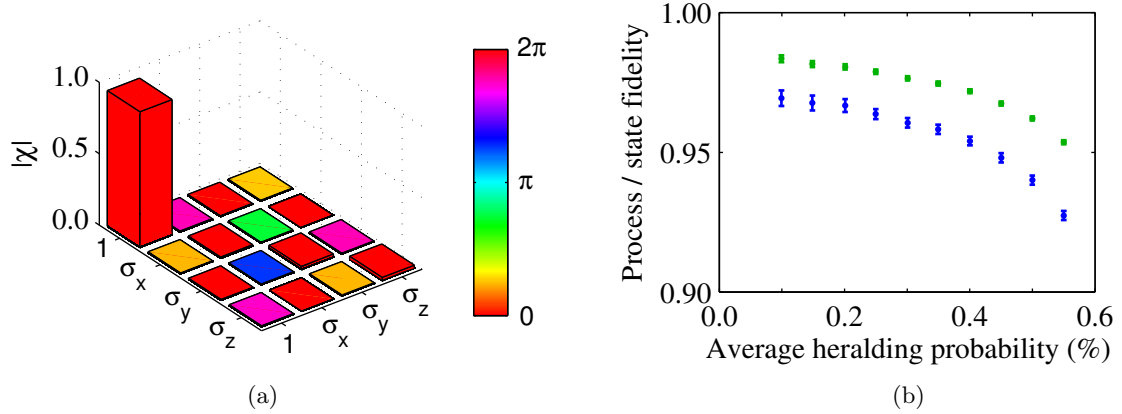


**Fig. 4.6:** (a) Quantum-process matrix characterizing the mapping protocol. Shown are the moduli of the matrix entries; the colors represent the entries' complex arguments. (b) Process fidelity (blue dots) and average quantum-state fidelity (green dots) for different heralding probabilities, determined by the length of the detection time window.

fidelity reach values close to unity. On the other hand, if we cut back on fidelity, we can reach heralding probabilities above 0.5 %.

#### 4.1.7 Error sources

The fidelity of our mapping protocol is mainly limited by two effects: first, detector dark counts mimic the detection of true photons at 393 nm (1.7 % within 450 ns). If the ion emits a Raman photon and is transferred to the ground state but a dark-count event is detected instead, the atomic-phase information is lost and the qubit state decoheres entirely. For linearly polarized light at 854 nm, this corresponds to a statistical mixture of  $|+1/2\rangle$  and  $|-1/2\rangle$  (fidelity  $F = 0.5$ ). For circularly polarized light, however, the ion is transferred to the corresponding Zeeman state (for which no relative phase exists) and we still obtain a high fidelity.

A second source of error lies in spontaneous decay from the  $P_{3/2}$  state back to  $D_{5/2}$ . The emission of an undetected (parasitic) photon at 854 nm leaves the ion in a statistical mixture from which it is once more excited by the driving laser. Obviously, this will cause the  $S_{1/2}$  qubit to end up in a mixed state as well, thus degrading the transfer fidelity. The observed effect (1.4 %) is on the order of what is expected from the  $P_{3/2}$  branching fractions [156]. This limitation will not be relevant for mapping the polarization state of single photons at 854 nm since there will be no second photon available for a re-excitation from  $D_{5/2}$ . The emission of a parasitic photon will hence only reduce the efficiency of the protocol.

#### 4.1.8 Alternative schemes

Finally, I would like to mention that modified versions of our mapping protocol exist; ref. [73] discusses these in terms of efficiency and experimental complexity. We implemented

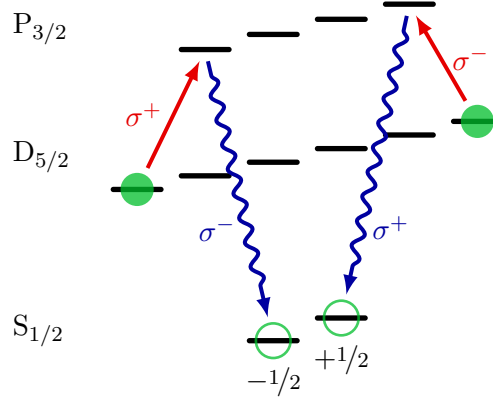


**Fig. 4.7:** Alternative scheme for heralded photon-to-atom quantum-state transfer (“ $\sigma$  scheme”). A successful mapping event is heralded by the detection of a Raman photon in a  $|\sigma\rangle$  state.

one of these alternative schemes, sketched in fig. 4.7; the initial atomic superposition is now created between the Zeeman states  $|D_{5/2}, m = +5/2\rangle$  and  $|D_{5/2}, m = -5/2\rangle$ . In contrast to the scheme presented above in which the absorption process is heralded by the detection of a Raman photon in state  $|\pi\rangle$  (“ $\pi$  scheme”), this scheme relies on the detection of a photon emitted on a  $|\sigma\rangle$  transition (“ $\sigma$  scheme”). The excitation of the state  $|D_{5/2}, m = +5/2\rangle$  yields a Raman photon in state  $|\sigma^+\rangle$ , while exciting state  $|D_{5/2}, m = -5/2\rangle$  produces a  $|\sigma^-\rangle$  photon. This implies, however, that the polarization of the heralding photon reveals the final state of the atomic qubit. We circumvent this by another quantum-eraser technique; by projecting the state of the heralding photon onto a superposition of  $|\sigma^+\rangle$  and  $|\sigma^-\rangle$ , the information about the photon’s polarization state is erased. We achieve this projective measurement by simply removing the polarizer that was used in the  $\pi$  scheme in order to select photons from  $\pi$  transitions only. Since we now observe light from the ion perpendicularly to the quantization axis, the two  $\sigma$  transitions become indistinguishable and are perceived as vertically polarized light.

Apart from the differing state preparation and the removed polarizer, the experimental implementation of the  $\sigma$  scheme follows exactly that of the  $\pi$  scheme. Using a set of input polarizations at 854 nm and performing quantum-state tomography allows us to determine the figures of merit: for a 450 ns detection time window, we find 91.7(5) % process fidelity, 94.8(2) % average state fidelity and 0.318(1) % heralding probability. The reduced fidelities as compared with the  $\pi$  scheme result, to the best of our knowledge, from the nonlinearly [172] higher susceptibility of the  $|D_{5/2}, m = \pm 5/2\rangle$  states to magnetic-field noise. While less relevant for the  $\pi$  scheme, this becomes important for the  $\sigma$  scheme already within the time it takes for state preparation ( $\sim 20 \mu\text{s}$ ). The reduced heralding probability is explained by the spatial emission pattern of  $\sigma$  which, in contrast to  $\pi$  transitions, is preferentially directed along the quantization axis. Both drawbacks of this scheme, however, will be mitigated in the future; the polarization-state transfer of single photons at 854 nm can only be realized by sending the photons onto the ion through one of the HALOs (otherwise,

the absorption probability will be too small). This means that the quantization axis (and hence the magnetic field) must be set along the HALO optical axis. Consequently, heralding photons at 393 nm would be collected along the quantization axis only, almost completely suppressing the detection of photons from  $|\pi\rangle$  transitions. In summary, the  $\pi$  scheme will not be feasible with single 854 nm photons with our experimental setup, but in terms of efficiency, the  $\sigma$  scheme provides an even better solution [73] once the active compensation of magnetic-field noise [137] is ready. The implications of magnetic-field noise on the feasibility of our protocol for single-photon absorptions will be discussed in the next section.

#### 4.1.9 Coherence-time considerations for single-photon realizations

In the demonstration of our mapping protocol, using laser pulses at 854 nm instead of single photons, most heralding photons at 393 nm were detected within 1  $\mu$ s after switching on the laser. In realizations employing single photons whose polarization state is to be mapped onto the ion, the average time for which the ion remains in the  $D_{5/2}$  superposition until it absorbs a single photon will be greater by many orders of magnitude. However, since magnetic-field fluctuations limit the coherence time of any atomic superposition state, we re-prepare the ion for absorption after a certain time even if no absorption has taken place. Otherwise, the atomic state decoheres and the mapping fidelity decreases. In order to achieve an appreciable duty cycle of the experimental sequence, it is hence imperative that the superposition remain coherent (with respect to the RF reference oscillator) for as long as possible [94].

From the Ramsey experiments presented in chapter 2 on both the 729 nm and the RF transition, we could in principle derive the expected coherence time of the  $D_{5/2}$  superposition in the case of the  $\sigma$  scheme. However, in the course of preparing the measurements presented in this chapter, we could significantly lower magnetic-field influences by repositioning some of our laboratory devices and their power cables. Consequently, it is advisable to examine the  $D_{5/2}$  superposition in terms of coherence time in an independent measurement: in analogy to the Ramsey experiments described before, we first prepare the  $|D_{5/2}, m = \pm 5/2\rangle$  superposition state through one RF pulse and two optical pulses at 729 nm. After a certain waiting time (Ramsey time), we map the  $D_{5/2}$  back to an  $S_{1/2}$  superposition through another two optical pulses. Ideally, this superposition equals that created by the initial  $\frac{\pi}{2}$  RF pulse (up to a fixed phase shift given by the relative phase of the optical pulses). Scanning the phase of a final  $\frac{\pi}{2}$  RF pulse, followed by electron shelving, allows us to infer the coherence properties and hence, by varying the Ramsey time, to determine the coherence time of the  $D_{5/2}$  superposition.

The results of the Ramsey measurement are displayed in fig. 4.8. Although the amplitudes of the fluctuating magnetic fields are significantly lower as compared with those from chapter 2, the much larger effective Landé factor  $g_{\text{eff}} = 6$  leads us to a coherence time in the range 200 – 400  $\mu$ s. Ideally, this value should be at least two orders of magnitude larger than the state-preparation time ( $\sim 20$   $\mu$ s) in order to attain a reasonable duty cycle. We are confident, however, that the active magnetic-field stabilization [137] that is currently being set up sufficiently prolongs the coherence time for duty cycles above 50 %.

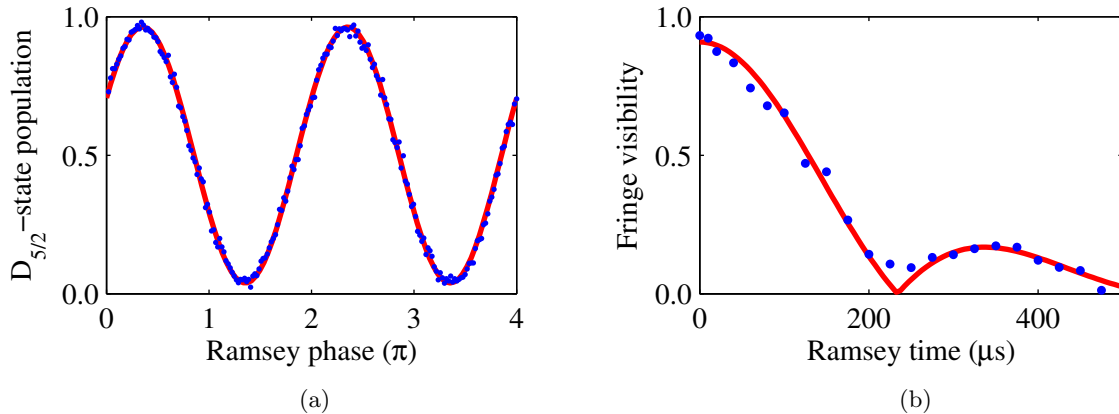


**Fig. 4.8:** (a) Ramsey experiment for the  $|D_{5/2}, m = \pm 5/2\rangle$  superposition state and  $10 \mu\text{s}$  Ramsey time. From the fit ( $\chi^2 = 1.3$ ), we obtain the fringe visibility  $V = 0.923(3)$ . (b) Fringe visibility as a function of Ramsey time. Fitting the theoretical model from eqn. 2.23 ( $\chi^2 = 36.5$ ) yields the white-noise contribution  $B_{\text{noise}} = 0.067(4)$  mG, the power-line contribution  $B_{\text{line}} = 0.195(4)$  mG and the qubit coherence times  $T_{2,\text{noise}}^* = 401(22)$   $\mu\text{s}$  and  $T_{2,\text{line}}^* = 170(3)$   $\mu\text{s}$ . Error bars are smaller than the size of symbols.

## Summary

We have experimentally demonstrated a protocol for heralded photon-to-atom quantum-state transfer. In future applications, it will allow mapping the polarization state of a single photon absorbed on the  $D_{5/2}$ – $P_{3/2}$  transition of  $^{40}\text{Ca}^+$  onto its  $S_{1/2}$  Zeeman qubit. An absorption event is heralded by a single Raman photon with  $\sim 0.4\%$  heralding probability, the detection time of the photon being crucial in keeping track of the atomic phase. The achievable fidelities of the mapping protocol were found to be  $> 95\%$ .

These results compare favorably with work from competing groups; in an experiment with single Cs atoms coupled to an optical cavity,  $\sim 73\%$  average quantum-state fidelity was achieved [81], while  $\sim 93\%$  fidelity was reached with a single Rb atom in a cavity [91]. In both cases, however, no signal for heralding a successful state transfer was available. Hence the transfer fidelity in a single experimental shot was limited by the photon-absorption probability, which was  $< 10\%$ . In contrast, a quantum memory based on single magnons in an atomic ensemble provided a herald in the shape of a Raman-scattered photon with  $\sim 10\%$  heralding probability (at  $\sim 90\%$  fidelity) [92]. Atomic ensembles, however, do not offer the prospect of local quantum-information processing.

## 4.2 Atom-photon entanglement

The creation of entanglement between flying and stationary qubits is an important resource in realizing a quantum network. In combination with mapping quantum states between the two kinds of qubits, it allows for establishing entanglement between spatially separated network nodes [62, 64, 65, 68, 66].

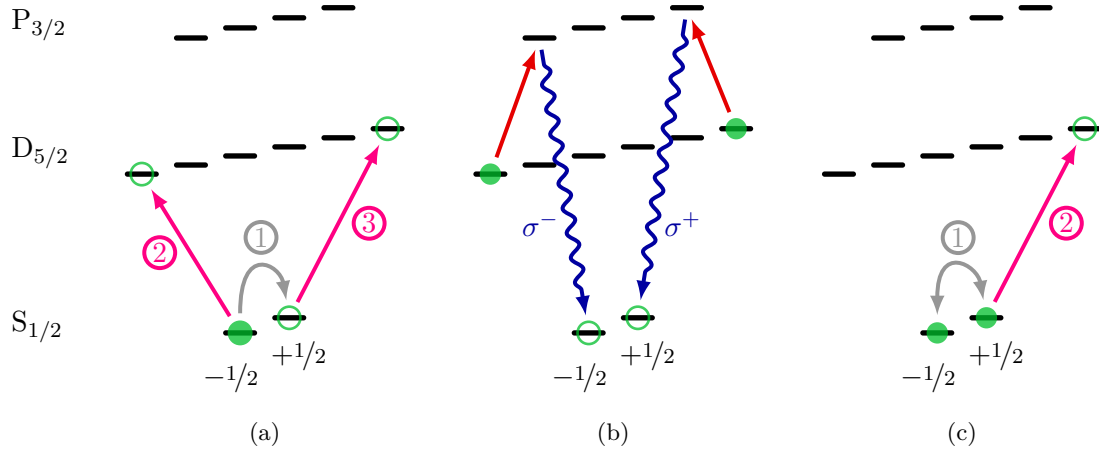


**Fig. 4.9:** Experimental scheme for atom-photon entanglement. (a) Preparation of a symmetric superposition of the  $|D_{5/2}, m = \pm 5/2\rangle$  states by a sequence of a radio-frequency (RF) and two optical pulses. (b) Generation of a single Raman photon, spin-entangled with the atomic  $S_{1/2}$  Zeeman qubit. (c) Read-out of the atomic state, after detection of the photonic state in a given polarization basis, through electron shelving. If desired, another RF pulse before shelving effects a basis rotation.

In the context of atom-based quantum networks, seminal work includes the entanglement of the polarization of a spontaneously scattered single photon with the spin state of a single ion [173] or neutral atom [151]. In both experiments, the generation of entanglement was based on Rayleigh scattering through pulsed laser excitation. More recently, tunable ion-photon entanglement by means of a cavity-mediated Raman transition was demonstrated [174].

In this part of the chapter, I present the generation and characterization of entanglement between the polarization state of a single spontaneous Raman photon and the spin state of a single ion.

#### 4.2.1 Scheme for atom-photon entanglement

Our experimental scheme for the creation of atom-photon entanglement is based on a modification of our “ $\sigma$  scheme” for heralded photon-to-atom quantum-state transfer, presented in the previous section. As shown in fig. 4.9, the scheme begins with state preparation: following optical ground-state pumping, a sequence of a radio-frequency (RF) and two optical pulses prepares a symmetric superposition of the Zeeman states  $|D_{5/2}, m = +5/2\rangle$  and  $|D_{5/2}, m = -5/2\rangle$ . Then a laser pulse excites the two Zeeman states on the  $D_{5/2}$ - $P_{3/2}$  transition at equal rates; the ion is transferred back to the  $S_{1/2}$  ground state, accompanied by the emission of a single Raman photon from the  $S_{1/2}$ - $P_{3/2}$  transition (at 393 nm wavelength). A photon in state  $|\sigma^+\rangle$  leaves the ion in the qubit state  $|+1/2\rangle$ , while a  $|\sigma^-\rangle$

photon results in the state  $|{-1/2}\rangle$ . Since the scattering process is mostly coherent<sup>6</sup>, the two decay channels interfere and yield the maximally entangled state

$$|\Psi_{\text{ion-photon}}\rangle = \frac{1}{\sqrt{2}} \left( |{+1/2}\rangle |\sigma^+\rangle + e^{i\theta} |{-1/2}\rangle |\sigma^-\rangle \right). \quad (4.5)$$

As described in more detail later, we observe the Raman photons parallel to the quantization axis; photons scattered on the  $|\sigma^+\rangle$  ( $|\sigma^-\rangle$ ) transition appear right-handed (left-handed) circularly polarized. Hence, changing from the atomic to the laboratory reference frame yields the state

$$|\Psi_{\text{ion-photon}}\rangle = \frac{1}{\sqrt{2}} \left( |{+1/2}\rangle |\text{R}\rangle + e^{i\theta} |{-1/2}\rangle |\text{L}\rangle \right). \quad (4.6)$$

In order to characterize this two-qubit state experimentally, we perform quantum-state tomography by analyzing the photon's polarization in a set of conjugate measurement bases. Upon detecting a photon, i.e. projecting it onto a specific polarization state, we analyze the atomic state as well. Like the photon, the ion's spin state is projected onto different measurement bases, using the same procedure as for our photon-to-atom state-transfer protocol (see section 4.1.1); in order to project the ion onto the  $\sigma_z$  basis, formed by the energy eigenstates  $|{+1/2}\rangle$  and  $|{-1/2}\rangle$ , we apply a pulse at 729 nm that transfers any population in state  $|{+1/2}\rangle$  to one of the  $\text{D}_{5/2}$  states. Subsequent atomic-state detection (switching on the cooling lasers and collecting atomic fluorescence) then discriminates between the two states with very high fidelity. On the other hand, in order to project the atomic state onto the superposition basis  $\sigma_\phi = \cos(\phi)\sigma_x - \sin(\phi)\sigma_y$  (with the phase  $\phi$  determined by the detection time of the Raman photon), another RF pulse prior to the shelving pulse effects a basis rotation.

### 4.2.2 Experimental realization

The experimental setup, shown in fig. 4.10, is only a slight modification of the one used for our protocol for heralded photon-to-atom quantum-state mapping (see section 4.1.2).

#### Light collection

We make use of both HALOs for the collection of blue light emitted by the ion. One of them collects single photons at 393 nm, whose polarization is analyzed by means of a half-wave and a quarter-wave plate and a polarizer. The quantization axis, defined by the static magnetic field, is chosen along the HALO optical axis, hence Raman photons from  $\sigma$  transitions appear as circularly polarized light. After being coupled to a multi-mode optical fiber, the light is detected by a photomultiplier tube (PMT). Its output pulses are fed into the sequence-control unit (Hydra) and furthermore time-tagged and stored for later analysis. At the same time, fluorescence light at 397 nm is collected by the second HALO and detected by another PMT, whose output pulses are fed into the sequence-control unit for atomic-state detection.

<sup>6</sup>Thanks to favorable branching fractions, population from the  $\text{P}_{3/2}$  state decays predominantly (with 93.5% probability [156]) to the ground state, making decoherence through decay back to  $\text{D}_{5/2}$  and subsequent re-excitation a comparably small effect.



### Experimental sequence

The experimental sequence starts with 60  $\mu\text{s}$  of optical pumping that initializes the ion in the state  $|S_{1/2}, m = -1/2\rangle$  with 99.83(1) % probability, followed by a resonant RF pulse of 2.6  $\mu\text{s}$  that creates the  $S_{1/2}$  qubit in the symmetric superposition state. The subsequent pulses at 729 nm of pulse area  $\pi$ , each 1.8  $\mu\text{s}$  long, transfer the  $|S_{1/2}, m = \pm 1/2\rangle$  state to  $|D_{5/2}, m = \pm 5/2\rangle$ . Following state preparation, the 854 nm photon-generation beam is switched on for 3  $\mu\text{s}$ . An optical power of 7  $\mu\text{W}$  yields  $\sim 7$  MHz Rabi frequency. As the ion returns to the  $S_{1/2}$  state, it emits a single Raman photon at 393 nm wavelength. In case the photon is detected, we perform atomic-state analysis; in order to project the ion onto the superposition basis  $\sigma_\phi$ , another  $\frac{\pi}{2}$  RF pulse effects a basis rotation. Then another pulse at 729 nm transfers any population in the state  $|S_{1/2}, m = +1/2\rangle$  to  $|D_{5/2}, m = +5/2\rangle$ , before we switch on the cooling lasers. Projecting it onto  $S_{1/2}$  causes the ion to emit fluorescence light which we detect at a rate of  $156 \cdot 10^3 \text{ s}^{-1}$ . On the other hand, projecting it onto  $D_{5/2}$  leaves the ion dark and we detect PMT events from detector dark counts and laser stray light at  $60 \text{ s}^{-1}$ . With 100  $\mu\text{s}$  integration period, we discriminate the states  $S_{1/2}$  and  $D_{5/2}$  with 99.9988 % fidelity (see section 2.1.3). If the heralding photon is not detected, as in most cases, the ion is Doppler cooled for 10  $\mu\text{s}$ . Including delays in our sequence-control unit, we attain 11 kHz repetition rate.

#### 4.2.3 Interlude: Quantum-state tomography

Before we can proceed with experimentally determining the joint atom-photon quantum state, we need to adapt the methods of quantum-state tomography [175, 176] to our problem. For a full reconstruction of the two-qubit state, we rely on the classic approach based on performing tomographically complete measurements [177] on the two-qubit Hilbert space. A common choice is the canonical set  $E$  of observables formed by tensor products of conjugate single-qubit measurement bases. Explicitly, this set contains all 16 tensor products of the Pauli operators  $\{\sigma_{i=1,\dots,4}\} = \{\mathbb{1}, \sigma_x, \sigma_y, \sigma_z\}$  acting on the individual qubits:

$$E = \{\sigma_i \otimes \sigma_j | i, j = 1, \dots, 4\} \quad (4.7)$$

For a given two-qubit density operator  $\rho$ , the expectation value for a particular measurement is

$$w_{i,j} := \langle \sigma_i \otimes \sigma_j \rangle = \text{tr}(\sigma_i \otimes \sigma_j \rho). \quad (4.8)$$

Since the set  $E$  of observables is tomographically complete, the set  $\{w_{i,j}\}$  of the 16 expectation values fully characterizes the quantum state  $\rho$ .  $E$  represents conjugate measurement bases, and hence  $\rho$  may be expressed directly as a linear combination of the tensor operators [175]:

$$\rho = \frac{1}{4} \sum_{i,j=1}^4 w_{i,j} \sigma_i \otimes \sigma_j \quad (4.9)$$

The expectation values  $w_{i,j}$  are determined experimentally from joint measurements on the two qubits, and from eqn. 4.9, the underlying quantum state  $\rho$  is reconstructed.

## 4.2. Atom-photon entanglement

---

In our experimental situation, the photonic qubit is measured in one of the standard polarization bases:  $X = \{|H\rangle, |V\rangle\}$  (horizontal, vertical),  $Y = \{|D\rangle, |A\rangle\}$  (diagonal, antidiagonal),  $Z = \{|R\rangle, |L\rangle\}$  (right-, left-handed circular). In the circular basis, the linear polarizations are defined as

$$|H\rangle = \frac{1}{\sqrt{2}}(|R\rangle + |L\rangle) \quad (4.10)$$

$$|V\rangle = \frac{1}{\sqrt{2}}(|R\rangle - |L\rangle) \quad (4.11)$$

$$|D\rangle = \frac{1}{\sqrt{2}}(|R\rangle - i|L\rangle) \quad (4.12)$$

$$|A\rangle = \frac{1}{\sqrt{2}}(|R\rangle + i|L\rangle). \quad (4.13)$$

Upon detecting a photon, i.e. projecting it onto one particular of the six polarization states, we measure the ion in terms of the observables  $\sigma_x$ ,  $\sigma_y$  and  $\sigma_z$  (the relation of these to the more directly accessible observables  $\sigma_\phi$  and  $\sigma_z$  will be given in section 4.2.4).

I will now explain exemplarily how a particular expectation value  $w_{i,j}$  is determined experimentally. For example, the expectation value of the atomic  $\sigma_x$  observable is approximated through

$$\langle \sigma_x^{(\text{ion})} \otimes \mathbb{1}^{(\text{ph})} \rangle = p(|0\rangle_i^{(\text{ph})}) w_x^{(\text{ion})} \Big|_{|0\rangle_i^{(\text{ph})}} + p(|1\rangle_i^{(\text{ph})}) w_x^{(\text{ion})} \Big|_{|1\rangle_i^{(\text{ph})}}. \quad (4.14)$$

Here,  $p(|0\rangle_i^{(\text{ph})})$  denotes the probability to find the photon in state  $|0\rangle$  in some arbitrary measurement basis  $i$ , and  $w_x^{(\text{ion})} \Big|_{|0\rangle_i^{(\text{ph})}}$  is the expectation value of the atomic  $\sigma_x$  observable *conditioned* on the detection of a photon in state  $|0\rangle$  (and analogously for the photonic state  $|1\rangle$ ). If instead we are interested in the expectation value of the *photonic*  $\sigma_x$  observable, we find the simpler expression

$$\langle \mathbb{1}^{(\text{ion})} \otimes \sigma_x^{(\text{ph})} \rangle = p(|0\rangle_x^{(\text{ph})}) - p(|1\rangle_x^{(\text{ph})}). \quad (4.15)$$

Finally, for a joint measurement in the atomic  $\sigma_x$  and the photonic  $\sigma_y$  basis, the expectation value is approximated via

$$\langle \sigma_x^{(\text{ion})} \otimes \sigma_y^{(\text{ph})} \rangle = p(|0\rangle_y^{(\text{ph})}) w_x^{(\text{ion})} \Big|_{|0\rangle_y^{(\text{ph})}} - p(|1\rangle_y^{(\text{ph})}) w_x^{(\text{ion})} \Big|_{|1\rangle_y^{(\text{ph})}}. \quad (4.16)$$

With this “recipe”, we are equipped for reconstructing the joint atom-photon state through independent, but simultaneous measurements on ion and photon.

### Maximum-likelihood estimation

The procedure for two-qubit quantum-state tomography described above has the advantage of being “analytic”, which means only elementary mathematical operations are required to reconstruct the atom-photon density matrix from the experimentally determined probabilities. It has, however, one considerable drawback: the linear combination 4.9 is

not guaranteed to result in a physical density matrix  $\rho$  when the measured values for  $w_{i,j}$  are used as approximations. A physical density matrix needs to fulfill the requirements on a valid density operator: (i) Positive semi-definite (and thus Hermitian): all eigenvalues are nonnegative. (ii) Normalized:  $\text{tr}(\rho) = 1$ . This implies that the expectation values  $w_{i,j}$  must fulfill the boundary condition

$$\sum_{i,j=1}^4 w_{i,j}^2 - w_{1,1}^2 \leq 1. \quad (4.17)$$

This condition, however, may not be satisfied by experimentally determined values due to measurement errors and statistical uncertainties. A solution to this problem lies in asking instead for the particular physical quantum state which is most likely to have produced the experimental data, hence the term “maximum-likelihood estimation” [178, 175]. This requires a numerical search over all physical states, details of which are found in app. A.8. Maximum-likelihood estimation is a standard method for reconstructing density operators from experimental data [175]. The thus found density matrices then allow deriving secondary quantities, such as entanglement measures, that further characterize the quantum state.

It should be mentioned that maximum-likelihood estimation does not at all render the analytic reconstruction (eqn. 4.9) obsolete, since the analytic density operator is usually needed as initial guess for the numerical search.

#### 4.2.4 Experimental results

For the actual measurement, the set of wave plates for analyzing the polarization of the Raman photons are set such that one particular of the six polarization basis states<sup>7</sup>  $|H\rangle$ ,  $|V\rangle$ ,  $|D\rangle$ ,  $|A\rangle$ ,  $|R\rangle$ ,  $|L\rangle$  is transmitted through the polarizer and detected by the PMT. Once a photon has been projected onto this basis state, the atomic qubit is measured in either the energy eigenbasis  $\sigma_z$  (shelving the  $|+1/2\rangle$  qubit state to the  $D_{5/2}$  manifold<sup>8</sup>) or the superposition basis  $\sigma_\phi$  (basis rotation through a  $\frac{\pi}{2}$  RF pulse prior to electron shelving). For each of these 12 combinations of single-qubit measurement bases, both the detection time of the Raman photon and the outcome of the atomic measurement are recorded. Just as we did in the context of our state-transfer protocol, the experimental data is evaluated by sorting each photon-detection time into one of two arrival-time histograms according to the atomic-measurement outcome. Fig. 4.11(a) exemplarily shows such histograms for projecting the ion onto the  $\sigma_z$  basis conditioned on the detection of a Raman photon in state  $|R\rangle$ . As expected from eqn. 4.6, almost all photon detections are followed by a projection of the atomic state onto  $|+1/2\rangle$ . For the reconstruction of the atom-photon density matrix, we define a time window from which photon-detection events are selected. As a reasonable trade-off between detection efficiency and quantum-state fidelity, we choose a

<sup>7</sup>The linear polarizations are defined with respect to the plane spanned by the photon-generation beam and the quantization axis, which coincides with the plane of the optical table.

<sup>8</sup>The measured probability for a projection onto the state  $|+1/2\rangle$  is corrected for the shelving efficiency  $p_{\text{shelving}} = 97.0(8)\%$ .

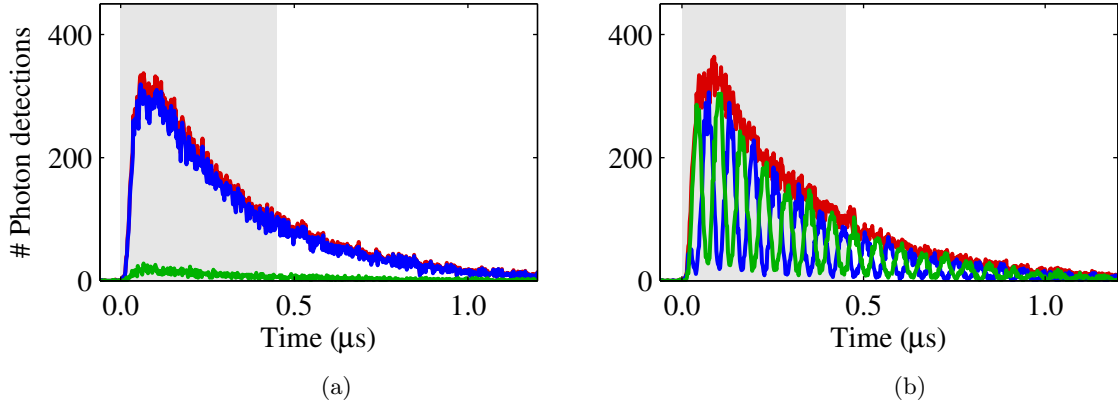


**Fig. 4.11:** Conditional arrival-time histograms of single 393 nm photons. Blue curve: ion in state  $|+1/2\rangle$ , green curve: ion in state  $|-1/2\rangle$ , red curve: unconditional arrival-time distribution (sum of the conditional histograms). (a) Projection onto the atomic  $\sigma_z$  basis after detecting a photon in state  $|R\rangle$ . (b) Projection onto the atomic  $\sigma_\phi$  basis after detecting a photon in state  $|H\rangle$ . The shaded areas represent the time window used for data analysis. For each graph, the bin size is 2 ns and the measurement time is 20 min.

window of 450 ns length. Averaged over all six polarization states, this yields 0.353(1)% detection efficiency. From the ratio of the number of events in the conditional arrival-time histograms, we find the approximation  $w_z^{(\text{ion})}|_{|0\rangle_z^{(\text{ph})}} = 0.944(16)$  for the expectation value of the atomic  $\sigma_z$  operator conditioned on the detection of a photon in state  $|0\rangle_z^{(\text{ph})} = |R\rangle$ . Repeating this measurement with the detection of photons in state  $|L\rangle$  then allows us to approximate the expectation values  $\langle \sigma_z^{(\text{ion})} \otimes \mathbb{1}^{(\text{ph})} \rangle$ ,  $\langle \mathbb{1}^{(\text{ion})} \otimes \sigma_z^{(\text{ph})} \rangle$  and  $\langle \sigma_z^{(\text{ion})} \otimes \sigma_z^{(\text{ph})} \rangle$ .

Besides measurements in the  $\sigma_z$  bases, fig. 4.11(b) displays the conditional arrival-time histograms for projecting the ion onto the superposition basis  $\sigma_\phi$  conditioned on the detection of a Raman photon in state  $|H\rangle$ . We observe oscillations in the conditional arrival-time distributions that have the same physical origin as the quantum beats described in section 3.2 (and the oscillations visible when characterizing our state-transfer protocol in section 4.1); the phase of the initially prepared superposition of  $|D_{5/2}, m = \pm 5/2\rangle$  evolves at the Larmor frequency of the two Zeeman states. Detecting a linearly polarized Raman photon projects this superposition onto that of  $|S_{1/2}, m = \pm 1/2\rangle$ , whose phase now evolves at the Larmor frequency given by the  $S_{1/2}$  Zeeman splitting. Hence, until the photon is detected, the ion accumulates a phase at the rate given by the difference of the two Larmor frequencies. The probability to project the final atomic state onto a given superposition state hence oscillates at that difference frequency. Including the Landé factors of the two fine-structure manifolds, the oscillation period (the *effective* Larmor period) which is seen in fig. 4.11(b) is

$$T = \frac{h}{4\mu_B B} = 63 \text{ ns} \quad (4.18)$$

for our static magnetic field  $B = 2.8 \text{ G}$ . Another interpretation of the accumulated phase is considering the measurement basis time-dependent; the time  $t$  of a photon detection

determines the phase  $\phi$  of the observable  $\sigma_\phi = \cos(\phi)\sigma_x - \sin(\phi)\sigma_y$  through

$$\phi = 2\pi \frac{t \bmod T}{T}. \quad (4.19)$$

Temporally resolving the Raman photons is thus crucial in keeping track of the phase of the atomic superposition state. Discarding it would cause the  $S_{1/2}$  superposition to decohere. Furthermore, this resolves yet another issue: the two  $\sigma$  channels of the  $S_{1/2}$ – $P_{3/2}$  transition yield photons that are distinguishable in frequency due to the Zeeman splitting. In principle, this implies entanglement of ion and photon not only in the spin but also the frequency degree of freedom. Since we analyze only the latter, the atom-photon quantum state would appear as statistically mixed. As we resolve the photons temporally, not spectrally, the frequency information is erased and the state remains pure (*quantum eraser* [167, 168, 169]).

### Reconstructing the two-qubit quantum state

In order to draw meaningful conclusions from the photonic wave packets in the case of projecting the ion onto the  $\sigma_\phi$  basis, we analyze visibility and phase offset of the oscillations in the arrival-time histograms. By the definition of the superposition observable,  $\sigma_\phi = \cos(\phi)\sigma_x - \sin(\phi)\sigma_y$ , it becomes apparent that visibility  $V$  and phase offset  $\phi_0$  relate to the expectation values  $w_x^{(\text{ion})}$  and  $w_y^{(\text{ion})}$  of the atomic observables  $\sigma_x$  and  $\sigma_y$  through

$$w_x^{(\text{ion})} = V \cos(\phi_0) \quad (4.20)$$

$$w_y^{(\text{ion})} = V \sin(\phi_0). \quad (4.21)$$

Hence, analyzing the atomic state in the superposition basis allows us to determine the values  $w_x^{(\text{ion})}$  and  $w_y^{(\text{ion})}$  simultaneously with just one experimental setting.

Now, after explaining how the experimental data acquired for the 12 settings of joint measurement bases translates into approximations for the expectation values  $w_{i,j} = \langle \sigma_i \otimes \sigma_j \rangle$  of the 16 two-qubit observables, we can reconstruct the atom-photon quantum state. The density matrix, reconstructed analytically from eqn. 4.9, turned out to be non-physical, exhibiting negative eigenvalues. Hence it was used as initial guess for a maximum-likelihood estimation, with the resulting density matrix shown in fig. 4.12. Importantly, most of the population is confined to the states  $|+1/2\rangle |\text{R}\rangle$  and  $|-1/2\rangle |\text{L}\rangle$ . The presence of the coherence terms shows that the atom-photon system is close to the maximally entangled state  $|\Psi\rangle = \frac{1}{\sqrt{2}} (|+1/2\rangle |\text{R}\rangle + |-1/2\rangle |\text{L}\rangle)$ .

### Entanglement measures

It is illustrative to quantify the amount of entanglement contained in the reconstructed two-qubit quantum state  $\rho$  through measures of entanglement [179]. One of them is the fidelity with respect to the maximally entangled state  $|\Psi\rangle = \frac{1}{\sqrt{2}} (|+1/2\rangle |\text{R}\rangle + |-1/2\rangle |\text{L}\rangle)$ :

$$F = \langle \Psi | \rho | \Psi \rangle = 84.6(2) \% \quad (4.22)$$

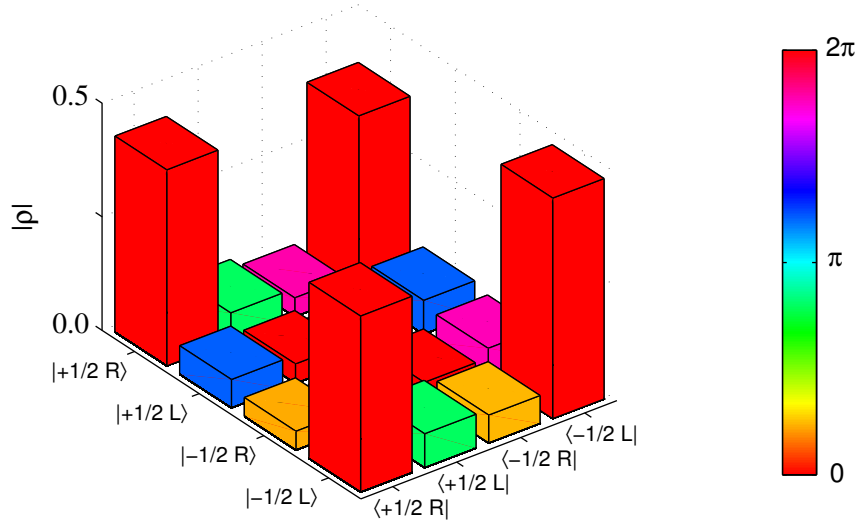


**Fig. 4.12:** Density matrix of the joint atom-photon state, represented in the  $Z^{(\text{ion})}-Z^{(\text{ph})}$  product basis. Shown are the moduli of the matrix entries; the colors represent the entries' complex arguments.

It clearly exceeds the value of  $\frac{1}{2}$  for a classical correlation and thus indicates the presence of entanglement.

Another measure of entanglement is found in *Bell's inequality* in the CHSH formulation [180]: for non-entangled (separable) quantum states, the Bell parameter

$$S := |\langle \sigma_\alpha \otimes \sigma_\beta \rangle + \langle \sigma_{\alpha'} \otimes \sigma_\beta \rangle| + |\langle \sigma_\alpha \otimes \sigma_{\beta'} \rangle - \langle \sigma_{\alpha'} \otimes \sigma_{\beta'} \rangle| \quad (4.23)$$

must fulfill the inequality  $S \leq 2$  for *any* choice of the measurement bases parameterized by the angles  $\alpha, \alpha', \beta, \beta'$ . In the case of maximally entangled states, however, an appropriate choice of these angles allows for values of  $S$  up to  $2\sqrt{2}$ . By numerically optimizing this choice of measurement bases, we find the maximized Bell parameter  $S = 2.305(9)$ , exceeding the value of 2 by more than 30 standard deviations and thus once more indicating the presence of entanglement in the atom-photon state.

#### 4.2.5 Error sources

While the main sources of error in the realization of our protocol for heralded photon-to-atom quantum-state transfer were found in detector dark counts and decay from the  $P_{3/2}$  back to the  $D_{5/2}$  state, the main reasons for the non-perfectly entangled atom-photon state are different: first, magnetic-field noise was not nearly as well compensated as it had been for the realization of the state-transfer protocol. Since the magnetic-field direction had to be rotated by  $90^\circ$  for the generation of atom-photon entanglement, the influence of the laboratory devices on the magnetic field at the position of the ion changed completely. Repositioning the devices and their cables, however, did not stabilize the field as much as hoped for.

Second, the half-wave and quarter-wave plate used for choosing the polarization state that a detected photon was projected on did not show retardances sufficiently close to  $\frac{\lambda}{2}$  and  $\frac{\lambda}{4}$ , respectively. Since characterizing them turned out hard, they introduced a systematic error into the polarization analysis and hence into the reconstructed density matrix.

### Summary

We have experimentally realized the generation of an entangled atom-photon quantum state. The photon is Raman scattered on the  $S_{1/2}$ - $P_{3/2}$  transition of  $^{40}\text{Ca}^+$ , its polarization state entangled with the ion's  $S_{1/2}$  Zeeman qubit. At  $\sim 0.35\%$  photon-detection efficiency and 11 kHz repetition rate, we obtain the fidelity 84.6(2)% with respect to an ideal, maximally entangled quantum state.

These results allow us to keep up with work from competing groups; experiments employing high-NA objectives for photon collection from single atoms/ions showed photon-detection probabilities up to  $\sim 0.4\%$ , however at repetition rates up to  $\sim 500$  kHz and with quantum-state fidelities in the range 92 – 95% [66, 144]. Cavity-based ion-photon entanglement was attained at  $\sim 6\%$  detection efficiency and 97% fidelity, but at  $< 1$  kHz repetition rate [174].

# Chapter 5

## Conclusion

### 5.1 Related work: Photonic interaction between distant ions

In parallel to the work presented in this thesis, another experiment was conducted that is described in detail in Michael Schug's Ph.D. thesis [93] and our publication [155]; we successfully demonstrated heralded photonic interaction between single ions in our two traps, spatially separated by  $\sim 1$  m.

In chapters 3 and 4, I presented building blocks for interfacing single  $^{40}\text{Ca}^+$  ions with single photons, namely the high-rate generation of single photons, atom-to-photon phase mapping, photon-to-atom quantum-state transfer and atom-photon entanglement. All these operations focus on implementing a single node in a quantum network; we have now realized a proof-of-principle experiment which makes use of both our ion traps and a photonic quantum channel for the direct interaction between single ions in the two traps. In the sender trap (the Bright Trap), we use a single ion to emit photons at 854 nm wavelength, the photon generation being either triggered or continuous. Single-photon absorptions by a single ion in the receiver trap (the Dark Trap) are heralded by the onset of fluorescence light, scattered from the cooling lasers. This *quantum-jump scheme* allows for near-unity detection efficiency of single-photon absorptions.

#### Experimental implementation

Our experimental setup is depicted in fig. 5.1. In the sender trap, a single ion is made to emit photons at 854 nm. For continuous photon generation, lasers at various wavelengths drive the ion to a steady state with high population in the  $P_{3/2}$  manifold, causing it to scatter photons on the  $D_{5/2}$ - $P_{3/2}$  transition (at 854 nm) at a high rate. For triggered photon generation, the ion is optically pumped from the  $S_{1/2}$  to the  $D_{5/2}$  state, scattering a single photon at 854 nm (see section 3.1.2). The photons are collected through one of our high-NA laser objectives (HALOs) and coupled to a single-mode optical fiber.

In the receiver trap, the cooling lasers are switched on at all times, and the ion is prepared for absorption in the  $D_{5/2}$  state (which is a dark state to the cooling beams) through optical pumping. Light from the sender ion exits the single-mode fiber and is focused onto the receiver ion through another HALO. The absorption of a photon excites

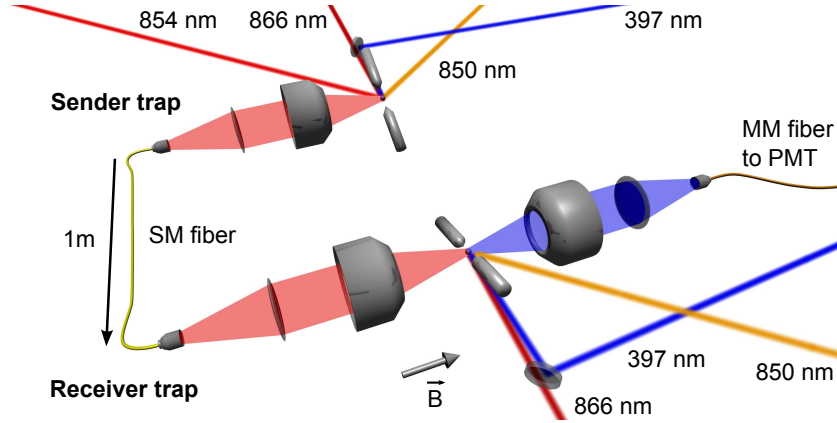


**Fig. 5.1:** Experimental setup for heralded photonic interaction.  $\vec{B}$ : magnetic-field direction, SM fiber: single-mode optical fiber, MM fiber: multi-mode optical fiber, PMT: photomultiplier tube.

the receiver ion to the  $P_{3/2}$  state, from which it predominantly decays to the ground state, entering the cooling cycle and emitting fluorescence light (quantum jump). The detection of a fluorescence photon from the receiver ion then signals (heralds) the successful absorption<sup>1</sup> of a photon from the sender ion.

## Results

In the case of continuous photon transmission, we obtain single-mode coupled photons at a rate of  $R_{\text{ph}} = 12.2(2.5) \cdot 10^3 \text{ s}^{-1}$ . The successful absorption of a photon by the receiver ion is heralded by the onset of fluorescence; we detect the latter at the rate  $R_{\text{fl}} \approx 300 \cdot 10^3 \text{ s}^{-1}$ . The first detection of a fluorescence photon marks the point in time of the absorption event, hence the temporal resolution is given by  $1/R_{\text{fl}} \approx 3.3 \mu\text{s}$ . For each quantum jump, the time that the ion spent in the  $D_{5/2}$  state (the dark-period duration) before returning into the cooling cycle is recorded and sorted into a histogram, see fig. 5.2(a). The mean dark-period duration is found to be  $\tau_{\text{on}} = 247(6) \text{ ms}$  and must be compared with the reference value  $\tau_{\text{off}} = 1022(34) \text{ ms}$  obtained when the sender ion is “off”, i.e. when the laser beams in the sender trap are switched off. Evidently, the transmission of photons from the sender ion significantly reduces the effective lifetime of the  $D_{5/2}$  state (from the natural lifetime of  $\sim 1 \text{ s}$  by a factor of  $\sim 4$ ). From these two values for the mean dark-period duration, we derive the photon-absorption rate  $R_{\text{abs}} = 1/\tau_{\text{on}} - 1/\tau_{\text{off}} = 3.07(10) \text{ s}^{-1}$ . Normalizing this to the rate of photons sent onto the receiver ion, we arrive at the value  $p_{\text{abs}} = R_{\text{abs}}/R_{\text{ph}} = 2.5(5) \cdot 10^{-4}$  for the absorption probability for a single photon.

In most quantum-networking scenarios, however, the more interesting mode of operation is triggered photon transmission. With 1.89(39)% fiber-coupling efficiency and 31.2 kHz sequence repetition rate, we obtain single photons at the receiver ion at a rate of  $590(120) \text{ s}^{-1}$ . Like in the case of continuous photon transmission, absorption events at

<sup>1</sup>In this context, “successful absorption” refers to the absorption of a photon, followed by the ion entering the cooling cycle (in contrast to decaying back to the  $D_{5/2}$  state, which occurs with 5.9% probability [156]).

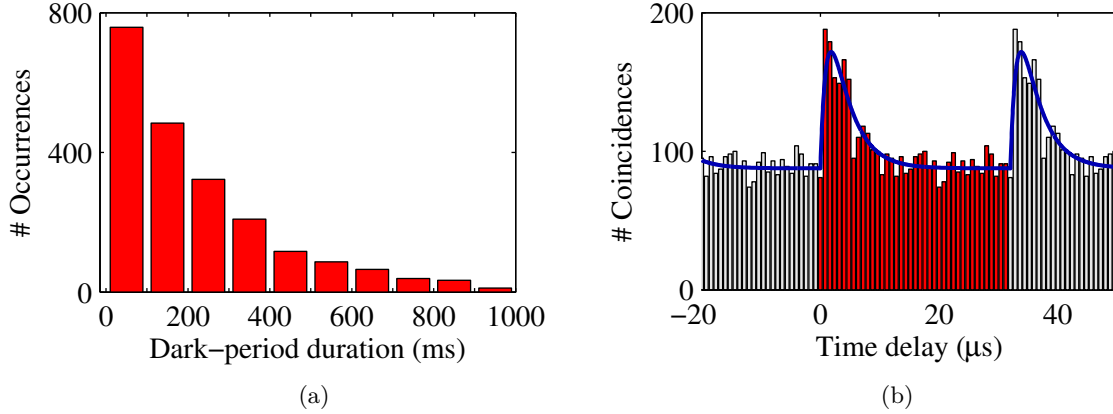


**Fig. 5.2:** Heralded single-photon absorption. (a) Continuous photon transmission; shown is a histogram of dark-period durations, following the preparation of the receiver ion in the  $D_{5/2}$  state. The bin size is 100 ms and the measurement time is 15 min. (b) Triggered photon transmission; shown is a time-delay histogram of coincidences between single-photon-emission triggers at the sender ion and absorption events (quantum jumps) at the receiver ion. The bin size is 800 ns and the measurement time is 74 min. The signal repeats at the sequence repetition rate (gray areas).

the receiver ion are heralded by the onset of fluorescence and time-stamped by the first detected fluorescence photon. The result is shown in fig. 5.2(b), the temporal correlation function between single-photon-emission triggers at the sender ion and absorption events at the receiver ion. The prominent peak at zero time delay evidences the strong correlation between triggered photon emission and single-photon absorption. The shape of the peak is composed of the photon's temporal shape (exponential, the  $\frac{1}{e}$  time of  $1.09(1) \mu\text{s}$  determined from an independent measurement) and the quantum-jump timing resolution ( $\sim 3.3 \mu\text{s}$ ). Subtracting events of spontaneous decay from the  $D_{5/2}$  state, we find  $640(100)$  successful absorption events after 74 min of measurement time. This corresponds to a success rate (rate of photon emissions followed by absorption events) of  $0.14(2) \text{ s}^{-1}$ . Normalizing this value to the repetition rate yields  $4.6(7) \cdot 10^{-6}$  success probability and  $2.4(6) \cdot 10^{-4}$  photon-absorption probability for a single experimental cycle. The value for the absorption probability is compatible with that determined from continuous photon transmission.

## Summary

We have successfully demonstrated heralded interaction between spatially separated single ions through a photonic quantum channel, where photon-absorption events are detected through a quantum-jump scheme. In continuous photon-transmission mode, the sender ion continuously emits photons at 854 nm wavelength that shorten the lifetime of the metastable  $D_{5/2}$  state of the receiver ion at a rate of  $3.07(10) \text{ s}^{-1}$ . In triggered photon-transmission mode, the sender ion emits single photons that are temporally strongly correlated with absorption events at the receiver ion, yielding a success probability of  $4.6(7) \cdot 10^{-6}$  and a success rate of  $0.14(2) \text{ s}^{-1}$ .

## 5.2 Summary

In this dissertation, I presented the experimental implementation of basic quantum-networking operations, realized with single ions and single photons. Ions and photons were interfaced in free space by means of objectives of high numerical aperture ( $NA = 0.4$ ).

Prior to any quantum-networking operation, we needed to gain control over the atomic qubit. The  $S_{1/2}$  ground state and  $D_{5/2}$  metastable state in  $^{40}\text{Ca}^+$ , coupled by a narrow-band laser at 729 nm, were used as an optical qubit. First, we established the basic tasks of spectroscopy (with spectral resolutions on the order of 10 Hz) and pulse-length scans (exhibiting Rabi frequencies in the 100 kHz range) necessary for calibrating the laser excitation. Afterwards, we investigated the qubit's coherence properties. It turned out that fluctuations of the ambient magnetic field limit the coherence time to values on the order of 1 ms. Besides this optical qubit, we made use of the two  $S_{1/2}$  Zeeman states to form a radio-frequency qubit. An RF field generated through a copper-wire coil facilitates simple and coherent control over this qubit, offering two particular advantages: insensitivity of qubit manipulations to the ion's thermal motion and the use of an easy-to-handle direct digital synthesizer (DDS) as a reference oscillator in place of the complex setup of a laser locked to a high-finesse optical cavity. Pulse-length scans showed Rabi frequencies as high as 100 kHz, comparable to those from the optical qubit. For the initialization of both kinds of qubits prior to coherent manipulations, we implemented two complementary optical-pumping techniques which prepare the ion in one specific  $S_{1/2}$  Zeeman state with  $> 99.5\%$  fidelity. Also, I presented a robust method for measuring the ion's temperature in the trap potential ( $\sim 1$  mK).

Once control over the atomic qubit was achieved, we started toward basic quantum-networking experiments; our first step was the generation of single Raman photons at two different wavelengths which we tuned both temporally and spectrally. Single photons at 854 nm were single-mode fiber-coupled at a rate of  $3.0(6) \cdot 10^3 \text{ s}^{-1}$  [155], while photons at 393 nm were multi-mode coupled at  $5.5(2) \cdot 10^3 \text{ s}^{-1}$  [88]. In the next step, we coherently transferred the phase of an atomic superposition state onto the photonic quantum state through two distinct quantum-interference schemes [89]. This marks an important step toward mapping the ion's quantum state onto a single photon.

After these preliminary experiments, I presented the realization of two typical building blocks for quantum networks; we implemented a protocol in which the polarization state of a single photon is mapped onto the quantum state of a single ion through an absorption process [90]. The ion is projected onto the state of the absorbed photon by the detection of a Raman-scattered photon. This particular property of the protocol (*heralded* quantum-state transfer) allows for mapping the photonic onto the atomic quantum state with high fidelity, even in the case of low absorption probabilities. At  $\sim 0.4\%$  heralding probability for a successful photon absorption on the  $D_{5/2}-P_{3/2}$  transition, we achieved state-mapping fidelities exceeding 95%. The second building block is formed by an experiment entangling a single photon with the ion. To this end, a spontaneous Raman photon is emitted as the ion transitions from an excited to the ground state. This process takes place via two different atomic transitions, resulting in distinct final states of the ion's angular-momentum

degree of freedom. We thus achieved quantum-mechanical entanglement between the photonic polarization and the atomic spin. At  $\sim 0.35\%$  photon-detection efficiency, we obtained  $\sim 85\%$  fidelity with respect to an ideal, maximally entangled ion-photon state. The fidelity was mainly limited by magnetic-field fluctuations and difficulties in characterizing the wave plates used for photonic polarization analysis.

## 5.3 Outlook

### Magnetic-field stabilization

As explained and quantified in section 2.1.6, magnetic-field noise poses a serious problem regarding atomic-qubit coherence. In particular, it affects the realization of our protocol for mapping the quantum state of single photons onto the ion's spin state. More precisely, it severely limits the duty cycle of the experimental sequence as the ion must be repeatedly re-prepared even if no absorption has taken place (see section 4.1.9).

The only promising approach to stabilizing the magnetic field at the position of the ion is an active field compensation, which is currently being developed by Matthias Kreis [137]. A number of three-axis Hall sensors in the vicinity of the vacuum chamber allow inferring the magnetic field at the position of the ion, with  $\sim 1$  kHz significantly exceeding the bandwidth of single-ion spectroscopy. Compensation coils will then facilitate a closed feedback loop, with which we hope to significantly extend the atomic-qubit coherence time.

### Quantum-state transfer of heralded single photons

In the framework of this thesis, we demonstrated our protocol for photon-to-atom quantum-state transfer by mapping the polarization of weak coherent light pulses onto the ion's spin state. We will now proceed to the single-photon level; as mentioned earlier, we operate a photon-pair source, based on spontaneous parametric down-conversion (SPDC), that can be used as a heralded single-photon source. In the past, our group carried out proof-of-principle experiments demonstrating heralded absorption of single photons by a single ion [181, 182, 165, 166]. Single photons from the SPDC source were heralded by their partner photons and their absorption by the ion heralded by the onset of atomic fluorescence (quantum jumps).

In the next step, we will attempt to map the polarization state of an SPDC photon, heralded by its partner photon, onto the ion's spin state through our state-transfer protocol (see section 4.1). The presence of a single SPDC photon is heralded by its partner photon, and its absorption by the ion is heralded by the detection of a Raman-scattered photon. In a first experiment, we already showed the temporal correlation between the partner photon (for one particular polarization) and the Raman photon [183]. As the SPDC source can be operated such that it produces pairs of polarization-entangled photons, this scheme will facilitate entanglement between the partner photon and the ion. As explained above, however, we will require a significantly increased coherence time of the atomic qubit before being able to implement this scheme with an appreciable duty cycle.

### Frequency-converted single photons

We collaborate with the research group of Christoph Becher in the field of hybrid quantum networks [184, 185]. One of our goals of the near future is the frequency conversion of single photons from the near-visible range to the telecom O band. To this end, we will send photons at 854 nm emitted by the ion (see section 3.1.2) to a nonlinear waveguide which frequency-converts them to 1310 nm wavelength. This *quantum frequency conversion* [186, 187] is a very appealing concept as it bridges the gap between the (near-)visible transitions in most atomic species and the low-loss spectral windows of optical fibers in the near-infrared region.

### Greater vision

In a larger context, the experimental tools and methods presented in my thesis will facilitate the vision explained in the introduction; a network of small-scale processing units, interconnected through photonic quantum channels, will form quantum-information processors that will be able to tackle mathematical problems intractable on classical computers. Our tools, such as the coherent manipulation of optical and radio-frequency qubits, will enable local processing of quantum information, while networking functionalities like photon-to-atom quantum-state transfer and atom-photon entanglement are essential in connecting the individual processing units. In particular, our scheme for the heralded transfer of a photonic quantum state onto a trapped ion plays a key role; only with the high transfer fidelities provided by a heralded protocol will a truly useful quantum network become feasible.

# Appendix

## A.1 Properties of atomic states and transitions

Tab. A.1 lists the properties of the atomic states and the optical transitions of  $^{40}\text{Ca}^+$  which are relevant to our experimental situation.

State	Lifetime	Transition	Wavelength	Linewidth	Branching fraction
$P_{3/2}$	6.924(19) ns	$P_{3/2}-S_{1/2}$	393.3660 nm	22.986(63) MHz	0.934 7(3)
		$P_{3/2}-D_{3/2}$	849.8015 nm	22.986(63) MHz	0.006 61(4)
		$P_{3/2}-D_{5/2}$	854.2087 nm	22.986(63) MHz	0.058 7(2)
$P_{1/2}$	7.098(20) ns	$P_{1/2}-S_{1/2}$	396.8466 nm	22.423(63) MHz	0.935 65(7)
		$P_{1/2}-D_{3/2}$	866.2137 nm	22.423(63) MHz	0.064 35(7)
$D_{5/2}$	1.168(9) s	$D_{5/2}-S_{1/2}$	729.1464 nm	136.3(1.1) mHz	1
$D_{3/2}$	1.176(11) s	$D_{3/2}-S_{1/2}$	732.3886 nm	135.3(1.3) mHz	1
$S_{1/2}$	stable				

**Tab. A.1:** Relevant atomic states and optical transitions of  $^{40}\text{Ca}^+$ . The  $P_{3/2}$  and  $P_{1/2}$  natural lifetimes were taken from [121], while those of the  $D_{5/2}$  and  $D_{3/2}$  state are from [122]. The  $P_{3/2}$  and  $P_{1/2}$  branching fractions were taken from [156] and [123], respectively. The natural linewidth of each transition is calculated from the natural lifetime of the upper and lower state. The transition wavelengths (in standard air) were measured with a wavelength meter (HighFinesse, WS/7 Super Precision), the uncertainties being on the order of  $10^{-4}$  nm.

## A.2 Adiabatic passage

Many tasks in quantum-information processing with trapped ions require the ability to efficiently transfer population between atomic energy eigenstates. A typical goal is to transfer all population from a particular  $S_{1/2}$  Zeeman state to a (non-populated)  $D_{5/2}$  state. This is usually done through a laser pulse of rectangular temporal shape which is resonant with the atomic carrier transition. Ideally, for the pulse area  $A = \Omega \cdot T = \pi$  with Rabi frequency  $\Omega$  and duration  $T$ , the laser will transfer the entire atomic population from the  $S_{1/2}$  to the  $D_{5/2}$  Zeeman state. Besides decoherence through magnetic-field

fluctuations, as touched on in section 2.1.5, a more severe complication arises from the ion's motional state.

### Decoherence through spin-motion entanglement

As described in section 1.1.3, the motion of a laser-cooled ion is well approximated by a thermal state, i.e. a Boltzmann distribution in Fock space, characterized entirely by the expectation value  $\langle n \rangle$  of the motional quantum number. Since the ion is brought into this state through spontaneous scattering of photons from the field of the cooling laser, the motion is described in the Fock basis by a completely mixed quantum state:

$$\rho_{\text{mot}} = \sum_{n=0}^{\infty} p_n |n\rangle \langle n| \quad (\text{A.1})$$

with the thermal distribution  $p_n = \frac{\langle n \rangle^n}{(\langle n \rangle + 1)^{n+1}}$ . Assuming the electronic state to be initially in the ground state  $\rho_{\text{el}} = |g\rangle \langle g|$ , the joint density operator for the two degrees of freedom reads

$$\rho(t=0) = \rho_{\text{el}} \otimes \rho_{\text{mot}} \quad (\text{A.2})$$

$$= |g\rangle \langle g| \otimes \sum_{n=0}^{\infty} p_n |n\rangle \langle n| \quad (\text{A.3})$$

$$= \sum_{n=0}^{\infty} p_n |g\rangle \langle g| \otimes |n\rangle \langle n|. \quad (\text{A.4})$$

From eqn. 1.32 and for a laser pulse resonant with the carrier transition ( $\Delta = 0$ ) and of not too high intensity ( $\Omega \ll \omega_{\text{T}}$ ), the interaction Hamiltonian describing the dynamics of the electronic quantum state *for a specific motional state*  $|n\rangle$  simplifies to

$$H_{\text{int},n} = \frac{\hbar\Omega_n}{2} (|e\rangle \langle g| + |g\rangle \langle e|) \quad (\text{A.5})$$

with the motion-dependent Rabi frequency

$$\Omega_n = \Omega \left| \langle n | e^{i\eta(a+a^\dagger)} | n \rangle \right| \quad (\text{A.6})$$

$$= \Omega e^{-\eta^2/2} L_n^0(\eta^2). \quad (\text{A.7})$$

Since this Hamiltonian is time-independent and does not couple the different motional states, we can apply the time-evolution operator  $U_n(t) = e^{-iH_{\text{int},n}t/\hbar}$  individually to each of the summands in eqn. A.4. After tracing over the motional part, we find the electronic state

$$\rho_{\text{el}}(t) = \sum_{n=0}^{\infty} p_n U_n(t) |g\rangle \langle g| U_n^\dagger(t), \quad (\text{A.8})$$

from which we readily obtain the probability for a projection onto the excited state:

$$p_{|e\rangle}(t) = \langle e | \rho_{\text{el}}(t) | e \rangle \quad (\text{A.9})$$

$$= \frac{1}{2} \left( 1 - \sum_{n=0}^{\infty} p_n \cos(\Omega_n t) \right) \quad (\text{A.10})$$

We see now that for a thermal state which comprises many individual Fock states  $|n\rangle$ , Rabi oscillations between states  $|g\rangle$  and  $|e\rangle$  no longer occur at a well-defined frequency  $\Omega$  but at a multitude of frequencies  $\Omega_n$ . As these frequencies are in general incommensurable, the sum in eqn. A.10 will not reach the value  $-1$  at any time  $t$ , and thus the population cannot be efficiently transferred to the excited state. This effect becomes more dramatic the higher the mean motional quantum number  $\langle n \rangle$  is.

This damping of Rabi oscillations can be viewed as a process of decoherence; as the Rabi frequency depends on the motional quantum number  $n$ , the electronic state after a given time will be different for each of the Fock states involved – the ion’s electronic state (its spin) has become entangled with its motion. The joint electronic and motional state is still a pure one, but as we observe only the electronic state, i.e. we trace over the motion, we obtain a statistical mixture, a decohered state.

### The adiabatic-passage technique

As explained above, the transfer efficiency between two energy eigenstates when using resonant laser pulses suffers (greatly) from the ion’s motion when the latter is not cooled to the ground state of the trap potential. As shown above, the reason for this lies in the motion-dependent Rabi frequency. A different approach for which the transfer efficiency is less affected by a variation of the Rabi frequency would thus be favorable.

The idea of adiabatic passage relies on the adiabatic theorem: a quantum-mechanical system initially prepared in an eigenstate of its Hamiltonian will remain in the corresponding eigenstate when the Hamiltonian varies in time, as long as the variation occurs on a time scale much longer than the internal dynamics of the system [188]. Applied to our two-level system, this leads to the condition

$$\frac{\dot{E}}{E} \ll \frac{E}{\hbar} \quad (\text{A.11})$$

for the time-dependent transition energy  $E$ . For an adiabatic process, this condition must be fulfilled at all times. We would now like to engineer a Hamiltonian for which the initial lowest-energy state corresponds to the ground state  $|g\rangle$ , while the final lowest-energy state corresponds to the excited state  $|e\rangle$ . When the Hamiltonian is changed slowly in time, the system will always be in the lower energy eigenstate of the current Hamiltonian and is thus adiabatically driven from state  $|g\rangle$  to  $|e\rangle$ .

For our system, the free Hamiltonian parameters are the Rabi frequency  $\Omega$  and the detuning  $\Delta$  from the atomic resonance. The interaction Hamiltonian 1.32 is time-dependent already by itself and thus not well suited for the description of this process since Rabi frequency and detuning are now a function of time as well. Instead, we will transform it to the reference frame of the laser field, in which it is time-independent for given values of  $\Omega$  and  $\Delta$ . This is known as the *dressed-state* picture [116].

As in the previous paragraph, we will consider only the electronic degree of freedom and absorb the motional state in the magnitude of the Rabi frequency. In the Schrödinger picture, we thus find the system Hamiltonian

$$H_{\text{sys}} = \frac{\hbar\omega_0}{2} (|e\rangle\langle e| - |g\rangle\langle g|) \quad (\text{A.12})$$

and the interaction Hamiltonian

$$H_{\text{int}} = \frac{\hbar\Omega}{2} (|e\rangle\langle g| + |g\rangle\langle e|) (e^{-i\omega_L t} + e^{i\omega_L t}). \quad (\text{A.13})$$

With the definition

$$H_0 := \frac{\hbar\omega_L}{2} (|e\rangle\langle e| - |g\rangle\langle g|) \quad (\text{A.14})$$

and  $U = e^{iH_0 t/\hbar}$ , we then transform the Hamiltonian describing the entire system to the reference frame of the laser (including the transition energy):

$$H_{\text{int}}^L = U (H_{\text{sys}} + H_{\text{int}} - H_0) U^\dagger \quad (\text{A.15})$$

$$= -\frac{\hbar\Delta}{2} (|e\rangle\langle e| - |g\rangle\langle g|) + \frac{\hbar\Omega}{2} (|e\rangle\langle g| + |g\rangle\langle e|) \quad (\text{A.16})$$

In the second step, we performed once more the rotating-wave approximation. Diagonalization finally yields the energy eigenstates

$$|+\rangle = \cos\theta |g\rangle + \sin\theta |e\rangle \quad (\text{A.17})$$

$$|-\rangle = \sin\theta |g\rangle - \cos\theta |e\rangle \quad (\text{A.18})$$

with the mixing angle  $\theta$  defined by  $\tan\theta = \frac{\sqrt{\Omega^2 + \Delta^2} - \Delta}{\Omega}$  and the energy eigenvalues

$$E_{\pm} = \pm \frac{\hbar}{2} \sqrt{\Omega^2 + \Delta^2}. \quad (\text{A.19})$$

Fig. A.1(a) shows the energy eigenstates and eigenvalues as a function of the detuning parameter  $\Delta$ . For large negative detunings, the lower (higher) energy eigenstate is given by the ground state  $|g\rangle$  (excited state  $|e\rangle$ ). At resonance, the eigenstates are symmetric superpositions  $|\pm\rangle = (|g\rangle \pm |e\rangle)/\sqrt{2}$  of ground and excited state with energy splitting  $\hbar\Omega$ . This situation corresponds to resonant Rabi oscillations, where  $|g\rangle$  and  $|e\rangle$  are no longer stable solutions. Far above resonance,  $|g\rangle$  and  $|e\rangle$  are eigenstates once more, but their energies are exchanged compared with large negative detunings. This picture nicely illustrates how a system initially in state  $|g\rangle$  is adiabatically driven into the excited state  $|e\rangle$  by sweeping the laser frequency across the atomic resonance.

The adiabaticity condition A.11 with  $E = E_+ - E_- = \hbar\sqrt{\Omega^2 + \Delta^2}$  dictates

$$\frac{d}{dt} \sqrt{\Omega^2 + \Delta^2} \ll \Omega^2 + \Delta^2 \quad (\text{A.20})$$

at any point in time. The adiabatic passage is then typically performed through a chirped laser pulse with a smooth temporal envelope. The chirp provides the sweep across resonance, while the smooth envelope makes sure adiabaticity is attained. For our experiment, we choose a pulse of Gaussian shape with an intensity FWHM of  $T = 100 \mu\text{s}$ , peak Rabi frequency  $\Omega_{\text{peak}} = 2\pi \cdot 25 \text{ kHz}$  and a linear chirp<sup>1</sup>, sweeping the laser detuning as  $\Delta(t) = \omega_{\text{chirp}} \cdot t/T$  with  $\omega_{\text{chirp}} = 2\pi \cdot 25 \text{ kHz}$  and  $t = 0$  at peak intensity. The transfer efficiency from state  $|g\rangle$  to  $|e\rangle$  as a function of the mean motional quantum number

<sup>1</sup>The chirp is chosen small enough as not to excite motional sidebands or other atomic transition.

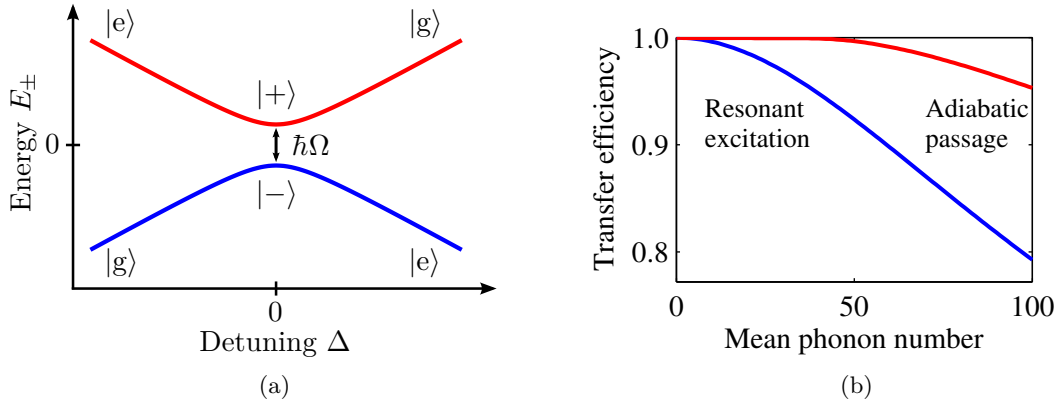


**Fig. A.1:** (a) Energies of the eigenstates of a two-level system under the effect of a laser field of Rabi frequency  $\Omega$  and detuning  $\Delta$ . (b) Numerical simulation of the ground-to-excited-state transfer efficiency as a function of the mean motional quantum number, for both adiabatic passage and a resonant pulse. For adiabatic passage, we choose the peak Rabi frequency of the Gaussian pulse  $\Omega_{\text{peak}} = 2\pi \cdot 25 \text{ kHz}$ , the FWHM value  $T = 100 \mu\text{s}$  and the frequency chirp  $\omega_{\text{chirp}} = 2\pi \cdot 25 \text{ kHz}$ . The resonant excitation is carried out with the pulse duration optimized for highest transfer efficiency.

$\langle n \rangle$  is numerically calculated in fig. A.1(b), comparing it to resonant excitation through a rectangularly shaped pulse with optimized pulse duration. As is seen, the adiabatic passage technique is expected to be superior to the resonant excitation already for very small values of  $\langle n \rangle$  and should remain above 99 % transfer efficiency for values as large as  $\langle n \rangle = 60$ .

For the experimental implementation, we choose one of the atomic transitions least susceptible to magnetic-field fluctuations, i.e.  $|S_{1/2}, m = -1/2\rangle \leftrightarrow |D_{5/2}, m = -1/2\rangle$ , since the pulse length  $T = 100 \mu\text{s}$  is already on the order of our typical qubit coherence times. As our sequence-control unit (Hydra) cannot change amplitude or frequency of the AOM RF drive in a continuous manner, both the Gaussian amplitude and the linear frequency chirp are approximated over a time of  $400 \mu\text{s}$  by 100 segments of constant value. In order to assess the adiabatic-passage performance, we cool the ion to two distinct motional states by appropriately choosing the power of the 397 nm cooling beam. For the standard cooling situation, we reach the mean motional quantum number  $\langle n \rangle = 20(1)$  for the ion’s axial motion in the trap (the “cool” state). See section 2.5 on our technique for ion-temperature measurement. For a higher cooling-beam power, however, the ion reaches a motional state of  $\langle n \rangle = 99(3)$  (the “warm” state).

The evolution of the population in the  $D_{5/2}$  state during the chirped laser pulse is shown in fig. A.2. For the cool state and the frequency chirp  $\omega_{\text{chirp}} = 2\pi \cdot 25 \text{ kHz}$ , we reach 98.06(4) % transfer efficiency at the end of the pulse. This is still comparable to the resonant excitation, which reaches 97.39(5) %. When bringing the ion into the warm state, the transfer efficiency is significantly reduced for both techniques. Still, the adiabatic passage performs much better (83.3(1) %) than the resonant excitation (68.4(1) %). However, all four values lie below what we expect from the numerical simulation. For the adiabatic passage, we attribute this to the magnetic-field fluctuations present during the

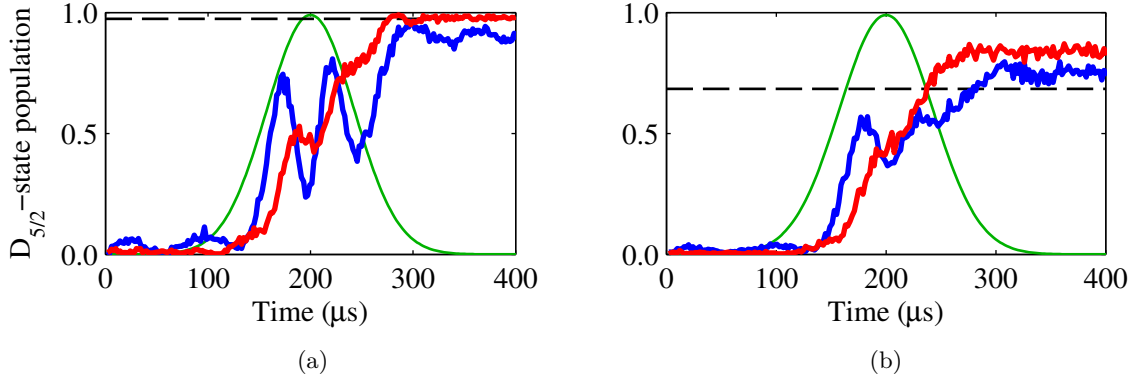


**Fig. A.2:** Adiabatic passage on the  $|S_{1/2}, m = -1/2\rangle \leftrightarrow |D_{5/2}, m = -1/2\rangle$  transition. Shown is the evolution of the  $D_{5/2}$ -state population during the chirped laser pulse for mean quantum numbers (a)  $\langle n \rangle = 20(1)$  and (b)  $\langle n \rangle = 99(3)$  for the ion's axial motion in the trap. The pulse envelope is indicated in green. All measurements were performed with Rabi frequency  $\Omega_{\text{peak}} = 2\pi \cdot 25$  kHz and FWHM value  $T = 100$   $\mu\text{s}$ . For the red curves, the frequency chirp  $\omega_{\text{chirp}} = 2\pi \cdot 25$  kHz had been chosen, while for the blue curves it had been reduced to  $\omega_{\text{chirp}} = 2\pi \cdot 10$  kHz. The dashed lines show the transfer efficiency for a resonant rectangularly shaped pulse with optimized pulse duration.

chirped pulse. For the resonant excitation, the Rabi frequency may have been too high such that sideband and other carrier transitions were driven as well, removing population from what is otherwise a two-level system.

We also investigate how the adiabatic passage reacts to a change in the frequency chirp  $\omega_{\text{chirp}}$ . While a value of  $\omega_{\text{chirp}} = 2\pi \cdot 25$  kHz over the pulse duration  $T$  appears sufficient to fulfill the adiabaticity condition A.20, the process is no longer adiabatic for a reduction to  $\omega_{\text{chirp}} = 2\pi \cdot 10$  kHz, as is seen from the Rabi oscillations around the pulse center.

It should be mentioned at this point that similar work has already been conducted in other groups; adiabatic passage has been shown to be insensitive to variations in the laser parameters [189] as well as to laser frequency noise [190].

In conclusion, I have shown that the technique of adiabatic passage is a tool superior to simple resonant excitations when confronted with the task of efficient population transfer in the electronic degree of freedom of an ion in a high-lying motional state. Loss in transfer efficiency through magnetic-field fluctuations can in principle be avoided by making the process faster, i.e. making the pulse shorter and increasing frequency chirp and Rabi frequency. At some point, however, the pulse will become spectrally broad enough to excite other atomic transitions, once more degrading the transfer efficiency.

### A.3 Probability distribution of an oscillating magnetic field

The power-line magnetic field is approximated by  $B(t) = B_0 \sin(\omega t)$  with  $\omega = 2\pi \cdot 50$  Hz (omitting higher harmonics). This represents a monochromatic oscillator, which has a well-defined phase relation to itself between any two points in time. However, when the

experimental sequence is not triggered to the power line, there is no phase relation between the atomic qubit and the power-line magnetic field. Instead, each cycle occurs at a random phase of the power-line oscillation. As the coherent manipulations are carried out on a time scale much shorter than the 50 Hz period, the magnetic field may be considered static during one experimental cycle. Averaged over many cycles, however, the field is a stochastic variable of which we are going to derive the probability distribution.

The probability  $P(B)$  to find a certain magnetic-field value  $B$  at a random point in time is proportional to the time that the field “spends” at a certain value, which is again inversely proportional to the time derivative

$$|\dot{B}(t)| = \omega B_0 |\cos(\omega t)| \quad (\text{A.21})$$

$$= \omega B_0 \cos\left(\arcsin\left(\frac{B}{B_0}\right)\right) \quad (\text{A.22})$$

$$= \omega B_0 \sqrt{1 - \left(\frac{B}{B_0}\right)^2}. \quad (\text{A.23})$$

From  $P \propto 1/|\dot{B}|$  and the normalization condition

$$\int_{-B_0}^{B_0} P(B) dB = 1, \quad (\text{A.24})$$

we find

$$P(B) = \frac{1}{\pi B_0} \frac{1}{\sqrt{1 - \left(\frac{B}{B_0}\right)^2}} \quad (\text{A.25})$$

(which is independent of the oscillation frequency  $\omega$ ).

## A.4 Ramsey-fringe visibility

Fluctuations of the magnetic field at the position of the ion lead to a loss of coherence between the atomic qubit state and the reference laser. Inferring the spectral properties of these fluctuations through an atomic ion has been studied and described in [191, 192]. Here, we restrict ourselves to assuming a given probability distribution (e.g. a Gaussian distribution for white field noise) with the magnetic-field amplitude as a free parameter which we would like to infer from the measured Ramsey-fringe visibility  $V(T)$  as a function of the Ramsey time  $T$ .

In an ideal environment without magnetic-field fluctuations, one expects Ramsey fringes (of the  $D_{5/2}$  population) of the form

$$p(\phi) = \frac{1}{2} (1 + \cos(\phi)) \quad (\text{A.26})$$

with the Ramsey phase  $\phi$  between the two  $\frac{\pi}{2}$  pulses. But as the magnetic field does change from one experimental cycle to the next, the ion acquires a stochastic phase  $\varphi$  relative to

the laser which is described by a probability distribution  $P_\varphi(\varphi)$ . The Ramsey phase is hence shifted by this stochastic phase, and we find the modified Ramsey fringes

$$p(\phi) = \int_{-\infty}^{\infty} \frac{1}{2} (1 + \cos(\phi - \varphi)) P_\varphi(\varphi) d\varphi \quad (\text{A.27})$$

$$= \int_{-\infty}^{\infty} \frac{1}{2} (1 + \cos(\phi) \cos(\varphi) + \sin(\phi) \sin(\varphi)) P_\varphi(\varphi) d\varphi. \quad (\text{A.28})$$

At the same time, the fringes are described as a cosine function with reduced visibility:

$$p(\phi) = \frac{1}{2} (1 + V \cos(\phi)) \quad (\text{A.29})$$

If we assume the probability distribution  $P_\varphi(\varphi)$  to be an even function (which is true for white and power-line noise), the term  $\sin(\phi) \sin(\varphi)$  in eqn. A.28 vanishes when performing the integration, and we identify the visibility as

$$V = \int_{-\infty}^{\infty} P_\varphi(\varphi) \cos(\varphi) d\varphi. \quad (\text{A.30})$$

The next step is to express the probability distribution  $P_\varphi(\varphi)$  for the stochastic phase in terms of the probability distribution  $P_B(B)$  for the magnetic-field fluctuations. Here the Ramsey time  $T$  comes into play, as longer time spans between the two  $\frac{\pi}{2}$  pulses will cause larger phase uncertainties. For an experimental cycle in which a certain magnetic field  $B$  is present, the phase acquired by the atomic state is

$$\varphi = g_{\text{eff}} \frac{\mu_B}{\hbar} B \cdot T. \quad (\text{A.31})$$

Here,  $g_{\text{eff}}$  is the effective Landé factor of the transition in question<sup>2</sup>. For the particular transition  $|S_{1/2}, m = -1/2\rangle \leftrightarrow |D_{5/2}, m = -1/2\rangle$ , it amounts to  $g_{\text{eff}} = \frac{2}{5}$ . With this relation, we transform from the probability distribution for the stochastic phase to that for the magnetic field:

$$P_\varphi(\varphi) = P_B(B) \frac{dB}{d\varphi} \quad (\text{A.32})$$

$$= \frac{1}{T} \frac{\hbar}{g_{\text{eff}} \mu_B} P_B(B) \quad (\text{A.33})$$

Inserting this expression into eqn. A.30 then finally yields the Ramsey-fringe visibility  $V(T)$  as the cosine transform of the probability distribution for the magnetic-field fluctuations:

$$V(T) = \int_{-\infty}^{\infty} P_B(B) \cos\left(g_{\text{eff}} \frac{\mu_B}{\hbar} B \cdot T\right) dB \quad (\text{A.34})$$

If several, independent sources for magnetic-field noise are present, the probability distribution  $P_B(B)$  is given by the convolution of the individual distributions. By virtue of the convolution theorem, the visibility  $V(T)$  is then simply the product of the visibilities for the individual noise sources.

---

<sup>2</sup>For an arbitrary transition  $|S_{1/2}, m_S\rangle \leftrightarrow |D_{5/2}, m_D\rangle$ , the effective Landé factor is defined as  $g_{\text{eff}} := |g_D m_D - g_S m_S|$  with  $g_D = \frac{6}{5}$  and  $g_S = 2$ .

## A.5 Spectrum of a single-photon wave packet

Experimentally determining the temporal and spectral properties of single-photon states usually yields only the probability distributions  $p(t)$  of the temporal and  $S(\omega)$  of the spectral shape. It is thus vital to understand the underlying connections between the two and the electromagnetic field itself. Here I treat the field classically, which is sufficient to explain the notion of Fourier-limited single photons.

Omitting normalization constants, the temporal probability distribution  $p(t)$  is related to the electric field  $E(t)$  through

$$p(t) = |E(t)|^2. \quad (\text{A.35})$$

Analogously,

$$S(\omega) = |\tilde{E}(\omega)|^2 \quad (\text{A.36})$$

with the spectral probability distribution  $S(\omega)$  and the spectral representation  $\tilde{E}(\omega)$  of the electric field. The latter is defined through the Fourier transform of the electric field:

$$\tilde{E}(\omega) = \mathcal{F}\{E(t)\} \quad (\text{A.37})$$

$$= \int_{-\infty}^{\infty} E(t) e^{-i\omega t} dt \quad (\text{A.38})$$

It is practical to express the electric field through an amplitude function  $g(t)$  and a time-dependent phase  $\phi(t)$ :

$$E(t) = g(t) e^{i\phi(t)} \quad (\text{A.39})$$

This is a general form that does not put any restrictions on the electric-field function. Using the convolution theorem, we obtain the expression

$$\tilde{E}(\omega) = \mathcal{F}\{g(t)\} * \mathcal{F}\{e^{i\phi(t)}\} \quad (\text{A.40})$$

for the spectral field representation. At this point, we need another definition: a wave packet is called ‘‘Fourier limited’’ if its temporal and spectral probability distribution are related through the Fourier transform in the following way:

$$S(\omega - \omega_0) = \left| \mathcal{F}\left\{ \sqrt{p(t)} \right\} \right|^2 \quad (\text{A.41})$$

with carrier frequency  $\omega_0$ , which implies

$$S(\omega - \omega_0) = |\mathcal{F}\{g(t)\}|^2. \quad (\text{A.42})$$

From expression A.40, we can see that a wave packet is Fourier limited if and only if the phase function  $\phi(t)$  is of the form

$$\phi(t) = \omega_0 t + \phi_0. \quad (\text{A.43})$$

Other behaviors of the phase, such as e.g. a quadratic time-dependence due to a frequency chirp, will cause the photon not to fulfill the Fourier limit A.41. Hence there is no

way of transforming between the temporal and spectral probability distribution without knowledge of the phase function.

It is important to also mention the meaning of the phase offset  $\phi_0$ . As touched on in section 3.1.1, a single-photon state does not possess a well-defined phase, which means the phase offset  $\phi_0$  must be understood as a stochastic phase that is random from one experimental realization to the next. Thus the photonic phase is undefined in the sense of a measurable observable, although the individual wave packet has a specific, but unknown, phase offset. Practically, this means that a Fourier-limited photon is fully coherent with respect to itself, but not with respect to a photon emitted in a different experimental realization.

## A.6 Probability distribution of parasitic photons

In section 3.1.1, we elaborated on the effect of parasitic photons on the generation of single Raman photons; the emission of photons on the transition excited by the driving laser introduces decoherence and increases the time-bandwidth product of the Raman photon. Now we are interested in inferring the number of parasitic photons that were scattered before the Raman photon was detected. The *unconditional* probability distribution for the number of parasitic photons (the prior), i.e. when *not* detecting the Raman photon, is of the exponential form

$$P(n) = \frac{\bar{n}^n}{(\bar{n} + 1)^{n+1}} \quad (\text{A.44})$$

for which the expectation value is given by the branching fractions of the two transitions:  $\bar{n} = f_{i,r}/f_{i,g}$ .

As we have shown, the probability distribution of the Raman photon, *conditioned* on the emission of  $n$  parasitic photons, is given by

$$p(t|n) = \frac{1}{n!} \left( \frac{t}{\tau_{\text{ph}}} \right)^n \frac{1}{\tau_{\text{ph}}} e^{-t/\tau_{\text{ph}}} \Theta(t) \quad (\text{A.45})$$

with

$$\tau_{\text{ph}} = \left( \Gamma_i \frac{\Omega^2}{(2\Delta)^2 + \Gamma_i^2} \right)^{-1}. \quad (\text{A.46})$$

From this, we showed that the *unconditional* probability distribution of the Raman photon is

$$p(t) = \frac{1}{\bar{\tau}_{\text{ph}}} e^{-t/\bar{\tau}_{\text{ph}}} \Theta(t) \quad (\text{A.47})$$

with the prolonged photon duration

$$\bar{\tau}_{\text{ph}} = \tau_{\text{ph}} (\bar{n} + 1). \quad (\text{A.48})$$

We are now asking for the distribution  $P(n|t)$  of the number of parasitic photons *conditioned* on the detection of a Raman photon at time  $t$ . Following Bayesian inference (see section 2.1.3), we can express this distribution as

$$P(n|t) = \frac{p(t|n) \cdot P(n)}{p(t)}, \quad (\text{A.49})$$

which is readily evaluated to yield the Poisson distribution

$$P(n|t) = \frac{\bar{n}^n(t)}{n!} e^{-\bar{n}(t)}, \quad (\text{A.50})$$

for which the expectation value

$$\bar{n}(t) = \bar{n} \frac{t}{\tau} \quad (\text{A.51})$$

now depends on the detection time  $t$  of the Raman photon. It implies in particular that the later the Raman photon was detected, the larger the number of scattered parasitic photons (as expected intuitively). Hence temporally resolving the Raman photon provides information about the actual number of scattered parasitic photons.

## A.7 Estimating the multi-photon probability

In the context of the generation of single Raman photons, it is essential to estimate the multi-photon contribution. In our experimental situation, the emission of more than two photons is entirely negligible, and we will thus consider only single- and two-photon probabilities.

We define the two-photon probability  $p_2$  as the probability for the ion to emit a second photon conditioned on the detection of a first photon. The *unconditional* probability for a two-photon event is thus

$$p'_2 = p_1 \cdot p_2 \quad (\text{A.52})$$

with the single-photon probability  $p_1$ . The latter is simply given by the population of the initial state  $|r\rangle$  after state preparation.

As described in section 3.1.2, we make use of a Hanbury-Brown-Twiss (HBT) interferometer [157] in order to estimate the two-photon probability; after splitting up the light emitted by the ion, it is detected by two single-photon detectors. Coincidental detection events thus signal the presence of two photons. The probability for this kind of coincidence is given by

$$P_{\text{coinc}} = 2 \eta_1 \eta_2 p'_2 \quad (\text{A.53})$$

with the total detection efficiencies  $\eta_1$  and  $\eta_2$  for the two detectors. The factor 2 stems from the fact that the two photons are not temporally resolved, i.e. we cannot determine which detector was triggered by which photon. On the other hand, the probability for detection events *in a given order* from two successive experimental cycles amounts to

$$P_{\text{succ}} = \eta_1 \eta_2 p_1^2. \quad (\text{A.54})$$

A coincidence between the two detectors can also be mimicked by a dark-count event of one detector in conjunction with a real photon detection by the other. The probability for such a coincidence is

$$P_{\text{coinc}}^{(\text{dc})} = (d_1 \Delta T) (\eta_2 p_1) + (d_2 \Delta T) (\eta_1 p_1) \quad (\text{A.55})$$

with dark-count rates  $d_1$  and  $d_2$  of the two detectors and length  $\Delta T$  of the detection time window. Coincidences caused by dark-count events of both detectors, on the other hand, can be safely neglected.

The two-photon probability  $p_2$  can now be determined by comparing the number  $N_{\text{coinc}}$  of coincidental detection events to the number  $N_{\text{succ}}$  of detection events from successive experimental cycles:

$$\frac{N_{\text{coinc}}}{N_{\text{succ}}} = \frac{P_{\text{coinc}} + P_{\text{coinc}}^{(\text{dc})}}{P_{\text{succ}}} \quad (\text{A.56})$$

$$= \frac{1}{p_1} \left( 2p_2 + \frac{(\eta_1 d_2 + \eta_2 d_1) \Delta T}{\eta_1 \eta_2} \right) \quad (\text{A.57})$$

We solve this expression for  $p_2$ , yielding

$$p_2 = \frac{1}{2} \left( p_1 \frac{N_{\text{coinc}}}{N_{\text{succ}}} - \frac{(\eta_1 d_2 + \eta_2 d_1) \Delta T}{\eta_1 \eta_2} \right). \quad (\text{A.58})$$

The experimental data from the HBT measurement in section 3.1.2 is as follows:  $N_{\text{coinc}} = 12$ ,  $N_{\text{succ}} = 785$ ,  $p_1 = 0.69$ ,  $\eta_1 = 0.78\%$ ,  $\eta_2 = 0.51\%$ ,  $d_1 = 18\text{s}^{-1}$ ,  $d_2 = 13\text{s}^{-1}$ ,  $\Delta T = 0.8\text{ }\mu\text{s}$ . Assuming Poissonian errors on the numbers of detection events, we arrive at the two-photon probability  $p_2 = 0.33(15)\%$ .

## A.8 Maximum-likelihood estimation for a two-qubit system

In section 4.2.3, we introduced the analytic reconstruction of an unknown two-qubit quantum state  $\rho$ . Joint single-qubit measurements in conjugate bases allow to determine the 16 expectation values

$$w_{i,j} := \langle \sigma_i \otimes \sigma_j \rangle = \text{tr}(\sigma_i \otimes \sigma_j \rho), \quad (\text{A.59})$$

with the Pauli operators  $\{\sigma_{i=1,\dots,4}\} = \{\mathbb{1}, \sigma_x, \sigma_y, \sigma_z\}$  acting on the individual qubits. From the expectation values, we can directly infer the underlying quantum state:

$$\rho = \frac{1}{4} \sum_{i,j=1}^4 w_{i,j} \sigma_i \otimes \sigma_j \quad (\text{A.60})$$

As explained, the reconstruction from a set of experimentally approximated expectation values  $\{w_{i,j}\}$  is not guaranteed to yield a physical density matrix  $\rho$ , in that the matrix may contain eigenvalues (which represent probabilities) that do not lie in the unit interval  $[0, 1]$ .

Besides more recent approaches based on Quantum Bayesianism [193], the technique of maximum-likelihood estimation [175] has proven suitable for quantum-state reconstruction. In order to overcome the above problem, we ask for the particular physical quantum state which is most likely to have produced the experimentally determined data (the expectation values). This requires a numerical search over all physical states, which can be broken down into three steps:

1. Construct a likelihood function  $\mathcal{L}(\rho_{\text{cand}})$  which is a measure for how likely a physical candidate state  $\rho_{\text{cand}}$  will reproduce the measured expectation values  $\{w_{i,j}\}$ .
2. Parametrize the candidate state  $\rho_{\text{cand}}$  by a suitable set of parameters  $\{t_{i=1,\dots,16}\}$ .
3. Numerically maximize the likelihood function  $\mathcal{L}$  by varying the parameter set  $\{t_i\}$ . The final result is thus the quantum state corresponding to the optimized set of parameters.

### Constructing the likelihood function

The experimentally approximated expectation values  $\{w_{i,j}\}$  possess uncertainties  $\{\Delta w_{i,j}\}$  (standard deviations). If we assume these uncertainties to have Gaussian probability distributions, the probability that a candidate state  $\rho_{\text{cand}}$  produces the measured set of data is

$$P(\rho_{\text{cand}}) = \frac{1}{\mathcal{N}} \prod_{i,j=1}^4 \exp\left(-\frac{1}{2} \left(\frac{\text{tr}(\sigma_i \otimes \sigma_j \rho_{\text{cand}}) - w_{i,j}}{\Delta w_{i,j}}\right)^2\right) \quad (\text{A.61})$$

with some normalization constant  $\mathcal{N}$ . This is the quantity that we would like to maximize among all physical states  $\rho_{\text{cand}}$ . It is equivalent and at the same time numerically favorable to maximize not the value  $P(\rho_{\text{cand}})$  but its logarithm (omitting all unnecessary constants):

$$\mathcal{L}(\rho_{\text{cand}}) = - \sum_{i,j=1}^4 \left(\frac{\text{tr}(\sigma_i \otimes \sigma_j \rho_{\text{cand}}) - w_{i,j}}{\Delta w_{i,j}}\right)^2 \quad (\text{A.62})$$

### Parametrizing the candidate state

The important requirement on a physical density matrix  $\rho$ , besides normalization, is positive semi-definiteness, which ensures nonnegative eigenvalues. Such a matrix can always be expressed in terms of its Cholesky decomposition,

$$\rho = T T^\dagger, \quad (\text{A.63})$$

where  $T$  is a lower triangular matrix with a real-valued diagonal. This matrix  $T$  can be parametrized through a set of 16 real numbers  $\{t_{i=1,\dots,16}\}$ :

$$T(\{t_i\}) = \begin{pmatrix} t_1 & 0 & 0 & 0 \\ t_5 + it_6 & t_2 & 0 & 0 \\ t_7 + it_8 & t_9 + it_{10} & t_3 & 0 \\ t_{11} + it_{12} & t_{13} + it_{14} & t_{15} + it_{16} & t_4 \end{pmatrix} \quad (\text{A.64})$$

Followed by normalization, any set of real numbers  $\{t_i\}$  (except all zeros) yields a physical density matrix

$$\rho(\{t_i\}) = \frac{T T^\dagger}{\text{tr}(T T^\dagger)}. \quad (\text{A.65})$$

**Maximizing the likelihood function**

After parametrizing the candidate state  $\rho_{\text{cand}}$ , we can numerically maximize the likelihood function  $\mathcal{L}(\{t_i\})$ . A possible choice for achieving this is the MATLAB function `fminsearch`. However, a search with 16 independent parameters requires an initial guess which is sufficiently close to the global maximum lest the algorithm converge to some local maximum. Such is provided by the analytically reconstructed density matrix from eqn. A.60. However, should this state happen to have negative eigenvalues, it cannot be decomposed into a lower triangular matrix from which the initial set of parameters  $\{t_i\}$  can be extracted. We circumvent this issue by first expressing the density matrix in its eigenbasis. Setting any negative eigenvalue to zero and transforming back to the computational basis thus yields a positive semi-definite matrix (although not necessarily of trace 1). This modified matrix is usually still sufficiently close to the original one such that decomposing it into the set  $\{t_i\}$  provides a good initial guess for the numerical search.

Following eqn. A.65, the optimized set  $\{t_i\}$  yields the particular quantum state among all physical states which is most likely to reproduce the experimental data.

# Journal publications

The work presented in this thesis gave rise to the following journal publications:

*Experimental protocol for high-fidelity heralded photon-to-atom quantum state transfer*

C. Kurz, M. Schug, P. Eich, J. Huwer, P. Müller, J. Eschner  
Nat. Commun. **5**, 5527 (2014)

*Quantum interference in the absorption and emission of single photons by a single ion*

M. Schug, C. Kurz, P. Eich, J. Huwer, P. Müller, J. Eschner  
Phys. Rev. A **90**, 023829 (2014)

*Heralded photonic interaction between distant single ions*

M. Schug, J. Huwer, C. Kurz, P. Müller, J. Eschner  
Phys. Rev. Lett. **110**, 213603 (2013)

*A high-rate source for single photons in a pure quantum state*

C. Kurz, J. Huwer, M. Schug, P. Müller, J. Eschner  
New J. Phys. **15**, 055005 (2013)

Manuscripts in preparation:

*Programmable ion-photon quantum interface*

C. Kurz, P. Eich, M. Schug, J. Eschner



# Bibliography

- [1] M. A. Nielsen, I. L. Chuang. *Quantum Computation and Quantum Information*. Cambridge University Press (2000).
- [2] C. E. Shannon. *A Mathematical Theory of Communication*. Bell Labs Techn. J. **27**, 379–423 (1948).
- [3] A. Goel. *Computer Fundamentals*. Pearson Education (2010).
- [4] D. Deutsch. *Quantum Theory, the Church-Turing Principle and the Universal Quantum Computer*. Proc. R. Soc. Lond. A **400**, 97 (1985).
- [5] P. W. Shor. *Algorithms for quantum computation: discrete logarithms and factoring*. Proceedings of the 35th Annual Symposium on Foundations of Computer Science, IEEE Computer Society Press (1994).
- [6] D. Deutsch, R. Jozsa. *Rapid Solution of Problems by Quantum Computation*. Proc. R. Soc. Lond. A **439**, 553 (1992).
- [7] G. Brassard, P. Høyer. *An exact quantum polynomial-time algorithm for Simon's problem*. Proceedings of the Fifth Israeli Symposium on Theory of Computing and Systems, IEEE Computer Society Press (1997).
- [8] L. K. Grover. *A fast quantum mechanical algorithm for database search*. Proceedings of the 28th Annual ACM Symposium on the Theory of Computing, ACM (1996).
- [9] A. M. Childs, R. Cleve, E. Deotto, E. Farhi, S. Gutmann, D. A. Spielman. *Exponential algorithmic speedup by quantum walk*. Proceedings of the 35th ACM Symposium on Theory of Computing, ACM (2003).
- [10] T. H. Johnson, S. R. Clark, D. Jaksch. *What is a quantum simulator?* EPJ Quantum Technology **1**, 10 (2014).
- [11] A. L. Fetter, J. D. Walecka. *Quantum Theory of Many-Particle Systems*. New York: Dover (2003).
- [12] R. P. Feynman. *Simulating Physics with Computers*. Int. J. Theor. Phys. **21**, 467–488 (1982).

- [13] D. Deutsch. *Quantum Computational Networks*. Proc. R. Soc. Lond. A **425**, 73 (1989).
- [14] E. Knill, R. Laflamme, G. J. Milburn. *A scheme for efficient quantum computation with linear optics*. Nature **409**, 46–52 (2001).
- [15] R. Raussendorf, H. J. Briegel. *A One-Way Quantum Computer*. Phys. Rev. Lett. **86**, 5188 (2001).
- [16] E. Farhi, J. Goldstone, S. Gutmann, J. Lapan, A. Lundgren, D. Preda. *A Quantum Adiabatic Evolution Algorithm Applied to Random Instances of an NP-Complete Problem*. Science **292**, 472–475 (2001).
- [17] D. Aharonov, W. van Dam, J. Kempe, Z. Landau, S. Lloyd, O. Regev. *Adiabatic Quantum Computation is Equivalent to Standard Quantum Computation*. SIAM J. Comput. **37**, 166–194 (2007).
- [18] J.-W. Pan, Z.-B. Chen, C.-Y. Lu, H. Weinfurter, A. Zeilinger, M. Zukowski. *Multi-photon entanglement and interferometry*. Rev. Mod. Phys. **84**, 777 (2012).
- [19] I. Marzoli, P. Tombesi, G. Ciaramicoli, G. Werth, P. Bushev, S. Stahl, F. Schmidt-Kaler, M. Hellwig, C. Henkel, G. Marx, I. Jex, E. Stachowska, G. Szawiola, A. Walaszyk. *Experimental and theoretical challenges for the trapped electron quantum computer*. J. Phys. B **42**, 154010 (2009).
- [20] H.-J. Briegel, T. Calarco, D. Jaksch, J. I. Cirac, P. Zoller. *Quantum computing with neutral atoms*. J. Mod. Opt. **47**, 415–451 (2000).
- [21] H. J. Kimble. *The quantum internet*. Nature **453**, 1023–1030 (2008).
- [22] J. I. Cirac, P. Zoller. *A scalable quantum computer with ions in an array of microtraps*. Nature **404**, 579–581 (2000).
- [23] H. Häffner, C. F. Roos, R. Blatt. *Quantum computing with trapped ions*. Phys. Rep. **469**, 155–203 (2008).
- [24] Y. Makhlin, G. Schön, A. Shnirman. *Quantum-state engineering with Josephson-junction devices*. Rev. Mod. Phys. **73**, 357 (2001).
- [25] J. Clarke, F. K. Wilhelm. *Superconducting quantum bits*. Nature **453**, 1031–1042 (2008).
- [26] R. Hanson, L. P. Kouwenhoven, J. R. Petta, S. Tarucha, L. M. K. Vandersypen. *Spins in few-electron quantum dots*. Rev. Mod. Phys. **79**, 1217 (2007).
- [27] R. Hanson, D. D. Awschalom. *Coherent manipulation of single spins in semiconductors*. Nature **453**, 1043–1049 (2008).

- [28] B. E. Kane. *A silicon-based nuclear spin quantum computer*. Nature **393**, 133–137 (1998).
- [29] L. M. K. Vandersypen, M. Steffen, G. Breyta, C. S. Yannoni, M. H. Sherwood, I. L. Chuang. *Experimental realization of Shor’s quantum factoring algorithm using nuclear magnetic resonance*. Nature **414**, 883–887 (2001).
- [30] D. P. DiVincenzo. *The Physical Implementation of Quantum Computation*. Fortschr. Phys. **48**, 771–783 (2000).
- [31] P. Zoller, T. Beth, D. Binosi, R. Blatt, H. Briegel, D. Bruss, T. Calarco, J. I. Cirac, D. Deutsch, J. Eisert, A. Ekert, C. Fabre, N. Gisin, P. Grangiere, M. Grassl, S. Haroche, A. Imamoglu, A. Karlson, J. Kempe, L. Kouwenhoven, S. Kröll, G. Leuchs, M. Lewenstein, D. Loss, N. Lütkenhaus, S. Massar, J. E. Mooij, M. B. Plenio, E. Polzik, S. Popescu, G. Rempe, A. Sergienko, D. Suter, J. Twamley, G. Wendin, R. Werner, A. Winter, J. Wrachtrup, A. Zeilinger. *Quantum information processing and communication*. Eur. Phys. J. D **36**, 203–228 (2005).
- [32] P. Schindler, D. Nigg, T. Monz, J. T. Barreiro, E. Martinez, S. X. Wang, S. Quint, M. F. Brandl, V. Nebendahl, C. F. Roos, M. Chwalla, M. Hennrich, R. Blatt. *A quantum information processor with trapped ions*. New J. Phys. **15**, 123012 (2013).
- [33] D. Leibfried, R. Blatt, C. Monroe, D. Wineland. *Quantum dynamics of single trapped ions*. Rev. Mod. Phys. **75**, 281 (2003).
- [34] F. Diedrich, J. C. Bergquist, W. M. Itano, D. J. Wineland. *Laser Cooling to the Zero-Point Energy of Motion*. Phys. Rev. Lett. **62**, 403 (1989).
- [35] C. Langer, R. Ozeri, J. D. Jost, J. Chiaverini, B. DeMarco, A. Ben-Kish, R. B. Blakestad, J. Britton, D. B. Hume, W. M. Itano, D. Leibfried, R. Reichle, T. Rosenband, T. Schaetz, P. O. Schmidt, D. J. Wineland. *Long-Lived Qubit Memory Using Atomic Ions*. Phys. Rev. Lett. **95**, 060502 (2005).
- [36] H. C. Nägerl, D. Leibfried, H. Rohde, G. Thalhammer, J. Eschner, F. Schmidt-Kaler, R. Blatt. *Laser addressing of individual ions in a linear ion trap*. Phys. Rev. A **60**, 145 (1999).
- [37] F. Mintert, C. Wunderlich. *Ion-Trap Quantum Logic Using Long-Wavelength Radiation*. Phys. Rev. Lett. **87**, 257904 (2001).
- [38] D. Leibfried, B. DeMarco, V. Meyer, D. Lucas, M. Barrett, J. Britton, W. M. Itano, B. Jelenković, C. Langer, T. Rosenband, D. J. Wineland. *Experimental demonstration of a robust, high-fidelity geometric two ion-qubit phase gate*. Nature **422**, 412–415 (2003).
- [39] J. Benhelm, G. Kirchmair, C. F. Roos, R. Blatt. *Towards fault-tolerant quantum computing with trapped ions*. Nat. Phys. **4**, 463–466 (2008).

- [40] M. Riebe, K. Kim, P. Schindler, T. Monz, P. O. Schmidt, T. K. Körber, W. Hänsel, H. Häffner, C. F. Roos, R. Blatt. *Process Tomography of Ion Trap Quantum Gates*. Phys. Rev. Lett. **97**, 220407 (2006).
- [41] C. Monroe, D. M. Meekhof, B. E. King, W. M. Itano, D. J. Wineland. *Demonstration of a Fundamental Quantum Logic Gate*. Phys. Rev. Lett. **75**, 4714 (1995).
- [42] F. Schmidt-Kaler, H. Häffner, M. Riebe, S. Gulde, G. P. T. Lancaster, T. Deuschle, C. Becher, C. F. Roos, J. Eschner, R. Blatt. *Realization of the Cirac-Zoller controlled-NOT quantum gate*. Nature **422**, 408–411 (2003).
- [43] T. Monz, K. Kim, W. Hänsel, M. Riebe, A. S. Villar, P. Schindler, M. Chwalla, M. Hennrich, R. Blatt. *Realization of the Quantum Toffoli Gate with Trapped Ions*. Phys. Rev. Lett. **102**, 040501 (2009).
- [44] K. Mølmer, A. Sørensen. *Multiparticle Entanglement of Hot Trapped Ions*. Phys. Rev. Lett. **82**, 1835 (1999).
- [45] A. Sørensen, K. Mølmer. *Quantum Computation with Ions in Thermal Motion*. Phys. Rev. Lett. **82**, 1971 (1999).
- [46] T. P. Harty, D. T. C. Allcock, C. J. Ballance, L. Guidoni, H. A. Janacek, N. M. Linke, D. N. Stacey, D. M. Lucas. *High-Fidelity Preparation, Gates, Memory, and Readout of a Trapped-Ion Quantum Bit*. Phys. Rev. Lett. **113**, 220501 (2014).
- [47] F. Schmidt-Kaler, S. Gulde, M. Riebe, T. Deuschle, A. Kreuter, G. Lancaster, C. Becher, J. Eschner, H. Häffner, R. Blatt. *The coherence of qubits based on single  $Ca^+$  ions*. J. Phys. B **36**, 623 (2003).
- [48] C. Roos, T. Zeiger, H. Rohde, H. C. Nägerl, J. Eschner, D. Leibfried, F. Schmidt-Kaler, R. Blatt. *Quantum State Engineering on an Optical Transition and Decoherence in a Paul Trap*. Phys. Rev. Lett. **83**, 4713 (1999).
- [49] P. W. Shor. *Scheme for reducing decoherence in quantum computer memory*. Phys. Rev. A **52**, R2493 (1995).
- [50] A. M. Steane. *Error Correcting Codes in Quantum Theory*. Phys. Rev. Lett. **77**, 793 (1996).
- [51] J. Chiaverini, D. Leibfried, T. Schaetz, M. D. Barrett, R. B. Blakestad, J. Britton, W. M. Itano, J. D. Jost, E. Knill, C. Langer, R. Ozeri, D. J. Wineland. *Realization of quantum error correction*. Nature **432**, 602–605 (2004).
- [52] P. Schindler, J. T. Barreiro, T. Monz, V. Nebendahl, D. Nigg, M. Chwalla, M. Hennrich, R. Blatt. *Experimental Repetitive Quantum Error Correction*. Science **332**, 1059–1061 (2011).

- [53] S. Gulde, M. Riebe, G. P. T. Lancaster, C. Becher, J. Eschner, H. Häffner, F. Schmidt-Kaler, I. L. Chuang, R. Blatt. *Implementation of the Deutsch-Jozsa algorithm on an ion-trap quantum computer*. Nature **421**, 48–50 (2003).
- [54] J. Chiaverini, J. Britton, D. Leibfried, E. Knill, M. D. Barrett, R. B. Blakestad, W. M. Itano, J. D. Jost, C. Langer, R. Ozeri, T. Schaetz, D. J. Wineland. *Implementation of the Semiclassical Quantum Fourier Transform in a Scalable System*. Science **308**, 997–1000 (2005).
- [55] R. Islam, C. Senko, W. C. Campbell, S. Korenblit, J. Smith, A. Lee, E. E. Edwards, C.-C. J. Wang, J. K. Freericks, C. Monroe. *Emergence and Frustration of Magnetism with Variable-Range Interactions in a Quantum Simulator*. Science **340**, 583–587 (2013).
- [56] R. Blatt, C. F. Roos. *Quantum simulations with trapped ions*. Nat. Phys. **8**, 277–284 (2012).
- [57] D. Kielpinski, C. Monroe, D. J. Wineland. *Architecture for a large-scale ion-trap quantum computer*. Nature **417**, 709–711 (2002).
- [58] R. Bowler, J. Gaebler, Y. Lin, T. R. Tan, D. Hanneke, J. D. Jost, J. P. Home, D. Leibfried, D. J. Wineland. *Coherent Diabatic Ion Transport and Separation in a Multizone Trap Array*. Phys. Rev. Lett. **109**, 080502 (2012).
- [59] T. Ruster, C. Warschburger, H. Kaufmann, C. T. Schmiegelow, A. Walther, M. Hettich, A. Pfister, V. Kaushal, F. Schmidt-Kaler, U. G. Poschinger. *Experimental realization of fast ion separation in segmented Paul traps*. Phys. Rev. A **90**, 033410 (2014).
- [60] L. Deslauriers, S. Olmschenk, D. Stick, W. K. Hensinger, J. Sterk, C. Monroe. *Scaling and Suppression of Anomalous Heating in Ion Traps*. Phys. Rev. Lett. **97**, 103007 (2006).
- [61] L.-M. Duan, C. Monroe. *Quantum networks with trapped ions*. Rev. Mod. Phys. **82**, 1209 (2010).
- [62] C. Cabrillo, J. I. Cirac, P. García-Fernández, P. Zoller. *Creation of entangled states of distant atoms by interference*. Phys. Rev. A **59**, 1025 (1999).
- [63] L. Slodička, G. Hétet, N. Röck, P. Schindler, M. Hennrich, R. Blatt. *Atom-Atom Entanglement by Single-Photon Detection*. Phys. Rev. Lett. **110**, 083603 (2013).
- [64] C. Simon, W. T. M. Irvine. *Robust Long-Distance Entanglement and a Loophole-Free Bell Test with Ions and Photons*. Phys. Rev. Lett. **91**, 110405 (2003).
- [65] D. L. Moehring, P. Maunz, S. Olmschenk, K. C. Younge, D. N. Matsukevich, L.-M. Duan, C. Monroe. *Entanglement of single-atom quantum bits at a distance*. Nature **449**, 68–71 (2007).

- [66] J. Hofmann, M. Krug, N. Ortegel, L. Gérard, M. Weber, W. Rosenfeld, H. Weinfurter. *Heralded Entanglement Between Widely Separated Atoms*. *Science* **337**, 72–75 (2012).
- [67] J. I. Cirac, P. Zoller, H. J. Kimble, H. Mabuchi. *Quantum State Transfer and Entanglement Distribution among Distant Nodes in a Quantum Network*. *Phys. Rev. Lett.* **78**, 3221 (1997).
- [68] S. Ritter, C. Nölleke, C. Hahn, A. Reiserer, A. Neuzner, M. Uphoff, M. Mücke, E. Figueroa, J. Bochmann, G. Rempe. *An Elementary Quantum Network of Single Atoms in Optical Cavities*. *Nature* **484**, 195–200 (2012).
- [69] P. G. Kwiat, K. Mattle, H. Weinfurter, A. Zeilinger, A. V. Sergienko, Y. Shih. *New High-Intensity Source of Polarization-Entangled Photon Pairs*. *Phys. Rev. Lett.* **75**, 4337 (1995).
- [70] A. V. Burlakov, M. V. Chekhova, O. A. Karabutova, S. P. Kulik. *Collinear two-photon state with spectral properties of type-I and polarization properties of type-II spontaneous parametric down-conversion: Preparation and testing*. *Phys. Rev. A* **64**, 041803(R) (2001).
- [71] S. Lloyd, M. S. Shahriar, J. H. Shapiro, P. R. Hemmer. *Long Distance, Unconditional Teleportation of Atomic States via Complete Bell State Measurements*. *Phys. Rev. Lett.* **87**, 167903 (2001).
- [72] N. Sangouard, J.-D. Bancal, P. Müller, J. Ghosh, J. Eschner. *Heralded mapping of photonic entanglement into single atoms in free space: proposal for a loophole-free Bell test*. *New J. Phys.* **15**, 085004 (2013).
- [73] P. Müller, J. Eschner. *Single calcium-40 ion as quantum memory for photon polarization: a case study*. *Appl. Phys. B* **114**, 303–306 (2014).
- [74] H.-J. Briegel, W. Dür, J. I. Cirac, P. Zoller. *Quantum Repeaters: The Role of Imperfect Local Operations in Quantum Communication*. *Phys. Rev. Lett.* **81**, 5932 (1998).
- [75] N. Gisin, G. Ribordy, W. Tittel, H. Zbinden. *Quantum cryptography*. *Rev. Mod. Phys.* **74**, 145 (2002).
- [76] N. Gisin, R. Thew. *Quantum communication*. *Nat. Photon.* **1**, 165–171 (2007).
- [77] C. H. Bennett, G. Brassard, C. Crépeau, R. Jozsa, A. Peres, W. K. Wootters. *Teleporting an unknown quantum state via dual classical and Einstein-Podolsky-Rosen channels*. *Phys. Rev. Lett.* **70**, 1895–1899 (1993).
- [78] M. Riebe, H. Häffner, C. F. Roos, W. Hänsel, J. Benhelm, G. P. T. Lancaster, T. W. Körber, C. Becher, F. Schmidt-Kaler, D. F. V. James, R. Blatt. *Deterministic quantum teleportation with atoms*. *Nature* **429**, 734–737 (2004).

- [79] M. D. Barrett, J. Chiaverini, T. Schaetz, J. Britton, W. M. Itano, J. D. Jost, E. Knill, C. Langer, D. Leibfried, R. Ozeri, D. J. Wineland. *Deterministic quantum teleportation of atomic qubits*. Nature **429**, 737–739 (2004).
- [80] S. Olmschenk, D. N. Matsukevich, P. Maunz, D. Hayes, L.-M. Duan, C. Monroe. *Quantum Teleportation Between Distant Matter Qubits*. Science **323**, 486–489 (2009).
- [81] A. D. Boozer, A. Boca, R. Miller, T. E. Northup, H. J. Kimble. *Reversible State Transfer between Light and a Single Trapped Atom*. Phys. Rev. Lett. **98**, 193601 (2007).
- [82] T. Wilk, S. C. Webster, A. Kuhn, G. Rempe. *Single-Atom Single-Photon Quantum Interface*. Science **317**, 488–490 (2007).
- [83] M. K. Tey, Z. Chen, S. A. Aljunid, B. Chng, F. Huber, G. Maslennikov, C. Kurtsiefer. *Strong interaction between light and a single trapped atom without the need for a cavity*. Nat. Phys. **4**, 924–927 (2008).
- [84] S. Gerber, D. Rotter, M. Hennrich, R. Blatt, F. Rohde, C. Schuck, M. Almdendros, R. Gehr, F. Dubin, J. Eschner. *Quantum interference from remotely trapped ions*. New J. Phys. **11**, 013032 (2009).
- [85] G. Vittorini, D. Hucul, I. V. Inlek, C. Crocker, C. Monroe. *Entanglement of distinguishable quantum memories*. Phys. Rev. A **90**, 040302(R) (2014).
- [86] R. Maiwald, D. Leibfried, J. Britton, J. C. Bergquist, G. Leuchs, D. J. Wineland. *Stylus ion trap for enhanced access and sensing*. Nat. Phys. **5**, 551–554 (2009).
- [87] M. Fischer, M. Bader, R. Maiwald, A. Golla, M. Sondermann, G. Leuchs. *Efficient saturation of an ion in free space*. Appl. Phys. B **117**, 797–801 (2014).
- [88] C. Kurz, J. Huwer, M. Schug, P. Müller, J. Eschner. *A high-rate source for single photons in a pure quantum state*. New J. Phys. **15**, 055005 (2013).
- [89] M. Schug, C. Kurz, P. Eich, J. Huwer, P. Müller, J. Eschner. *Quantum interference in the absorption and emission of single photons by a single ion*. Phys. Rev. A **90**, 023829 (2014).
- [90] C. Kurz, M. Schug, P. Eich, J. Huwer, P. Müller, J. Eschner. *Experimental protocol for high-fidelity heralded photon-to-atom quantum state transfer*. Nat. Commun. **5**, 5527 (2014).
- [91] H. P. Specht, C. Nölleke, A. Reiserer, M. Uphoff, E. Figueroa, S. Ritter, G. Rempe. *A single-atom quantum memory*. Nature **473**, 190–193 (2011).
- [92] H. Tanji, S. Ghosh, J. Simon, B. Bloom, V. Vuletić. *Heralded Single-Magnon Quantum Memory for Photon Polarization States*. Phys. Rev. Lett. **103**, 043601 (2009).

- [93] M. Schug. *Single photons from single ions: quantum interference and distant ion interaction*. Ph.D. thesis, Universität des Saarlandes (2015).
- [94] J. Huwer. *Experimental tools for quantum networking operations with single photons and single ions*. Ph.D. thesis, Universität des Saarlandes and ICFO – The Institute of Photonic Sciences (2013).
- [95] T. W. Hänsch, A. L. Schawlow. *Cooling of gases by laser radiation*. Opt. Commun. **13**, 68–69 (1975).
- [96] S. Stenholm. *The semiclassical theory of laser cooling*. Rev. Mod. Phys. **58**, 699 (1986).
- [97] J. Eschner, G. Morigi, F. Schmidt-Kaler, R. Blatt. *Laser cooling of trapped ions*. J. Opt. Soc. Am. **20**, 1003–1015 (2003).
- [98] D. J. Wineland, R. E. Drullinger, F. L. Walls. *Radiation-Pressure Cooling of Bound Resonant Absorbers*. Phys. Rev. Lett. **40**, 1639 (1978).
- [99] W. Neuhauser, M. Hohenstatt, P. Toschek, H. Dehmelt. *Optical-Sideband Cooling of Visible Atom Cloud Confined in Parabolic Well*. Phys. Rev. Lett. **41**, 233 (1978).
- [100] P. O. Schmidt, T. Rosenband, C. Langer, W. M. Itano, J. C. Bergquist, D. J. Wineland. *Spectroscopy Using Quantum Logic*. Science **309**, 749–752 (2005).
- [101] T. Rosenband, D. B. Hume, P. O. Schmidt, C. W. Chou, A. Brusch, L. Lorini, W. H. Oskay, R. E. Drullinger, T. M. Fortier, J. E. Stalnaker, S. A. Diddams, W. C. Swann, N. R. Newbury, W. M. Itano, D. J. Wineland, J. C. Bergquist. *Frequency Ratio of  $Al^+$  and  $Hg^+$  Single-Ion Optical Clocks; Metrology at the 17th Decimal Place*. Science **319**, 1808–1812 (2008).
- [102] J. I. Cirac, P. Zoller. *Quantum Computations with Cold Trapped Ions*. Phys. Rev. Lett. **74**, 4091 (1995).
- [103] A. R. Calderbank, P. W. Shor. *Good quantum error-correcting codes exist*. Phys. Rev. A **54**, 1098 (1996).
- [104] R. Blatt, D. Wineland. *Entangled states of trapped atomic ions*. Nature **453**, 1008–1015 (2008).
- [105] W. Paul. *Quadrupole Mass Filter*. Z. Naturforsch. **A8**, 448 (1953).
- [106] W. Neuhauser, M. Hohenstatt, P. E. Toschek, H. Dehmelt. *Localized visible  $Ba^+$  mono-ion oscillator*. Phys. Rev. A **22**, 1137 (1980).
- [107] C. F. Roos. *Controlling the quantum state of trapped ions*. Ph.D. thesis, Universität Innsbruck (2000).

- [108] M. Welling, H. A. Schuessler, R. I. Thompson, H. Walther. *Ion/molecule reactions, mass spectrometry and optical spectroscopy in a linear ion trap*. Int. J. Mass Spectrom. **172**, 95–114 (1998).
- [109] P. H. Dawson. *Quadrupole Mass Spectrometry and Its Applications*. American Institute of Physics (1978).
- [110] P. K. Ghosh. *Ion Traps*. Oxford University Press (1995).
- [111] S. T. Gulde. *Experimental Realization of Quantum Gates and the Deutsch-Josza Algorithm with Trapped  $^{40}\text{Ca}^+$  ions*. Ph.D. thesis, Universität Innsbruck (200302).
- [112] C. Schuck. *Interfacing single ions and single photons for quantum networks*. Ph.D. thesis, ICFO – The Institute of Photonic Sciences (2009).
- [113] S. Earnshaw. *On the Nature of the Molecular Forces which Regulate the Constitution of the Luminiferous Ether*. Trans. Camb. Phil. Soc. **7**, 97 (1842).
- [114] H. G. Dehmelt. *Radiofrequency spectroscopy of stored ions I: Storage*. Adv. At. Mol. Phys. **3**, 53 (1967).
- [115] D. J. Berkeland, J. D. Miller, J. C. Bergquist, W. M. Itano, D. J. Wineland. *Minimization of ion micromotion in a Paul trap*. J. Appl. Phys. **83**, 5025 (1998).
- [116] M. Fox. *Quantum Optics*. Oxford University Press (2006).
- [117] J. Javanainen, S. Stenholm. *Laser Cooling of Trapped Particles III: The Lamb-Dicke Limit*. Appl. Phys. **24**, 151–162 (1981).
- [118] J. Mizrahi, C. Senko, B. Neyenhuis, K. G. Johnson, W. C. Campbell, C. W. S. Conover, C. Monroe. *Ultrafast Spin-Motion Entanglement and Interferometry with a Single Atom*. Phys. Rev. Lett. **110**, 203001 (2013).
- [119] M. O. Scully, M. S. Zubairy. *Quantum optics*. Cambridge University Press (1997).
- [120] L. Boltzmann. *Lectures on gas theory*. University of California Press (1964).
- [121] J. Jin, D. A. Church. *Precision lifetimes for the  $\text{Ca}^+4p^2P$  levels: Experiment challenges theory at the 1 % level*. Phys. Rev. Lett. **70**, 3213 (1993).
- [122] A. Kreuter, C. Becher, G. P. T. Lancaster, A. B. Mundt, C. Russo, H. Häffner, C. Roos, W. Hänsel, F. Schmidt-Kaler, R. Blatt, M. S. Safronova. *Experimental and theoretical study of the  $3d^2D$ -level lifetimes of  $^{40}\text{Ca}^+$* . Phys. Rev. A **71**, 032504 (2005).
- [123] M. Ramm, T. Pruttivarasin, M. Kokish, I. Talukdar, H. Häffner. *Precision Measurement Method for Branching Fractions of Excited  $P_{1/2}$  States Applied to  $^{40}\text{Ca}^+$* . Phys. Rev. Lett. **111**, 023004 (2013).

- [124] M. Chwalla. *Precision spectroscopy with  $^{40}\text{Ca}^+$  ions in a Paul trap*. Ph.D. thesis, Universität Innsbruck (2009).
- [125] K. Matsubara, K. Hayasaka, Y. Li, H. Ito, S. Nagano, M. Kajita, M. Hosokawa. *Frequency Measurement of the Optical Clock Transition of  $^{40}\text{Ca}^+$  Ions with an Uncertainty of  $10^{-14}$  Level*. Appl. Phys. Express **1**, 067011 (2008).
- [126] S. Haze, T. Ohno, K. Toyoda, S. Urabe. *Measurement of the coherence time of the ground-state Zeeman states in  $^{40}\text{Ca}^+$* . Appl. Phys. B **105**, 761–765 (2011).
- [127] F. Rohde. *Remote ion traps for quantum networking: Two-photon interference and correlations*. Ph.D. thesis, ICFO – The Institute of Photonic Sciences (2009).
- [128] B. H. Rohde. *Experimente zur Quanteninformatonsverarbeitung in einer linearen Ionenfalle*. Ph.D. thesis, Universität Innsbruck (2001).
- [129] L. Ricci, M. Weidemüller, T. Esslinger, A. Hemmerich, C. Zimmermann, V. Vuletić, W. König, T. W. Hänsch. *A compact grating-stabilized diode laser system for atomic physics*. Opt. Commun. **117**, 541–549 (1995).
- [130] F. Rohde, M. Almendros, C. Schuck, J. Huwer, M. Hennrich, J. Eschner. *A diode laser stabilization scheme for  $^{40}\text{Ca}^+$  single-ion spectroscopy*. J. Phys. B **43**, 115401 (2010).
- [131] M. Almendros. *Towards Long-Distance Quantum Communication*. Ph.D. thesis, ICFO – The Institute of Photonic Sciences (2009).
- [132] R. W. P. Drever, J. L. Hall, F. V. Kowalski, J. Hough, G. M. Ford, A. J. Munley, H. Ward. *Laser Phase and Frequency Stabilization Using an Optical Resonator*. Appl. Phys. B **31**, 97–105 (1983).
- [133] A. D. Ludlow, X. Huang, M. Notcutt, T. Zanon-Willette, S. M. Foreman, M. M. Boyd, S. Blatt, J. Ye. *Compact, thermal-noise-limited optical cavity for diode laser stabilization at  $1 \times 10^{-15}$* . Opt. Lett. **32**, 641–643 (2007).
- [134] J. Alnis, A. Matveev, N. Kolachevsky, T. Udem, T. W. Hänsch. *Subhertz linewidth diode lasers by stabilization to vibrationally and thermally compensated ultralow-expansion glass Fabry-Pérot cavities*. Phys. Rev. A **77**, 053809 (2008).
- [135] J. Neyman. *Outline of a Theory of Statistical Estimation Based on the Classical Theory of Probability*. Phil. Trans. **236**, 333–380 (1937).
- [136] C. Howson, P. Urbach. *Scientific Reasoning: The Bayesian Approach*. Open Court Publishing Company (2005).
- [137] M. Kreis. *Magnetfeldstabilisierung für Hochpräzise Einzelatom Spektroskopie*. Master’s thesis, Universität des Saarlandes (2014).

- [138] N. F. Ramsey. *A Molecular Beam Resonance Method with Separated Oscillating Fields*. Phys. Rev. **78**, 695 (1950).
- [139] B. Odom, D. Hanneke, B. D’Urso, G. Gabrielse. *New Measurement of the Electron Magnetic Moment Using a One-Electron Quantum Cyclotron*. Phys. Rev. Lett. **97**, 030801 (2006).
- [140] J. J. Sakurai. *Modern Quantum Mechanics, Revised Edition*. Pearson Education (1994).
- [141] L. Viola, S. Lloyd. *Dynamical suppression of decoherence in two-state quantum systems*. Phys. Rev. A **58**, 2733 (1998).
- [142] M. J. Biercuk, H. Uys, A. P. VanDevender, N. Shiga, W. M. Itano, J. J. Bollinger. *Experimental Uhrig dynamical decoupling using trapped ions*. Phys. Rev. A **79**, 062324 (2009).
- [143] M. Schubert, I. Siemers, R. Blatt, W. Neuhauser, P. E. Toschek. *Transient internal dynamics of a multilevel ion*. Phys. Rev. A **52**, 2994 (1995).
- [144] D. Hucul, I. V. Inlek, G. Vittorini, C. Crocker, S. Debnath, S. M. Clark, C. Monroe. *Modular entanglement of atomic qubits using photons and phonons*. Nat. Phys. **11**, 37–42 (2014).
- [145] J. McKeever, A. Boca, A. D. Boozer, R. Miller, J. R. Buck, A. Kuzmich, H. J. Kimble. *Deterministic Generation of Single Photons from One Atom Trapped in a Cavity*. Science **303**, 1992–1994 (2004).
- [146] M. Keller, B. Lange, K. Hayasaka, W. Lange, H. Walther. *Continuous generation of single photons with controlled waveform in an ion-trap cavity system*. Nature **431**, 1075–1078 (2004).
- [147] M. Hijlkema, B. Weber, H. P. Specht, S. C. Webster, A. Kuhn, G. Rempe. *A single-photon server with just one atom*. Nat. Phys. **3**, 253–255 (2007).
- [148] M. Almendros, J. Huwer, N. Piro, F. Rohde, C. Schuck, M. Hennrich, F. Dubin, J. Eschner. *Bandwidth-Tunable Single-Photon Source in an Ion-Trap Quantum Network*. Phys. Rev. Lett. **103**, 213601 (2009).
- [149] X.-S. Ma, T. Herbst, T. Scheidl, D. Wang, S. Kropatschek, W. Naylor, B. Wittmann, A. Mech, J. Kofler, E. Anisimova, V. Makarov, T. Jennewein, R. Ursin, A. Zeilinger. *Quantum teleportation over 143 kilometres using active feed-forward*. Nature **489**, 269–273 (2012).
- [150] C. Nölleke, A. Neuzner, A. Reiserer, C. Hahn, G. Rempe, S. Ritter. *Efficient Teleportation Between Remote Single-Atom Quantum Memories*. Phys. Rev. Lett. **110**, 140403 (2013).

- [151] J. Volz, M. Weber, D. Schlenk, W. Rosenfeld, J. Vrana, K. Saucke, C. Kurtsiefer, H. Weinfurter. *Observation of Entanglement of a Single Photon with a Trapped Atom*. Phys. Rev. Lett. **96**, 030404 (2006).
- [152] D. L. Moehring, B. B. Blinov, D. W. Gidley, R. N. Kohn, Jr., M. J. Madsen, T. D. Sanderson, R. S. Vallery, C. Monroe. *Precision lifetime measurements of a single trapped ion with ultrafast laser pulses*. Phys. Rev. A **73**, 023413 (2006).
- [153] R. Loudon. *The Quantum Theory of Light*. Oxford University Press (1994).
- [154] J. D. Sterk, L. Luo, T. A. Manning, P. Maunz, C. Monroe. *Photon collection from a trapped ion-cavity system*. Phys. Rev. A **85**, 062308 (2012).
- [155] M. Schug, J. Huwer, C. Kurz, P. Müller, J. Eschner. *Heralded Photonic Interaction between Distant Single Ions*. Phys. Rev. Lett. **110**, 213603 (2013).
- [156] R. Gerritsma, G. Kirchmair, F. Zähringer, J. Benhelm, R. Blatt, C. F. Roos. *Precision measurement of the branching fractions of the  $4p^2P_{3/2}$  decay of Ca II*. Eur. Phys. J. D **50**, 13–19 (2008).
- [157] R. Hanbury Brown, R. Q. Twiss. *Correlation between Photons in two Coherent Beams of Light*. Nature **177**, 27–29 (1956).
- [158] P. Müller. *In preparation*. Ph.D. thesis, Universität des Saarlandes.
- [159] A. Stute, B. Casabone, B. Brandstätter, K. Friebe, T. E. Northup, R. Blatt. *Quantum-state transfer from an ion to a photon*. Nat. Photon. **7**, 219–222 (2013).
- [160] A. Reiserer, N. Kalb, G. Rempe, S. Ritter. *A quantum gate between a flying optical photon and a single trapped atom*. Nature **508**, 237–240 (2014).
- [161] E. Rephaeli, J.-T. Shen, S. Fan. *Full inversion of a two-level atom with a single-photon pulse in one-dimensional geometries*. Phys. Rev. A **82**, 033804 (2010).
- [162] G. Leuchs, M. Sondermann. *Time-reversal symmetry in optics*. Phys. Scr. **85**, 058101 (2012).
- [163] S. A. Aljunid, G. Maslennikov, Y. Wang, H. L. Dao, V. Scarani, C. Kurtsiefer. *Excitation of a Single Atom with Exponentially Rising Light Pulses*. Phys. Rev. Lett. **111**, 103001 (2013).
- [164] X.-L. Feng, Z.-M. Zhang, X.-D. Li, S.-Q. Gong, Z.-Z. Xu. *Entangling Distant Atoms by Interference of Polarized Photons*. Phys. Rev. Lett. **90**, 217902 (2003).
- [165] N. Piro, F. Rohde, C. Schuck, M. Almendros, J. Huwer, J. Ghosh, A. Haase, M. Hennrich, F. Dubin, J. Eschner. *Heralded single-photon absorption by a single atom*. Nat. Phys. **7**, 17–20 (2011).

- [166] J. Huwer, J. Ghosh, N. Piro, M. Schug, F. Dubin, J. Eschner. *Photon entanglement detection by a single atom*. New J. Phys. **15**, 025033 (2013).
- [167] A. G. Zajonc, L. J. Wang, X. Y. Zou, L. Mandel. *Quantum eraser*. Nature **353**, 507–508 (1991).
- [168] T. J. Herzog, P. G. Kwiat, H. Weinfurter, A. Zeilinger. *Complementarity and the Quantum Eraser*. Phys. Rev. Lett. **75**, 3034 (1995).
- [169] S. P. Walborn, M. O. Terra Cunha, S. Pádua, C. H. Monken. *Double-slit quantum eraser*. Phys. Rev. A **65**, 033818 (2002).
- [170] I. L. Chuang, M. A. Nielsen. *Prescription for experimental determination of the dynamics of a quantum black box*. J. Mod. Opt. **44**, 2455–2467 (1997).
- [171] B. Schumacher. *Sending entanglement through noisy quantum channels*. Phys. Rev. A **54**, 2614 (1996).
- [172] E. Mount, S.-Y. Baek, M. Blain, D. Stick, D. Gaultney, S. Crain, R. Noek, T. Kim, P. Maunz, J. Kim. *Single qubit manipulation in a microfabricated surface electrode ion trap*. New J. Phys. **15**, 093018 (2013).
- [173] B. B. Blinov, D. L. Moehring, L.-M. Duan, C. Monroe. *Observation of entanglement between a single trapped atom and a single photon*. Nature **428**, 153–157 (2004).
- [174] A. Stute, B. Casabone, P. Schindler, T. Monz, P. O. Schmidt, B. Brandstätter, T. E. Northup, R. Blatt. *Tunable ion-photon entanglement in an optical cavity*. Nature **485**, 482–485 (2012).
- [175] D. F. V. James, P. G. Kwiat, W. J. Munro, A. G. White. *Measurement of qubits*. Phys. Rev. A **64**, 052312 (2001).
- [176] M. Paris, J. Řeháček. *Quantum State Estimation*. Springer (2004).
- [177] M. Shalaby, A. Vourdas. *Tomographically complete sets of orthonormal bases in finite systems*. J. Phys. A **44**, 345303 (2011).
- [178] J. Aldrich. *R. A. Fisher and the making of maximum likelihood 1912-1922*. Statist. Sci. **12**, 162–176 (1997).
- [179] M. B. Plenio, S. Virmani. *An introduction to entanglement measures*. Quant. Inf. Comput. **7**, 1–51 (2007).
- [180] J. F. Clauser, M. A. Horne, A. Shimony, R. A. Holt. *Proposed Experiment to Test Local Hidden-Variable Theories*. Phys. Rev. Lett. **23**, 880 (1969).
- [181] N. Piro, A. Haase, M. W. Mitchell, J. Eschner. *An entangled photon source for resonant single-photon–single-atom interaction*. J. Phys. B **42**, 114002 (2009).

- [182] C. Schuck, F. Rohde, N. Piro, M. Almendros, J. Huwer, M. W. Mitchell, M. Hennrich, A. Haase, F. Dubin, J. Eschner. *Resonant interaction of a single atom with single photons from a down-conversion source*. Phys. Rev. A **81**, 011802(R) (2010).
- [183] J. Brito, S. Kucera, P. Eich, P. Müller, J. Eschner. *Doubly-heralded single-photon absorption by a single atom*. Preprint at <http://arxiv.org/abs/1508.01029> (2015).
- [184] L. Tian, P. Rabl, R. Blatt, P. Zoller. *Interfacing Quantum-Optical and Solid-State Qubits*. Phys. Rev. Lett. **92**, 247902 (2004).
- [185] M. Wallquist, K. Hammerer, P. Rabl, M. Lukin, P. Zoller. *Hybrid quantum devices and quantum engineering*. Phys. Scr. **2009**, 014001 (2009).
- [186] R. Ikuta, Y. Kusaka, T. Kitano, H. Kato, T. Yamamoto, M. Koashi, N. Imoto. *Wide-band quantum interface for visible-to-telecommunication wavelength conversion*. Nat. Commun. **2**, 537 (2011).
- [187] S. Zaske, A. Lenhard, C. A. Keßler, J. Kettler, C. Hepp, C. Arend, R. Albrecht, W.-M. Schulz, M. Jetter, P. Michler, C. Becher. *Visible-to-Telecom Quantum Frequency Conversion of Light from a Single Quantum Emitter*. Phys. Rev. Lett. **109**, 147404 (2012).
- [188] M. Born, V. Fock. *Beweis des Adiabatenatzes*. Zeitschrift für Physik **51**, 165–180 (1928).
- [189] C. Wunderlich, T. Hannemann, T. Körber, H. Häffner, C. Roos, W. Hänsel, R. Blatt, F. Schmidt-Kaler. *Robust state preparation of a single trapped ion by adiabatic passage*. J. Mod. Opt. **54**, 1541–1549 (2007).
- [190] T. Noel, M. R. Dietrich, N. Kurz, G. Shu, J. Wright, B. B. Blinov. *Adiabatic passage in the presence of noise*. Phys. Rev. A **85**, 023401 (2012).
- [191] S. Kotler, N. Akerman, Y. Glickman, A. Keselman, R. Ozeri. *Single-ion quantum lock-in amplifier*. Nature **473**, 61–65 (2011).
- [192] S. Kotler, N. Akerman, Y. Glickman, R. Ozeri. *Nonlinear Single-Spin Spectrum Analyzer*. Phys. Rev. Lett. **110**, 110503 (2013).
- [193] G. Jaeger. *Entanglement, Information, and the Interpretation of Quantum Mechanics*. Springer (2009).

# Danksagung

Um ein solch komplexes und aufwändiges Experiment wie unseres betreiben zu können bedarf es mehr als der Anstrengung eines einzelnen, sondern der Zusammenarbeit vieler. Daher möchte ich hier allen danken, die zum Gelingen dieser Arbeit beigetragen haben.

Mein erster Dank geht an Jürgen, einen Chef wie man ihn sich nur wünschen kann. Er versteht es, uns zum eigenständigen Denken und Handeln anzuregen und gibt uns damit sehr viel Freiraum in unserem Arbeitsalltag. Gleichzeitig steht er uns jederzeit mit seiner Weisheit zur Seite, hat für all unsere Anliegen stets ein offenes Ohr und nimmt sich Zeit für uns, selbst wenn er eigentlich gerade keine hat. Auch habe ich ihn als großzügigen Menschen und Chef kennengelernt, der seine Mitarbeiter an vielen (teilweise sehr teuren) Tagungen teilnehmen lässt, aber auch des öfteren den Kuchen für die wöchentlichen Gruppensitzung bezahlt. Letztere waren übrigens häufig das Highlight meiner Woche, insbesondere der Teil „Stammtisch“. Vielen Dank, Jürgen, für die schönen Jahre in deiner Gruppe.

Einen mindestens ebenso großen Anteil am Erfolg dieser Arbeit haben meine Kollegen, mit denen ich Labor und Büro teilen durfte. Michael, Jan und ich waren ein tolles Team, um den Umzug des Experiments von Spanien nach Saarbrücken zu bewerkstelligen und es danach auf ein Niveau zu bringen, mit dem wir all die in dieser Arbeit beschriebenen Messungen durchführen konnten. Ich danke Michael für seine Unermüdlichkeit und Hartnäckigkeit im Labor sowie seine nette Gesellschaft während wir beide an unseren Dissertationen schrieben. Jan zeichnete sich neben seiner Kompetenz im Labor vor allem durch seine Professionalität aus, mit der er essentielle Arbeiten, wie den Aufbau unseres Qubit-Lasers, bewerkstelligte. Michael und Jan, die Zeit mit euch möchte ich nicht missen. Auch will ich unsere Nachfolger, Pascal und Philipp, erwähnen, die derzeit das Labor am Laufen halten. Dank an Pascal für sein problemorientiertes Denken und die stets sehr unterhaltsame Fahrgemeinschaft. Philipp, einer der angenehmsten Menschen, die ich kenne, gebührt mein Dank für sein offenes Ohr für theoretische Fragen jeglicher Art sowie seine zahllosen Tipps im Umgang mit LaTeX.

Allen anderen Gruppenmitgliedern sei Dank für das tolle Arbeitsklima, das von Anfang an in unserer Gruppe herrschte. Erwähnt seien insbesondere José, der uns ein wenig südamerikanische Lebensart brachte, und Hannes, der den täglichen Mensagang mit interessanten Gesprächsthemen bereicherte. Alles Gute wünsche ich unseren beiden jüngsten Gruppenmitgliedern, Stephan und Matthias, beim weiteren Betrieb des Labors. Auch unsere Ehemaligen, Joyee und Johannes, die zur Vielfalt der Gruppe beitrugen, seien hier genannt.

Nicht zu vergessen ist natürlich unsere Sekretärin, Frau Michel, die all unsere Anliegen

## Danksagung

---

stets zügig und zuverlässig erledigt. Auch will ich die Arbeitsgruppen von Giovanna Morigi, Christoph Becher und Frank Wilhelm-Mauch erwähnen, die ein ausgezeichnetes wissenschaftliches Umfeld bilden. Dank außerdem an Prof. Schmidt-Kaler für die Begutachtung meiner Arbeit.

Nicht zuletzt geht mein Dank an Melanie für ihre Freundschaft und unsere sonntäglichen Abendessen, und an meine Eltern für ihre bedingungslose Unterstützung bei all meinen Vorhaben.